

The Photovoltaic Effect in Bismuth-Based Ferroelectric Perovskite Oxides

Dissertation

zur Erlangung des Doktorgrades
der Naturwissenschaften (Dr. rer. nat)

der

Naturwissenschaftlichen Fakultät II
Chemie, Physik und Mathematik

der

Martin-Luther-Universität Halle-Wittenberg

vorgelegt von

David Sebastian Walch (geb. Knoche)

Gutachtende: Prof. Dr. Jörg Schilling
Prof. Dr. Marin Alexe
Prof. Dr. Kathrin Dörr

Tag der Verteidigung: 8. November 2024

List of Publications

→ CHAPTER 4

Knoche, David S., Yun, Y., Ramakrishnegowda, N., Mühlenbein, L., Li, X. & Bhatnagar, A. “Domain and Switching Control of the Bulk Photovoltaic Effect in Epitaxial BiFeO₃ Thin Films”. *Scientific Reports* **9**, 13979 (2019)

Ramakrishnegowda, N., Yun, Y., **Knoche, David S.**, Mühlenbein, L., Li, X. & Bhatnagar, A. “Activity of Sub-Band Gap States in Ferroelectric Pb(Zr_{0.2}Ti_{0.8})O₃ Thin Films”. *Advanced Electronic Materials* **6**, 1900966 (2020)

Ramakrishnegowda, N., **Knoche, David S.**, Mühlenbein, L., Lotnyk, A. & Bhatnagar, A. “Bulk-Controlled Photovoltaic Effect in Nanometer-Thick Ferroelectric Pb(Zr_{0.2}Ti_{0.8})O₃ Thin Films and the Role of Domain Walls”. *ACS Applied Nano Materials* **3**, 11881–11888 (2020)

Mühlenbein, L., Singh, C. B., Lotnyk, A., Himcinschi, C., Yun, Y., Ramakrishnegowda, N., **Knoche, David S.**, Li, X. & Bhatnagar, A. “Nanocomposites with Three-Dimensional Architecture and Impact on Photovoltaic Effect”. *Nano Letters* **20**, 8789–8795 (2020)

→ CHAPTER 5

Knoche, David S., Steimecke, M., Yun, Y., Mühlenbein, L. & Bhatnagar, A. “Anomalous circular bulk photovoltaic effect in BiFeO₃ thin films with stripe-domain pattern”. *Nature Communications* **12**, 282 (2021)

Yun, Y., Mühlenbein, L., **Knoche, David S.**, Lotnyk, A. & Bhatnagar, A. “Strongly enhanced and tunable photovoltaic effect in ferroelectric-paraelectric superlattices”. *Science Advances* **7** (2021)

Himcinschi, C., Drechsler, F., **Walch, David S.**, Bhatnagar, A., Belik, A. A. & Kortus, J. “Unexpected Phonon Behaviour in BiFe_xCr_{1-x}O₃, a Material System Different from Its BiFeO₃ and BiCrO₃ Parents”. *Nanomaterials* **12** (2022)

→ CHAPTER 6

Walch, David S., Yun, Y., Ramakrishnegowda, N., Mühlenbein, L., Lotnyk, A., Himcinschi, C. & Bhatnagar, A. “Resistive Switching in Ferroelectric Bi₂FeCrO₆ Thin Films and Impact on the Photovoltaic Effect”. *Advanced Electronic Materials* **8**, 2200276 (2022)

Table of Content

List of Publications	I
Table of Content	II
List of Figures	IV
List of Tables	V
Acronyms/Abbreviations	VI
Nomenclature	VII
1 Introduction	1
2 Basics	5
2.1 Ferrioc Properties and Multiferroic Interactions	5
2.2 A-site Driven Ferroelectric Perovskite Oxides	8
2.3 Bulk Photovoltaic Effect	12
3 Thin Film Synthesis and Characterization Methods	23
3.1 Pulsed Laser Deposition	23
3.2 Substrate Selection & Treatment	25
3.3 Electrode Structuring and Deposition	26
3.4 Scanning Probe Microscopy	26
3.5 X-ray Diffraction Analysis	32
3.6 Photoelectrical Measurements	33

4	Domain and Switching Control of the Bulk Photovoltaic Effect in Epitaxial BiFeO₃ Thin Films	37
4.0	Abstract	38
4.1	Introduction	38
4.2	Results	39
4.3	Discussion	43
4.4	Methods	43
4.S	Supplementary Information	46
	Summary	49
5	Anomalous Circular Bulk Photovoltaic Effect in BiFeO₃ Thin Films with Stripe-Domain Pattern	51
5.0	Abstract	52
5.1	Introduction	53
5.2	Results	53
5.3	Discussion	57
5.4	Methods	57
5.S	Supplementary Information	60
	Summary	70
6	Resistive Switching in Ferroelectric Bi₂FeCrO₆ Thin Films and Impact on the Photovoltaic Effect	71
6.0	Abstract	72
6.1	Introduction	72
6.2	Results and Discussion	73
6.3	Conclusions	78
6.4	Experimental Section	78
6.S	Supplementary Information	81
	Summary	83
7	Summary & Conclusion	84
	Appendix	A

List of Figures

1.1	Number of publications containing "bulk photovoltaic effect" and similar terms and their total number of citations	2
2.1	Ferroic hysteresis and ferroic properties with possible multiferroic coupling effects	5
2.2	Classification of crystal classes, demonstrating the necessary pre-conditions for the existence of ferroelectricity.	6
2.3	Paraelectric-pyroelectric phase transition and ferroelectric switchability of a prototype ABO_3 structure	7
2.4	Rhombohedral crystal structure of ferroelectric $BiFeO_3$	9
2.5	Possible polarization variants of $BiFeO_3$ domains and three corresponding domain wall types	10
2.6	Schematic representation of the antiferromagnetic spin cycloid in $BiFeO_3$.	10
2.7	Transformation steps from general form of third rank tensor to linear and circular bulk photovoltaic (pseudo-)tensors	14
3.1	Picture and schematic of a pulsed laser deposition system and exemplary images of laser-induced plasma plumes	24
3.2	Epitaxial relationship between $BiFeO_3/Bi_2FeCrO_6$ and $SrTiO_3 (001)_c/DyScO_3 (110)_o$ substrates	25
3.3	Schematic depiction of used electrode configurations	26
3.4	Basic working principle of AFM microscopy in contact mode	27
3.5	Lennard-Jones potential and regimes of different AFM modes	28
3.6	Basic working principle of PFM	29
3.7	AFM, VPFM and LPFM images of $BiFeO_3$ thin film with striped domain configuration	30
3.8	Spectroscopy and manipulating possibilities of PFM	31
3.9	Basic principle of crystallographic XRD measurements	32
3.10	Experimental setup for BPV measurements and resulting light polarization	34
4.0	Publication I: Table of Content figure	37
4.1	Switchable BPV response in $BiFeO_3//SrTiO_3$ heterostructure with four polarization variants	39
4.2	Switching BPV response effect in $BiFeO_3//DyScO_3$ heterostructure with two polarization variants (electrodes \perp in-plane polarization)	41
4.3	Switching BPV response effect in $BiFeO_3//DyScO_3$ heterostructure with two polarization variants (electrodes \parallel in-plane polarization)	42
4.4	Intermediate switching states demonstrating the possibility to track the polarization rotation using the BPV response	42
4.S1	AFM topography and XRD $2\theta/\omega$ scans of $BiFeO_3/DyScO_3$ and $BiFeO_3/SrTiO_3$ samples	46
4.S2	Additional PFM measurements of the $BiFeO_3/ SrTiO_3$ thin film for extended domain structure characterization	46
4.S3	Initial measurements of the BPV effect of different $BiFeO_3$ thin films	47

4.S4	LPFM scans of intermediate switching states	47
4.S5	Comparison of BPV responses of the initial state and after repeated switching with same net in-plane polarization direction	48
4.S6	Summary of BPV response of several intermediate switching states	48
5.0	Publication II: Table of Content figure	51
5.1	Domain and structural characterization of BiFeO ₃ thin films	53
5.2	Photoelectrical measurements revealing LBPV and CBPV in BiFeO ₃ thin films	54
5.3	Deconvolution of the BPV response into linear and circular effects	55
5.4	Electrode alignments to show dominance of LCP over RCP response and vice versa	56
5.S1	AFM and PFM measurements of a BiFeO ₃ /DyScO ₃ thin film	60
5.S2	Schematic depiction of coordinate system transformation between pseudo-cubic, rhombohedral and hexagonal crystal system	62
5.S3	Demonstration of the switchable character of the photovoltaic effect	64
5.S4	Photovoltaic properties as a function of light intensity	65
5.S5	Extraction of photovoltaic properties from current-voltage characteristics	65
5.S6	Comparison between different orientations of outcoming light polarization	65
5.S7	Light polarization characterization	66
5.S8	Raman scattering experiments demonstrating the domain-specific light-matter interaction	67
5.S9	Linear and circular BPV effect in BiFeO ₃ /SrTiO ₃ thin film	68
6.0	Publication III: Table of Content figure	71
6.1	Structural characterization of Bi ₂ FeCrO ₆ thin films	73
6.2	Initial photovoltaic measurements	74
6.3	SPM demonstrating both ferroelectric and resistive switching locally	75
6.4	Comparing initial initial, high-resistive, and low-resistive states using SPM measurements	76
6.5	Resistive switching in macroscopic measurement	76
6.6	Multi-stage bi-directional resistive switching	77
6.7	Influence of resistive switching on photovoltaic properties / optical sensing of resistive state	77
6.S1	Electron microscopy images of Bi ₂ FeCrO ₆ /SrRuO ₃ /SrTiO ₃ heterostructure	81
6.S2	Fe and Cr composition profile acquired from EDX maps	81
6.S3	Current-voltage characteristics under solar simulator illumination	81
6.S4	Different vertical piezo-response force microscopy images demonstrating the retention of the switched domain configuration	82
6.S5	Capacitance-voltage characteristics	82

List of Tables

3.1	Typical PLD growth parameter	24
5.1	CBPV contribution from each ferroelectric domain variant	56

Acronyms/Abbreviations

AFM	atomic force microscopy	PEEM	photo emission electron microscopy
APV	abnormal/anomalous photovoltaic	PFM	piezo-response force microscopy
BFO	BiFeO ₃ bismuth ferrite	PG	photogalvanic
BFCO	Bi ₂ FeCrO ₆	PLD	pulsed laser deposition
BPV	bulk photovoltaic	PPL	parallel to net in-plane polarization
BTO	BaTiO ₃	PPP	perpendicular to net-inplane polarization
CBPV	circular bulk photovoltaic	PSD	position-sensitive detector
CCD	charge-coupled device	PV	photovoltaic
CD	circular dichroism/dichroic	PVD	physical vapor deposition
CP	circularly polarized	PZT	Pb[Zr _x Ti _{1-x}]O ₃
C-AFM	conductive atomic force microscopy	RCP	right-handed circularly polarized
DART	dual AC resonance tracking	RMS	root mean square
DSO	DyScO ₃	ROA	raman optical activity
EDX	energy dispersive X-ray	RSM	reciprocal space mapping/maps
HAADF	high-angle annular dark-field	SHG	second harmonic generation
HR	high-resistive	SMU	source measure unit
ITO	In ₂ O ₃ :Sn	SPM	scanning probe microscopy
LBPV	linear bulk photovoltaic	SRO	SrRuO ₃
LCP	left-handed circularly polarized	STM	scanning tunneling microscopy
LP	linearly polarized	STO	SrTiO ₃
LPFM	lateral piezo-response force microscopy	TEM	transmission electron microscopy
LR	low-resistive	UV	ultra-violet
LSMO	La _{0.7} Sr _{0.3} MnO ₃	VPFM	vertical piezo-response force microscopy
PCA	principle component analysis	XRD	X-ray diffraction
PE	photoelectrical		

Nomenclature

α_i	angles describing crystal structure	F_L	lateral force
β_{ij}^C	tensor circular BPV effect	F_N	normal force
β_{ij}^L	tensor linear BPV effect	f_{ac}	frequency of AC voltage
ϵ	(spontaneous) strain	H	magnetic field
ϵ	coefficient Lennard-Jones potential	I	current
ϵ	ellipticity ratio	I_{sc}	short-circuit current
λ	wavelength	i_{sc}	short-circuit current density
ω	rotation angle of oxygen octahedra	J	light intensity
σ	coefficient Lennard-Jones potential	l	inter-electrode distance
σ	mechanical stress	M	(spontaneous) magnetization
σ_d	dark conductivity	P_i	(spontaneous) polarization
σ_{ph}	photo conductivity	P_r	remanent polarization
\vec{e}	polarization unit vector of light wave	r	probe-sample distance
\vec{q}	wave vector	T	temperature
A	area	T_C	Curie temperature
a_i	lattice parameter	T_N	Néel temperature
d	interatomic distance	V	voltage
d_{ijk}	direct/converse piezoelectric tensor	V_{ac}	AC voltage function generator
E	electric field	V_{LN}	Lennard-Jones potential
E_c	coercive electric field	V_{oc}	open-circuit voltage
F_B	buckling force		

CHAPTER 1

Introduction

ABO_3 perovskite oxides represent a lucrative and diverse class of materials to discover new (multi-)functional materials. In first place, they are known for their ferroelectric representatives, for instance lead zirconate titanate $Pb[Zr_xTi_{1-x}]O_3$ (PZT) or barium titanate $BaTiO_3$ (BTO) being established in a variety of commercial applications.¹ In addition to ferroelectricity, the two complementary ferroic properties are ferromagnetism and ferroelasticity. Materials comprising at least two ferroic properties are known as multiferroics. Especially, multiferroic coupling in magnetoelectric materials are of immense interest in the material research community.^{2,3} The concept of switching the magnetization by the application of electric fields could lead to the development of future memory devices.⁴ However, the coexistence of ferroelectricity and ferromagnetism is rare in single-phase materials.^{5,6} One of the most prominent candidates is bismuth ferrite $BiFeO_3$ being referred to as "the holy grail of research on magnetoelectric multiferroics".⁴ $BiFeO_3$ is ferroelectric and antiferromagnetic at room temperature and has been successfully utilized to fabricate magnetoelectric coupling devices.⁷⁻⁹

On one hand, the absence of inversion symmetry in the crystal structure is necessary pre-condition for the existence of ferroelectricity. On the other hand, it is required for the occurrence of the so-called bulk photovoltaic (BPV) effect.¹⁰ The BPV effect is fundamentally different to the photovoltaic effect in semiconductors like silicon used in commercially available solar cells. Being discovered in the 1950s in $BaTiO_3$ ¹¹, the BPV effect has three unique features:

- I) The open-circuit voltages can exceed the corresponding band gap by several orders of magnitude.^{12,13}
- II) Magnitude and direction of the BPV effect depend on the polarization state of the incident light.¹⁴
- III) The photovoltaic properties, open-circuit voltage and short-circuit current, can be reversed by the application of electric fields.^{15,16}

As demonstrated in Figure 1.1, the research field of ferroelectric photovoltaics revitalized after the demonstration of the photovoltaic effect in $BiFeO_3$ thin films in 2009.^{17,18} After initial discussion about its origin,¹⁶ the BPV effect was demonstrated as underlying mechanism of the observed photovoltaic behavior in $BiFeO_3$.^{15,19,20} The BPV effect in addition to its multiferroic character makes $BiFeO_3$ interesting for a new generation of devices, that is photovoltaic neuromorphic systems.²¹

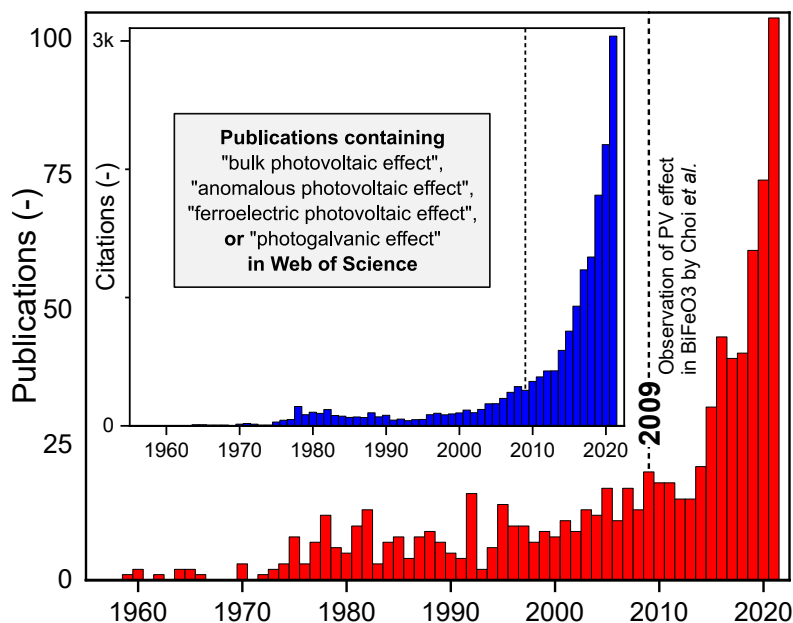


Figure 1.1: Number of publication containing the terms "bulk photovoltaic effect", "photogalvanic effect", "anomalous photovoltaic effect, or "ferroelectric photovoltaic effect" from 1955 to 2021. The inset shows their total number of citations. Certain data included herein are derived from Clarivate Web of Science. © Copyright Clarivate 2022. All rights reserved.

Even though the band gap of BiFeO_3 (2.7 eV²²) is low compared to other ferroelectric perovskite oxides, it is not optimal for photovoltaic energy-conversion applications.²³ The optimum band gap derived from thermodynamic consideration of a single-junction absorber ranges from 1.0 to 1.5 eV leading to a theoretically possible maximum energy conversion efficiency of $\sim 30\%$.^{24,25} There are different strategies to create a low-band gap ferroelectric. For example, the ferroelectric solid solution perovskite oxide based on potassium niobate $[\text{KNbO}_3]_{0.9}[\text{BaNi}_{1/2}\text{Nb}_{1/2}\text{O}_{3-\delta}]_{0.1}$ revealed a reduced band gap of 1.4 eV.²⁶ Another interesting material is $\text{Bi}_2\text{FeCrO}_6$ being closely related to BiFeO_3 . The chromium replacement of iron in BiFeO_3 was initially proposed to induce ferromagnetic ordering (instead of antiferromagnetic ordering). Interestingly, depending on the extent of the cationic ordering in the double perovskite $\text{Bi}_2\text{FeCrO}_6$ structure, the band gap varies from 1.4 to 2.5 eV.²⁷ The cationic ordering is controllable by the deposition conditions and therefore, a multi-layer device was fabricated and achieved an energy conversion efficiency of 8.1%, currently the maximum reported value of a photovoltaic device based on a ferroelectric perovskite oxide material.²⁷

The objective of this cumulative thesis was to conduct fundamental investigations of the BPV effect in bismuth-based ferroelectric perovskite oxides, BiFeO_3 and $\text{Bi}_2\text{FeCrO}_6$. The intrinsic link between the ferroelectric properties and BPV effect of BiFeO_3 was demonstrated using systematic photoelectrical measurements of different ferroelectric domain configurations under linearly polarized light. Furthermore, the circular BPV effect of BiFeO_3 was explored for the first time and an anomalous character of the BPV effect under circularly polarized light was observed. Finally, the ferroelectric and resistive switching behavior of $\text{Bi}_2\text{FeCrO}_6$ and their influence on the photovoltaic performance were investigated. The outcome of this work was published in various peer-reviewed articles (see Publication List above) and presented at several international conferences. Chapter 2 and 3 give short descriptions of the fundamen-

tal basics and experimental techniques, respectively. The main results of this thesis are represented by the corresponding articles (as published) in Chapter 4, 5 and 6. Supplementary Information can be found at the end of each chapter. Chapter 7 summarizes and concludes the main findings of this thesis.

Detailed descriptions of the co-authors' contribution can be found at the end each publication. The designs of the experiments were conceptualized in close collaboration with *Dr. Akash Bhatnagar*. X-ray diffraction measurements were performed by *Yeseul Yun*, *Niranjan Ramakrishnegowda*, *Xinye Li* and *Lutz Mühlenbein*. Raman scattering experiments and analysis were performed by *Dr. Matthias Steimecke*. Transmission electron microscopy specimen preparation and measurements were performed by *Dr. Andriy Lotnyk*. *Dr. Cameliu Himcinschi* performed ellipsometric measurements and analysis.

References - CHAPTER 1

1. Lines, M. E. & Glass, A. M. *Principles and applications of ferroelectrics and related materials* Reprinted. (Clarendon Press, Oxford, 2009).
2. Schmid, H. "Multi-ferroic magnetoelectrics". *Ferroelectrics* **162**, 317–338 (1994).
3. Spaldin, N. A. & Fiebig, M. "The renaissance of magnetoelectric multiferroics". *Science* **309**, 391–392 (2005).
4. Fiebig, M., Lottermoser, T., Meier, D. & Trassin, M. "The evolution of multiferroics". *Nature Reviews Materials* **1**, 16046 (2016).
5. Hill, N. A. "Why Are There so Few Magnetic Ferroelectrics?" *The Journal of Physical Chemistry B* **104**, 6694–6709 (2000).
6. Hill, N. A. & Filippetti, A. "Why are there any magnetic ferroelectrics?" *Journal of Magnetism and Magnetic Materials* **242-245**, 976–979 (2002).
7. Chu, Y.-H., Martin, L. W., Holcomb, M. B., Gajek, M., Han, S.-J., He, Q., Balke, N., Yang, C.-H., Lee, D., Hu, W., Zhan, Q., Yang, P.-L., Fraile-Rodríguez, A., Scholl, A., Wang, S. X. & Ramesh, R. "Electric-field control of local ferromagnetism using a magnetoelectric multiferroic". *Nature Materials* **7**, 478–482 (2008).
8. Heron, J. T., Trassin, M., Ashraf, K., Gajek, M., He, Q., Yang, S. Y., Nikonov, D. E., Chu, Y.-H., Salahuddin, S. & Ramesh, R. "Electric-field-induced magnetization reversal in a ferromagnet-multiferroic heterostructure". *Physical Review Letters* **107**, 217202 (2011).
9. Heron, J. T., Bosse, J. L., He, Q., Gao, Y., Trassin, M., Ye, L., Clarkson, J. D., Wang, C., Liu, J., Salahuddin, S., Ralph, D. C., Schlom, D. G., Iñiguez, J., Huey, B. D. & Ramesh, R. "Deterministic switching of ferromagnetism at room temperature using an electric field". *Nature* **516**, 370–373 (2014).
10. Sturman, B. I. & Fridkin, V. M. *The photovoltaic and photorefractive effects in noncentrosymmetric materials* (Gordon and Breach, Philadelphia, 1992).
11. Chynoweth, A. G. "Surface Space-Charge Layers in Barium Titanate". *Physical Review* **102**, 705–714 (1956).

12. Glass, A. M., von der Linde, D. & Negran, T. J. "High-voltage bulk photovoltaic effect and the photorefractive process in LiNbO_3 ". *Applied Physics Letters* **25**, 233–235 (1974).
13. Brody, P. S. "High voltage photovoltaic effect in barium titanate and lead titanate-lead zirconate ceramics". *Journal of Solid State Chemistry* **12**, 193–200 (1975).
14. Koch, W., Munser, R., Ruppel, W. & Würfel, P. "Bulk photovoltaic effect in BaTiO_3 ". *Solid State Communications* **17**, 847–850 (1975).
15. Ji, W., Yao, K. & Liang, Y. C. "Bulk photovoltaic effect at visible wavelength in epitaxial ferroelectric BiFeO_3 thin films". *Advanced Materials* **22**, 1763–1766 (2010).
16. Yang, S. Y., Seidel, J., Byrnes, S. J., Shafer, P., Yang, C.-H., Rossell, M. D., Yu, P., Chu, Y.-H., Scott, J. F., Ager, J. W., Martin, L. W. & Ramesh, R. "Above-bandgap voltages from ferroelectric photovoltaic devices". *Nature Nanotechnology* **5**, 143–147 (2010).
17. Choi, T., Lee, S., Choi, Y. J., Kiryukhin, V. & Cheong, S.-W. "Switchable ferroelectric diode and photovoltaic effect in BiFeO_3 ". *Science* **324**, 63–66 (2009).
18. Yang, S. Y., Martin, L. W., Byrnes, S. J., Conry, T. E., Basu, S. R., Paran, D., Reichertz, L., Ihlefeld, J., Adamo, C., Melville, A., Chu, Y.-H., Yang, C.-H., Musfeldt, J. L., Schlom, D. G., Ager, J. W. & Ramesh, R. "Photovoltaic effects in BiFeO_3 ". *Applied Physics Letters* **95**, 062909 (2009).
19. Yi, H. T., Choi, T., Choi, S. G., Oh, Y. S. & Cheong, S.-W. "Mechanism of the switchable photovoltaic effect in ferroelectric BiFeO_3 ". *Advanced Materials* **23**, 3403–3407 (2011).
20. Bhatnagar, A., Roy Chaudhuri, A., Heon Kim, Y., Hesse, D. & Alexe, M. "Role of domain walls in the abnormal photovoltaic effect in BiFeO_3 ". *Nature Communications* **4**, 2835 (2013).
21. Pérez-Tomás, A. "Functional Oxides for Photoneuromorphic Engineering: Toward a Solar Brain". *Advanced Materials Interfaces* **6**, 1900471 (2019).
22. Sando, D., Carrétéro, C., Grisolia, M. N., Barthélémy, A., Nagarajan, V. & Bibes, M. "Revisiting the Optical Band Gap in Epitaxial BiFeO_3 Thin Films". *Advanced Optical Materials* **6**, 1700836 (2018).
23. Tablero, C. "An evaluation of BiFeO_3 as a photovoltaic material". *Solar Energy Materials and Solar Cells* **171**, 161–165 (2017).
24. Shockley, W. & Queisser, H. J. "Detailed Balance Limit of Efficiency of p-n Junction Solar Cells". *Journal of Applied Physics* **32**, 510–519 (1961).
25. Würfel, P. *Physik der Solarzellen 2*. [vollst. überarb.] Aufl. (Spektrum Akad. Verl., Heidelberg, 2000).
26. Grinberg, I., West, D. V., Torres, M., Gou, G., Stein, D. M., Wu, L., Chen, G., Gallo, E. M., Akbashev, A. R., Davies, P. K., Spanier, J. E. & Rappe, A. M. "Perovskite oxides for visible-light-absorbing ferroelectric and photovoltaic materials". *Nature* **503**, 509–512 (2013).
27. Nechache, R., Harnagea, C., Li, S., Cardenas, L., Huang, W., Chakrabartty, J. & Rosei, F. "Bandgap tuning of multiferroic oxide solar cells". *Nature Photonics* **9**, 61–67 (2015).

CHAPTER 2

Basics

2.1 Ferroc Properties and Multiferroic Interactions

Ferroelectricity, ferromagnetism and ferroelasticity are the three primary ferroic properties. Ferroelectrics, ferromagnets, and ferroelastics exhibit a spontaneous polarization, spontaneous magnetization and spontaneous (mechanical) strain, respectively, with at least two orientation states. It is possible to switch between these states by the application of an external stimulus (electric field, magnetic field, mechanical stress) following a hysteretic behavior (Figure 2.1a). Materials, exhibiting at least two ferroic orders in one phase, are called multiferroics.¹ The co-existence of these is a fundamental requirements for the observation of multiferroic elastoelectric, magnetoelectric, and magnetoelastic coupling effects (Figure 2.1b).

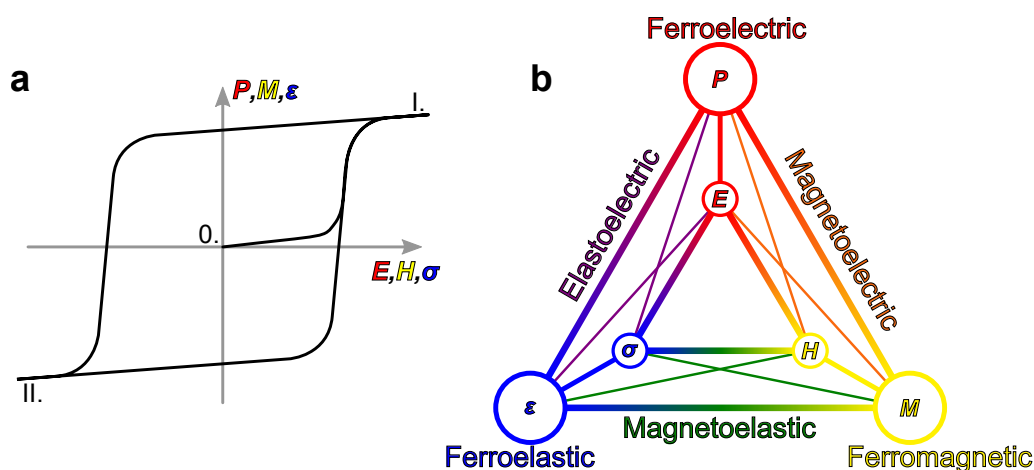


Figure 2.1: a Hysteretic behavior of the ferroic properties spontaneous polarization P , magnetization M and strain ϵ as a function of the external stimulus electric field E , magnetic field H and mechanical stress σ , respectively. The application of the external stimulus enables the setting of two different orientation states (I. & II.). b Ferroc properties and multiferroic coupling including magnetoelastic, elastoelectric, and magnetoelectric effects (adapted from Spaldin *et al.*²).

For future applications, multiferroic materials combining ferroelectric and ferromagnetic properties are interesting for novel devices.² The possibility of tuning the magnetization by the application of electric fields is capable of renew data storage concepts³, however, multiferroic magnetoelectric character is a rare combination in

single-phase materials at room temperature. Prominent candidates are bismuth-based ferroelectric perovskite oxides (more details and comparison to prototype perovskite oxides in Section 2.2).^{4,5}

2.1.1 Ferroelectricity

Despite the co-existence of magnetic ordering in BiFeO_3 and $\text{Bi}_2\text{FeCrO}_6$, ferroelectricity is the primary ferroic property of interest in this thesis and will be further discussed below. The schematic in Figure 2.2 demonstrates the necessary pre-conditions for the existence of ferroelectricity in a crystal. Out of 32 crystal classes, only 10 are fulfilling those conditions.^{6,7} The structure has to be non-centrosymmetric, piezoelectric, and pyroelectric with a switchable polarization.

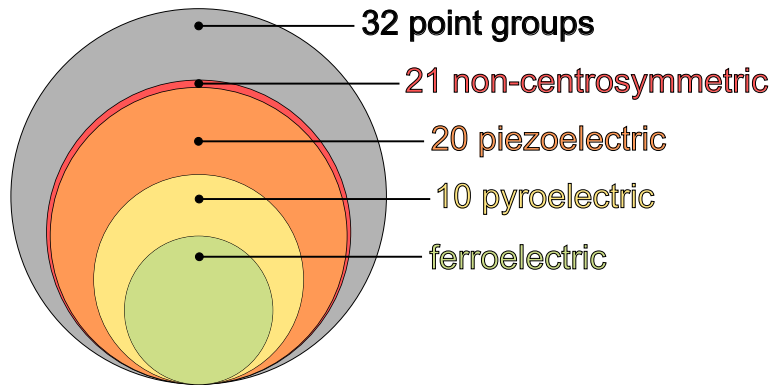


Figure 2.2: Classification of crystal classes, demonstrating the necessary pre-conditions for the existence of ferroelectricity.

Piezoelectricity is a tensorial property describing the coupling between mechanical stress σ / mechanical strain ε and electric polarization P_i / electric field E_i :^{6,7}

Direct piezoelectric effect:

$$P_i = d_{ijk}\sigma_{jk} \quad (2.1)$$

Converse piezoelectric effect:

$$\varepsilon_{jk} = d_{ijk}E_i \quad (2.2)$$

The third rank piezoelectric tensor d_{ijk} can be derived from the symmetry of the crystal. Note, that the tensorial notation is often replaced by a reduced matrix notation due to a reduction of independent coefficients because of symmetry reasons. The converse piezoelectric effect is utilized to investigate ferroelectric crystals using piezo-response force microscopy (PFM). Details on the technique can be found in Section 3.4.1.

Pyroelectric crystals undergo a phase transition from a paraelectric high-symmetry high-temperature to a polar low-symmetry low-temperature phase crossing a specific temperature called Curie temperature. This transition induces a change of polarization ΔP_i for a temperature change ΔT :^{6,7}

$$\Delta P_i = p_i \Delta T \quad (2.3)$$

The first rank polar tensor p_i consists out of three coefficients. Pyroelectricity is theoretically possible in 10 out of 32 crystal classes referred to as *polar* classes (1, 2, 3, 4, 6, m , $mm2$, $3m$, $4mm$, $6mm$).^{6,7}

The schematic of an ABO_3 perovskite oxide structure in Figure 2.2a-b demonstrates the transition from a cubic centrosymmetric to a tetragonal non-centrosymmetric with an off-centered B-cation in direction of the polar axis. As mentioned in Section 2.1, a ferroic property has two different states of orientation that are switchable by an external stimulus. Transferring this to the prototype ferroelectric ABO_3 structure in Figure 2.3b-c, the position of the B-cation can be reversibly switched by an external electric field resulting of an opposed electric polarization (black arrows).

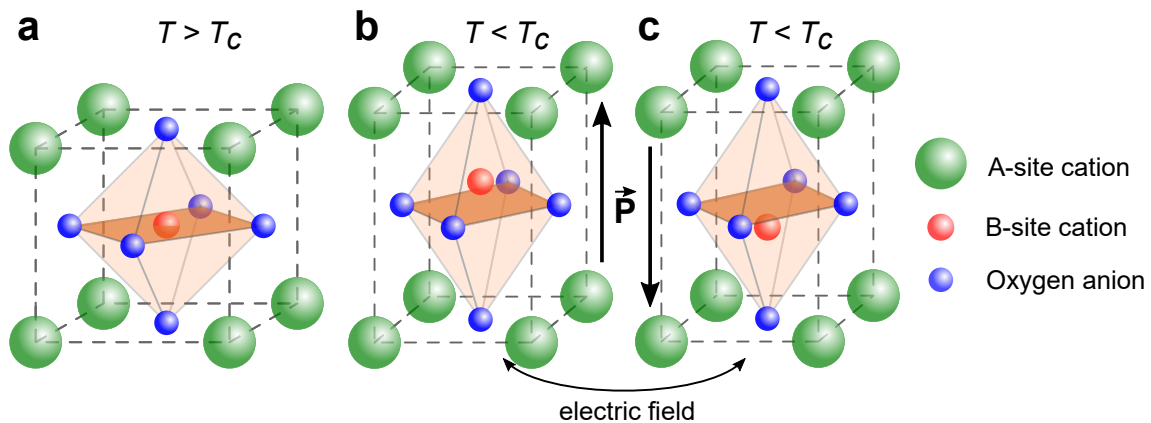


Figure 2.3: **a** Cubic paraelectric ABO_3 structure above the Curie temperature T_c . **b** Tetragonal pyroelectric ABO_3 structure below T_c with off-centered B-site cation inducing polarization along [001]-direction. Hysteretic electric-field reversal of polarization (from **b** to **c**) is needed to establish ferroelectricity.

The switching from one orientation state to the other follows a hysteretic behavior (compare Figure 2.1a) and the threshold electric field needed to change the polarization is called coercive electric field E_c . The remaining polarization in absence of an electric field is referred to as remanent polarization $\pm P_r$. A domain is an area of same polarization (direction) with a separating boundary called domain wall. Further details on the domain configurations and its visualization using PFM are explained in Section 3.4.1.

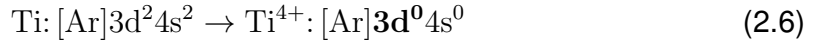
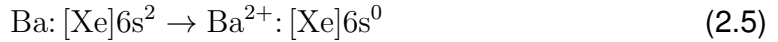
Ferroelectrics are commonly used in capacitors because of their high dielectric permittivity, in actuators and sensors because of their strong piezoelectric coupling, and in ferroelectric memory devices because of their hysteretic polarization behavior.⁸ Especially ferroelectric perovskite oxides are of great interest in the material science research because of their simple atomic structure, sensitivity to strain (with respect to thin films), and the innumerable different compositions with a wide range of different functional properties.⁸

2.2 A-site Driven Ferroelectric Perovskite Oxides

Perovskite oxides consist out of an A-site cation, a B-site transition metal cation, surrounded by a cage of oxygen anions (compare Figure 2.3). A mismatch between the radii of A-site and B-site cation favors crystal structures different than the ideal cubic perovskite structure. Calculating the Goldschmidt tolerance factor t_{ABO} ⁹ can give a first idea of the present structure of a perovskite oxide:

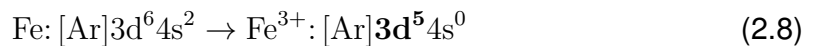
$$t_{\text{ABO}} = \frac{r_{\text{A}} + r_{\text{O}^{2-}}}{\sqrt{2}(r_{\text{B}} + r_{\text{O}^{2-}})} \quad t_{\text{BTO}} \approx 1.06 \quad t_{\text{BFO}} \approx 0.88, \quad (2.4)$$

whereas r_i are the radii of the different ions (ionic radius values taken from Shannon¹⁰). Perovskite oxides with values $t > 1$ tend to exhibit a tetragonal ferroelectric structure. This scenario of a "prototype" ferroelectric material is valid in BaTiO₃ ($t_{\text{BTO}} \approx 1.06$) with a tetragonal crystal structure at room temperature^{11,12}. Furthermore, the d-shell of B-site transition metal ion is empty (see formal electron configuration in (2.6)).^{4,13} Ferroelectricity arises from off-centering of the transition metal ion with respect to the oxygen cage. The hybridization between empty d-orbital and oxygen 2p-orbital stabilizes the ferroelectric distortion.^{4,14} Most ferroelectric perovskite oxides contain a B-site cation with empty d-shell (Ti⁴⁺, Zr⁴⁺, Nb⁵⁺) and this fact is sometimes referred to as d⁰-ness of ferroelectrics. This condition prohibits the existence of a magnetic ordering in most ferroelectric perovskite oxides.⁴



Contrary, the scenario is different in bismuth-based ferroelectrics like BiFeO₃. The Goldschmidt tolerance factor ($t_{\text{BFO}} \approx 0.88$) is smaller than one and the small Bi³⁺ ion on the A-site introduces a local distortion which favors rhombohedral structures.¹⁵ In this case, ferroelectricity is not driven by the off-centering of the B-cation, but there is a strong hybridization of the A-site bismuth cation's 6p- and the oxygen 2p-orbitals.⁴ The ferroelectricity is driven by the bismuth 6s²-orbital. The room temperature crystal structure of BiFeO₃ and the origin of ferroelectricity will be discussed in detail below in Section 2.2.1.

The iron cation at the B-site has a partially filled d-orbital (see formal electron configuration in (2.8)). The existence of a partially filled d-orbital of the transition metal ion at the B-site is a precondition of magnetic ordering. Details on the magnetic ordering in BiFeO₃ and Bi₂FeCrO₆ will be explained below.



2.2.1 Bismuth Ferrite BiFeO_3

The crystal structure of BiFeO_3 below the Curie temperature $T_c = 1083 \text{ K}$ ($810 \text{ }^\circ\text{C}$)¹⁶ is rhombohedral (space group $R3c$, point group $3m$).^{17–19} The rhombohedral (rh) structure ($a_{rh} = 5.64343 \text{ \AA}$, $\alpha_{rh} = 59.348^\circ$)¹⁹ can be described with the help of two cubic perovskite oxide unit cells (pseudo-cubic (pc) notation) with a slight rhombohedral distortion ($a_{pc} = 3.965 \text{ \AA}$, $\alpha_{pc} = 89.45^\circ$) as shown in Figure 2.4a.¹⁹ Note: The tensorial calculations of physical properties, e.g. BPV effect, requires the transformation from the rhombohedral to the cartesian coordinate system based on a hexagonal structure (IEEE standard setting). More information about the transformation can be found in Section 5.S.

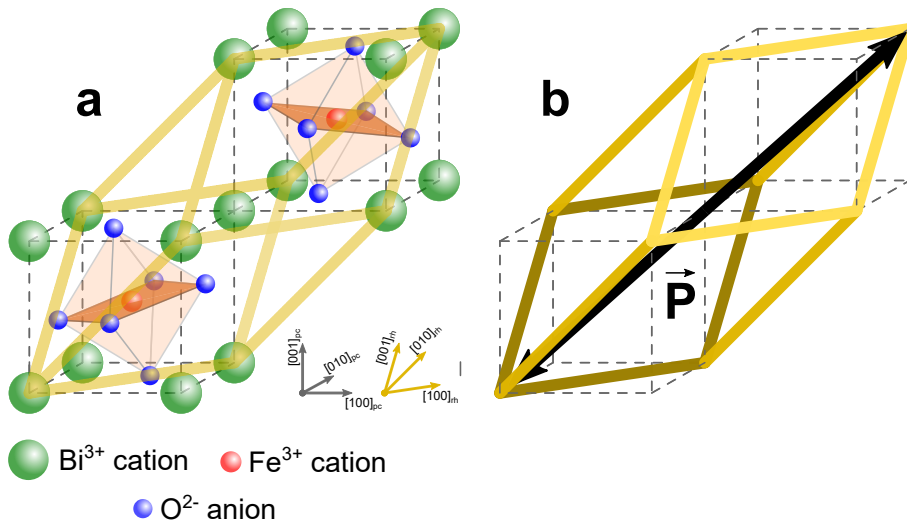


Figure 2.4: **a** Connection between two cubic perovskite oxide unit cells (gray dotted lines, pseudo-cubic (pc)) and the rhombohedral (rh) unit cell of BiFeO_3 (solid yellow lines). The opposed rotation of the two oxygen octahedra is visualized slightly. **b** Demonstration of the polarization direction with respect to the pseudo-cubic and rhombohedral unit cell.

Due to the ionic configuration, there is an opposed rotation of neighboring oxygen octahedra about and an ionic displacement of Bi^{3+} and Fe^{3+} ions along the $[111]_{pc}$ direction (Black arrow in Figure 2.4b).^{19,20} The rotation angle of the oxygen octahedra is $\omega = \pm 13.8^\circ$.¹⁹ The resulting polarization arises from a relative shift of the Bi^{3+} and Fe^{3+} within its O^{2-} surrounding along the $[111]_{pc}$ direction, whereas the Bi^{3+} displacement (0.540 \AA) is four times larger than the Fe^{3+} displacement (0.135 \AA).¹⁹ The large Bi^{3+} displacement is originated from the stereochemically active $6s^2$ lone pair. Ferroelectricity driven by an A-site lone pair has been also demonstrated to occur in BiMnO_3 ²¹ and PbTiO_3 .⁴ The theoretically predicted magnitude of polarization in BiFeO_3 ranges from $90 \mu\text{C cm}^{-2}$ to $100 \mu\text{C cm}^{-2}$,²⁰ which agrees with experimental investigations of single crystals²² and thin films²³.

Depending on the variant, the polarization vector can point along any of the four diagonal of the perovskite unit cell. The polarization of each structural (or ferroelastic) variant P_i has two antiparallel direction options, two ferroelectric variants. In total, there are eight different polarization variants P_i^\pm in BiFeO_3 as shown in Figure 2.5a. The separating domain walls are described using the angle between the corresponding polarization vector. Boundaries separating two antiparallel variants of the same

structural variant (P_2^+ / P_1^-) are called ferroelectric 180° domain walls (Figure 2.5b). Ferroelastic 109° and 71° domain walls (Figure 2.5c,d) occur at the interface between polarization variants of different structural variants.

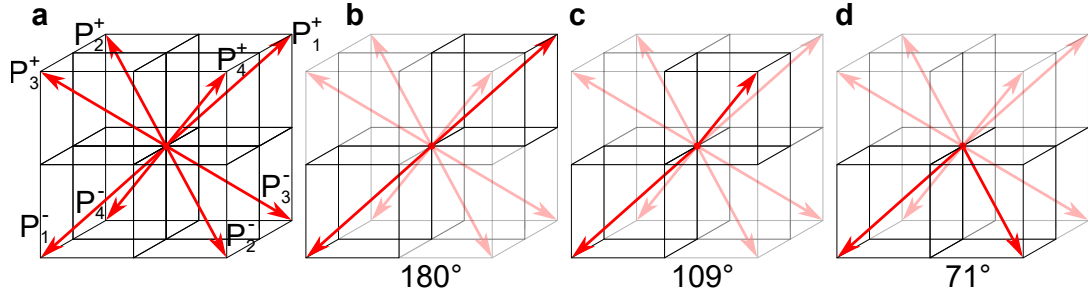


Figure 2.5: **a** Eight possible polarization variants resulting from two ferroelectric variants from each of the four structural (or ferroelastic) variants. **b-d** Polarization vector configuration of neighboring domains resulting in 180° , 109° and 71° domain walls, respectively.

Initial neutron powder diffraction investigations of single crystals in the 1960/70s identified BiFeO_3 as G-type anti-ferromagnet.^{18,24,25} Different experimental techniques revealed the Néel temperature T_N in the range from 643 to 655 K (370 to 382 °C).^{15,26} Subsequent high-resolution time-of-flight neutron diffraction experiment revealed the existence of an antiferromagnetic cycloidal arrangement of spins (spin spiral) with a period length of $\lambda \sim 60$ nm.²⁷ The weak effective magnetic moment arises from a small spin canting induced by the interaction between the non-collinear antiferromagnetic texture and the ferroelectric polarization via the Dzyalshinskii-Moriya interaction.^{28–30} A schematic representation of the antiferromagnetic spin cycloid can be found in Figure 2.6. In recent studies, the antiferromagnetic spin texture in BiFeO_3 thin films was visualized via scanning nitrogen-vacancy magnetometry.³¹ The propagation direction of the cycloid changes from one ferroelectric domain to the other³² and the influence of the epitaxial strain on the cycloidal arrangement can be used to tailor the antiferromagnetic character of the thin films.^{33–35}

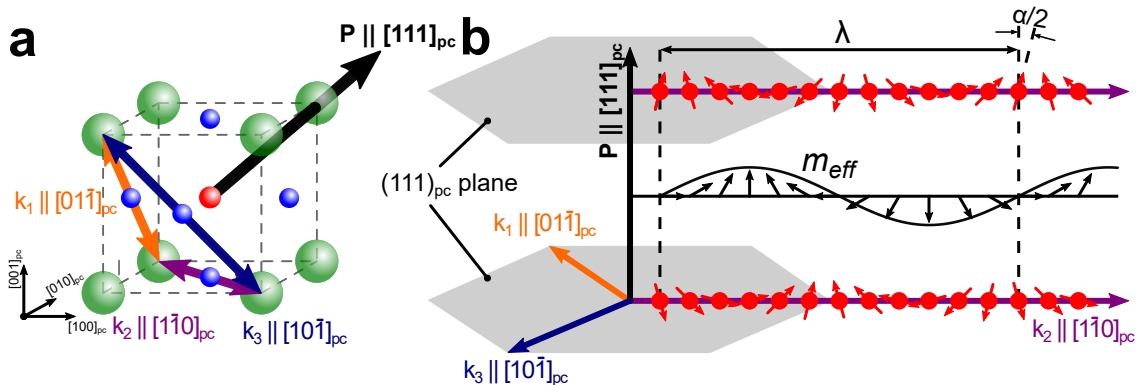


Figure 2.6: **a** Pseudo-cubic unit cell of BiFeO_3 with the three possible cycloid propagation directions ($k_1 \parallel [01\bar{1}]_{pc}$, $k_2 \parallel [1\bar{1}0]_{pc}$, $k_3 \parallel [10\bar{1}]_{pc}$). The ferroelectric polarization is pointing in $[111]_{pc}$ direction and all three cycloid propagation direction lie within the $(111)_{pc}$ plane. **b** Schematic representation of the cycloid arrangement of Fe^{3+} spins in two neighboring $(111)_{pc}$ planes with periodic length λ (top and bottom). The canting of the antiferromagnetic spin alignment (described by α) gives rise to an effective magnetic moment m_{eff} (middle). (Adapted from Gross *et al.*³¹)

The fabrication of epitaxial BiFeO₃ thin films with high polarization magnitude and small magnetization in the early 2000s triggered developing of electromagnetic coupling devices.²³ Using high-quality BiFeO₃ single crystals, electromagnetic coupling was demonstrated.³⁶ The application of an electric field forced a reorientation of the ferroelectric polarization and thus a changed orientation of the canted spin cycloid.³⁶ The destruction of the cycloidal antiferromagnetic spin arrangement in thin films due to the epitaxial strain has been proposed³⁷ and experimentally demonstrated on SrTiO₃ (111)_c substrates³⁸ However, subsequent experiments demonstrated the spin cycloid existence in thin film fabricated under moderate epitaxial strain.³³ The electromagnetic coupling in BiFeO₃ thin film based advanced heterostructures was also demonstrated.^{39–41} The application of electric fields to the BiFeO₃ layer changed the polarization direction and reversed the weak antiferromagnetic magnetization. Antiferromagnetic-ferromagnetic coupling induced a switching in a ferromagnetic top layer (Co_{0.9}Fe_{0.1}).^{39–41}

2.2.2 Bismuth Iron Chromium Oxide Bi₂FeCrO₆

Simultaneous to the demonstration of the electromagnetic coupling in BiFeO₃ described above, there is an ongoing search for alternative room temperature multiferroics. Other Bi-based ferroelectrics with similarities to BiFeO₃ are promising candidates and the first description of Bi₂FeCrO₆ using first principle density functional theory calculation predicted the existence of both large polarization and large magnetization at room temperature.^{42,43} The ordered double perovskite consists out of alternating Cr and Fe planes in [111]_{pc} direction (compare Figure 2.4). As in BiFeO₃, ferroelectricity is induced by Bi⁺³-cation at the A-site.^{4,42} With regard to BiFeO₃, the alternating substitution of Fe-ion with Cr-ions reduces the crystal symmetry from space group R3c to R3 ($a_{rh} = 5.47 \text{ \AA}$, $\alpha_{rh} = 60.09^\circ$).^{42,43} Spontaneous magnetization is introduced via ferrimagnetism.⁴² The Fe and Cr planes were expected to show ferromagnetic properties with an antiferromagnetic coupling between them and the different magnitude of magnetization results in an overall net magnetization.⁴²

Soon after the theoretical prediction, successful synthesis of Bi₂FeCrO₆ thin films enabled experiments to confirm the expected multiferroic behavior at room temperature by Nechache *et al.*^{44–48} The thin films were fabricated using pulsed laser deposition with a single stoichiometric Bi₂FeCrO₆ target, dual cross beam pulsed laser deposition⁴⁹ and superlattice growth⁵⁰ with separate BiFeO₃ and BiCrO₃ targets. Thin films were grown mostly on both single-crystalline (001)_c and (111)_{pc} SrTiO₃ substrates. The existence of cationic ordered Fe/Cr layering along [111]_{pc} direction was demonstrated using X-ray diffraction measurements^{46,47} and is essential for the multiferroic character of the material⁴³. Thin films with decreased ionic ordering are expected to show a massively decreased (if any) net magnetization.⁵¹

2.3 Bulk Photovoltaic Effect

The photovoltaic (PV) effect is the conversion of photon energy into electric energy, i.e. the generation of electric voltage and current under illumination. Semi-conducting materials absorb the photon energy of the incident illumination and convert it into chemical energy of an excited electron-hole pair. The separation of the excited charge carriers results in a steady-state current and/or voltage.

Conventional photovoltaic devices (solar cells) are based on semi-conducting material (often silicon) with differently doped regions. Because of the formation of a depletion layer between these regions, the effect is also referred to as barrier or junction photovoltaic effect.^{52,53} Another different photovoltaic effect is the bulk photovoltaic (BPV) effect also known as photogalvanic (PG) effect or abnormal/anomalous photovoltaic (APV) effect. The name refers to the general occurrence of the effect within the bulk of a material without any inhomogeneity, e.g. within a pure crystal.⁵² In contrast to the barrier photovoltaic effect, the current flow direction is predefined by the internal symmetry of the crystal and the effect occurs in a uniform medium under homogeneous illumination.⁵⁴ Due to symmetry reasons, the BPV effect in ferroelectrics and pyroelectrics is closely connected to the polarization direction. Thus, both polarization and BPV current flow can be tuned by the application of electric fields in ferroelectrics. Despite this switchability, there are two more outstanding features, which make the effect clearly distinguishable from the barrier photovoltaic effect:

- I) The observed open-circuit voltages are not limited by the corresponding band gap of the material.^{55,56}
- II) The BPV properties depend on the polarization of the incident light.⁵⁷

2.3.1 Microscopic Origin

After the first observation of an abnormal photovoltaic in BaTiO₃ in the late 1950s,⁵⁸ the research interest of the ferroelectric photovoltaic effect emerged. In the 1960s and 70s, the BaTiO₃ studies^{56,57,59} were accompanied by investigations of PbZr_xTi_{1-x}O₃⁵⁶ and transition metal doped LiNbO₃ (usually Fe-doped)^{55,60–62}. Several theoretical investigations have been carried out trying to explain the microscopic origin of the effect.^{52,63} Contrary to the barrier-layer photovoltaic effect in semiconductors with pn-junction^{64,65}, the transport of excited charge carriers exists without a gradient of electrochemical potential.⁶⁶ Illumination of ferroelectrics induces a local heating and therefore pyroelectric effects, however, corresponding transient currents resulting from the excitation-provoked polarization change cannot explain the observed steady-state photo current under constant illumination.⁶⁷ A first model proposed by Glass *et al.* in the mid 1970s suggests an asymmetric charge transfer at homogeneously distributed impurities (for example Fe dopants in LiNbO₃).⁶⁷

Soon after the introduction of the Glass model, the quadratic response theory was used to describe BPV currents in pure ferroelectric crystals without considering any impurity or trap level assistance phenomenologically.^{66,68–70} The current density is linked to the electric field of the radiation by the introduction of an additional quadratic term.^{66,68–70} This is analogous to the description of the induced polarization under illumination describing non-linear optical effects with the quadratic response theory.^{66,68–70}

Further theoretical studies confirm that the BPV effect is inherent in media lacking inversion symmetry and can be explained by the general asymmetry of elementary electronic processes.^{68,71–73} The asymmetry of excitation, recombination and scattering processes leads to the absence of detailed balancing under non-equilibrium conditions⁷³ and is valid for several different transitions (band-band, impurity-band, etc.).⁷⁴ Consequently, the steady-state current under illumination arises from an asymmetric electron distribution function of non-equilibrium charge carriers.^{73,75} For the generation of photo electro-motoric forces, either the existence of asymmetries in real space or an asymmetric momentum distribution of excited charge carriers is needed.⁵³ This is the main difference between the barrier effect in conventional photovoltaic devices and the bulk photovoltaic effect in non-centrosymmetric materials. The pn-junction exhibits a gradient of electrochemical potential as an asymmetry in real space.⁷³ Whereas the BPV effect originates from the asymmetry of the elementary electronic processes in momentum space.⁷³ Currents arising from the asymmetric momentum distribution are also referred to as ballistic currents j_b and contribute to both linear and circular BPV effect.⁷⁶

The theoretical understanding of the BPV effect was extended at the beginning of the 1980s.^{77,78} The overall current arising from the BPV effect, however, is a sum of j_b and the so-called shift (or displacement) current j_s .^{76–78} j_s results from a spatial shift (in real space) during the electron excitation^{76,79}. The shift contribution to the BPV current depends on the non-diagonal elements (with respect to the band number) of the density matrix.^{76–78,80}

The discovery of the photovoltaic effect in BiFeO₃ (compare Section 2.3.3) re-initiated theoretical investigations of the shift current contribution to the overall BPV response.^{81,82} Due to the simultaneous existence of j_b and j_s with comparable magnitude, the experimental separation of these two contributions is challenging.⁷⁸ Despite the complex realization, first experimental efforts trying to distinguish the overall BPV response in piezoelectric Bi₁₂GeO₂₀ into its corresponding ballistic and shift current contributions have been published recently.⁸⁰

2.3.2 Phenomenological Description

The phenomenological expression of a current \vec{j} in a uniform medium with applied electric field \vec{E} and under illumination of a monochromatic light wave (wave vector \vec{q} , polarization unit vector \vec{e} , light intensity J) is shown in Equation (2.9).^{54,83} The expression is incomplete and describes the corresponding currents with independent tensor components without giving information about the magnitude of the coefficients:⁵⁴

$$j_i = \underbrace{\sigma_{ij}^d E_j}_{\text{Dark conduction (Ohm's law)}} + \underbrace{\sigma_{ijl} E_j E_l}_{\text{Photo conduction}} + \underbrace{\sigma_{ijlm}^{ph} E_j e_l e_m^* J}_{\text{Photon-drag effect}} + \underbrace{\chi_{ijlm} q_j e_l e_m^* J}_{\text{Photon-drag effect}} + \underbrace{\beta_{ijl} e_j e_l^* J}_{\text{Bulk photovoltaic effect}} + \dots \quad (2.9)$$

The BPV effect is a physical property described by the third-rank BPV tensor β_{ijl} .⁷³ The transformation path from the general third rank tensor to the linear bulk photovoltaic (LBPV) and circular bulk photovoltaic (CBPV) tensors are shown in Figure 2.7. First, the symmetry operations of the corresponding crystal structure is applied to the general form of a third-rank tensor β_{ijl}^G . The resulting symmetry-specific tensor β_{ijl} can be split into its symmetric β_{ijl}^S and antisymmetric β_{ijl}^A part.⁸⁴ β_{ijl}^S describes

the BPV effect under linearly-polarized light illumination. Due to the symmetry of linearly polarized light, a reduced matrix notation can be used (tensor notation: $3^3 = 27$ independent coefficients, $\beta_{ijl}^S \rightarrow$ matrix notation: $3 \times 6 = 18$ independent coefficients, β_{il}^L).^{6,7} The shape of the linear BPV tensor β_{il}^L is analogous to the piezoelectric tensor d_{ij} and therefore β_{il}^L is non-zero for all piezoelectrics. β_{ijl}^A describes the BPV effect under circularly-polarized light and can be transformed into a second-rank tensor β_{il}^C using the Levi-Civita symbol. β_{il}^C is non-zero for all gyrotropic materials. Its appearance is analogous to the gyrotropic axial (pseudo-)tensor g_{lk} , which is connected to the natural optical activity tensor γ_{ijl}^A using the Levi-Civita symbol ϵ_{ijk} .^{85,86}

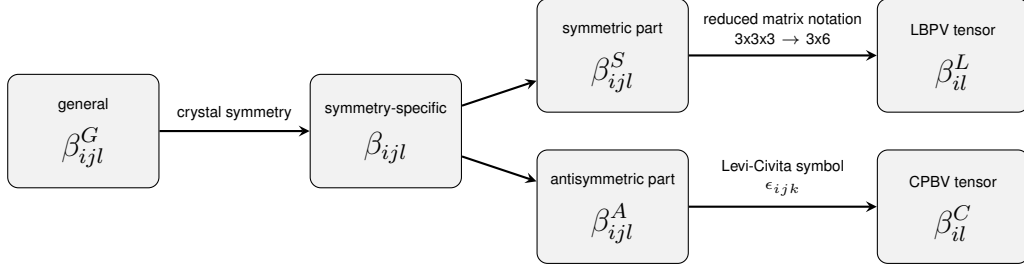


Figure 2.7: Transformation steps from general form of third rank tensor to linear and circular BPV (pseudo-)tensors, respectively.

Consequently, the overall BPV current j_i can be subdivided into the currents j_i^L and j_i^C arising from the linear and circular BPV effect, respectively. j_i^L depends on the direction of the incident linear light polarization. j_i^C scales up with the light's circularity.

$$j_i = \beta_{ijl} e_j e_l^* J = j_i^L + j_i^C = \underbrace{\beta_{il}^L [e^{\rightarrow} e^{\rightarrow*}]_l J}_{\text{Linear BPV effect}} + \overbrace{\beta_{il}^C [e^{\rightarrow} e^{\rightarrow*}]_l J}_{\text{Circular BPV effect}} \quad (2.10)$$

As described above, the open-circuit voltages $V_{i,oc}$ corresponding to j_i are not limited by the band gap of the absorbing material:

$$V_{i,oc} = \frac{j_i l}{\sigma_{ph} + \sigma_d}. \quad (2.11)$$

Following the linear relation between current and voltage, i.e. Ohm's law, $V_{i,oc}$ depends on the overall conductivity $\sigma_{ph} + \sigma_d$, the short-circuit current density j_i and scales up linearly with the inter-electrode distance l . Hence in open-circuit condition, an electric field builds up caused by the accumulation of charge carriers at the electrodes due to the photovoltaic current generation. Because of the tensorial nature of the (bulk) photovoltaic current (compare Equation (2.10)), the resulting open-circuit voltage also depends on the polarization state of the incident light.

2.3.3 Photovoltaic Effect in BiFeO₃ & Bi₂FeCrO₆

The research of ferroelectric photovoltaic materials revitalized after the observation of a switchable diodic current-voltage characteristic and an associated photovoltaic effect in BiFeO₃ in 2009.^{87,88} The photovoltaic effect was found to be dependent on the orientation of the incoming linearly polarized light. However, these measurements using a capacitor electrode geometry revealed resulting open-circuit voltages below the corresponding band gap. These findings triggered a discussion about the mechanism of the effect and subsequent reports suggest the BPV effect as a possible origin.^{89,90} Photoelectrical measurements under white light illumination using two top electrodes on BiFeO₃ thin films epitaxially grown on single-crystalline DyScO₃ substrates showed open-circuit voltages larger than 15 V tunable by the application of electric fields.⁹¹ The photovoltaic effect was only observed with electrodes oriented parallel to the ferroelectric stripe domains. Therefore, the existence of above-band gap photovoltages was attributed to a new mechanism based on the charge-carrier separation at each domain wall.^{91,92} Open-circuit voltages above band gap were also observed in single-crystalline BiFeO₃ with a sharp tip serving as an efficient collecting top electrode.⁹³ More detailed temperature-resolved photoelectrical measurements on BiFeO₃//DyScO₃ thin films under linearly-polarized laser light illumination identified the BPV effect to be the origin of the photovoltaic effect in BiFeO₃.⁹⁴ This was further confirmed by tensorial calculations matching the observed orientation dependent photovoltaic measurements^{94,95} and the observation of a photovoltaic effect in monodomain BiFeO₃ thin films⁹⁶. Even though its band gap $E_g = 2.7$ eV⁹⁷ is low compared to other perovskite oxides, it is too high to develop efficient photovoltaic devices for energy conversion purposes.⁹⁸ The optimum band gap of a single-junction absorber ranges from 1.0 to 1.5 eV.^{99,100}

The higher the band gap of the absorber, the smaller the usable fraction of the solar spectrum. Therefore, different engineering strategies to reduce the band gap in ferroelectric perovskite oxides were employed. For example, a band gap of 1.4 eV was measured in the ferroelectric solid solution perovskite oxide $[\text{KNbO}_3]_{0.9}[\text{BaNi}_{1/2}\text{Nb}_{1/2}\text{O}_{3-\delta}]_{0.1}$ (band gap KNbO₃ of 3.8 eV).¹⁰¹ Regarding BiFeO₃ as parent material, the substitution of B-site cation is one possible way to tune the light-absorbing properties without destroying the ferroelectric character (see details about the origin of ferroelectricity in BiFeO₃ in Section 2.2.1). After the successful fabrication of Bi₂FeCrO₆ thin films and the demonstration of its multiferroic character⁴⁴, a switchable photovoltaic effect depending on the ferroelectric polarization direction was demonstrated in 2011.¹⁰² In 2015, the possibility of tuning the band gap of Bi₂FeCrO₆ thin films by changing the ionic ordering of the B-site cation was reported.¹⁰³ Depending on the process parameter during thin film growth, the extent of cationic ordering differs and the band gap values range from 1.4 to 2.5 eV.¹⁰³ This knowledge enabled the realization of a multi-layer Bi₂FeCrO₆ thin film with efficient light-absorbing properties leading to a solar conversion efficiency of over 8% under 1.5AM illumination.¹⁰³

References - CHAPTER 2

1. Schmid, H. "Multi-ferroic magnetoelectrics". *Ferroelectrics* **162**, 317–338 (1994).
2. Spaldin, N. A. & Fiebig, M. "The renaissance of magnetoelectric multiferroics". *Science* **309**, 391–392 (2005).
3. Fiebig, M., Lottermoser, T., Meier, D. & Trassin, M. "The evolution of multiferroics". *Nature Reviews Materials* **1**, 16046 (2016).
4. Hill, N. A. "Why Are There so Few Magnetic Ferroelectrics?" *The Journal of Physical Chemistry B* **104**, 6694–6709 (2000).
5. Hill, N. A. & Filippetti, A. "Why are there any magnetic ferroelectrics?" *Journal of Magnetism and Magnetic Materials* **242-245**, 976–979 (2002).
6. Newnham, R. E. *Properties of materials: Anisotropy, symmetry, structure* (Oxford Univ. Press, Oxford, 2004).
7. Nye, J. F. *Physical properties of crystals: Their representation by tensors and matrices* Reprinted. (Clarendon Press, Oxford, 2012).
8. Lines, M. E. & Glass, A. M. *Principles and applications of ferroelectrics and related materials* Reprinted. (Clarendon Press, Oxford, 2009).
9. Goldschmidt, V. M. "Die Gesetze der Krystallochemie". *Naturwissenschaften* **14**, 477–485 (1926).
10. Shannon, R. D. "Revised effective ionic radii and systematic studies of interatomic distances in halides and chalcogenides". *Acta Crystallographica Section A* **32**, 751–767 (1976).
11. Forsbergh, P. W. "Domain Structures and Phase Transitions in Barium Titanate". *Physical Review* **76**, 1187–1201 (1949).
12. Evans, H. T. "An X-ray diffraction study of tetragonal barium titanate". *Acta Crystallographica* **14**, 1019–1026 (1961).
13. Cheong, S.-W. & Mostovoy, M. "Multiferroics: a magnetic twist for ferroelectricity". *Nature Materials* **6**, 13–20 (2007).
14. Shen, Y., Cai, J., Ding, H.-.-C., Shen, X.-.-W., Fang, Y.-.-W., Tong, W.-.-Y., Wan, X.-.-G., Zhao, Q. & Duan, C.-.-G. "Role of Lone-Pairs in Driving Ferroelectricity of Perovskite Oxides: An Orbital Selective External Potential Study". *Advanced Theory and Simulations*, 1900029 (2019).
15. Catalan, G. & Scott, J. F. "Physics and Applications of Bismuth Ferrite". *Advanced Materials* **21**, 2463–2485 (2009).
16. Tabares-Muñoz, C., Rivera, J.-P. & Schmid, H. "Ferroelectric domains, birefringence and absorption of single crystals of BiFeO₃". *Ferroelectrics* **55**, 235–238 (1984).
17. Michel, C., Moreau, J.-M., Achenbach, G. D., Gerson, R. & James, W. J. "The atomic structure of BiFeO₃". *Solid State Communications* **7**, 701–704 (1969).
18. Moreau, J. M., Michel, C., Gerson, R. & James, W. J. "Ferroelectric BiFeO₃ X-ray and neutron diffraction study". *Journal of Physics and Chemistry of Solids* **32**, 1315–1320 (1971).

19. Kubel, F. & Schmid, H. "Structure of a ferroelectric and ferroelastic monodomain crystal of the perovskite BiFeO_3 ". *Acta Crystallographica Section B, Structural Science*, 698–702 (1990).
20. Neaton, J. B., Ederer, C., Waghmare, U. V., Spaldin, N. A. & Rabe, K. M. "First-principles study of spontaneous polarization in multiferroic BiFeO_3 ". *Physical Review B* **71**, 014113 (2005).
21. Seshadri, R. & Hill, N. A. "Visualizing the Role of Bi 6s "Lone Pairs" in the Off-Center Distortion in Ferromagnetic BiMnO_3 ". *Chemistry of Materials* **13**, 2892–2899 (2001).
22. Lebeugle, D., Colson, D., Forget, A., Viret, M., Bonville, P., Marucco, J. F. & Fusil, S. "Room-temperature coexistence of large electric polarization and magnetic order in BiFeO_3 single crystals". *Physical Review B* **76** (2007).
23. Wang, J., Neaton, J. B., Zheng, H., Nagarajan, V., Ogale, S. B., Liu, B., Viehland, D., Vaithyanathan, V., Schlom, D. G., Waghmare, U. V., Spaldin, N. A., Rabe, K. M., Wuttig, M. & Ramesh, R. "Epitaxial BiFeO_3 multiferroic thin film heterostructures". *Science* **299**, 1719–1722 (2003).
24. Kiselev, S. V., Ozerov, R. P. & Zhdanov, G. S. "Detection of Magnetic Order in Ferroelectric BiFeO_3 by Neutron Diffraction". *Soviet Physics Doklady* **7**, 742 (1963).
25. Jacobson, A. J. & Fender, B. E. F. "A neutron diffraction study of the nuclear and magnetic structure of BiFeO_3 ". *Journal of Physics C: Solid State Physics* **8**, 844–850 (1975).
26. Blaauw, C. & van der Woude, F. "Magnetic and structural properties of BiFeO_3 ". *Journal of Physics C: Solid State Physics* **6**, 1422–1431 (1973).
27. Sosnowska, I., Neumaier, T. P. & Steichele, E. "Spiral magnetic ordering in bismuth ferrite". *Journal of Physics C: Solid State Physics* **15**, 4835–4846 (1982).
28. Kadomtseva, A. M., Zvezdin, A. K., Popov, Y. F., Pyatakov, A. P. & Vorob'ev, G. P. "Space-time parity violation and magnetoelectric interactions in antiferromagnets". *Journal of Experimental and Theoretical Physics* **79**, 571–581 (2004).
29. Fennie, C. J. "Ferroelectrically induced weak ferromagnetism by design". *Physical Review Letters* **100**, 167203 (2008).
30. Ederer, C. & Fennie, C. J. "Electric-field switchable magnetization via the Dzyaloshinskii-Moriya interaction: FeTiO_3 versus BiFeO_3 ". *Journal of Physics: Condensed Matter* **20**, 434219 (2008).
31. Gross, I., Akhtar, W., Garcia, V., Martínez, L. J., Chouaieb, S., Garcia, K., Carrière, C., Barthélémy, A., Appel, P., Maletinsky, P., Kim, J.-V., Chauleau, J. Y., Jaouen, N., Viret, M., Bibes, M., Fusil, S. & Jacques, V. "Real-space imaging of non-collinear antiferromagnetic order with a single-spin magnetometer". *Nature* **549**, 252–256 (2017).
32. Chauleau, J.-Y., Chirac, T., Fusil, S., Garcia, V., Akhtar, W., Tranchida, J., Thibaudeau, P., Gross, I., Blouzon, C., Finco, A., Bibes, M., Dkhil, B., Khalyavin, D. D., Manuel, P., Jacques, V., Jaouen, N. & Viret, M. "Electric and antiferromagnetic chiral textures at multiferroic domain walls". *Nature Materials* **19**, 386–390 (2020).

33. Sando, D., Agbelele, A., Rahmedov, D., Liu, J., Rovillain, P., Toulouse, C., Infante, I. C., Pyatakov, A. P., Fusil, S., Jacquet, E., Carrétéro, C., Deranlot, C., Lisenkov, S., Wang, D., Le Breton, J.-M., Cazayous, M., Sacuto, A., Juraszek, J., Zvezdin, A. K., Bellaiche, L., Dkhil, B., Barthélémy, A. & Bibes, M. "Crafting the magnonic and spintronic response of BiFeO₃ films by epitaxial strain". *Nature Materials* **12**, 641–646 (2013).
34. Agbelele, A., Sando, D., Toulouse, C., Paillard, C., Johnson, R. D., Ruffer, R., Popkov, A. F., Carrétéro, C., Rovillain, P., Le Breton, J.-M., Dkhil, B., Cazayous, M., Gallais, Y., Méasson, M.-A., Sacuto, A., Manuel, P., Zvezdin, A. K., Barthélémy, A., Juraszek, J. & Bibes, M. "Strain and Magnetic Field Induced Spin-Structure Transitions in Multiferroic BiFeO₃". *Advanced Materials* **29** (2017).
35. Haykal, A., Fischer, J., Akhtar, W., Chauleau, J.-Y., Sando, D., Finco, A., Godel, F., Birkhölzer, Y. A., Carrétéro, C., Jaouen, N., Bibes, M., Viret, M., Fusil, S., Jacques, V. & Garcia, V. "Antiferromagnetic textures in BiFeO₃ controlled by strain and electric field". *Nature Communications* **11**, 1704 (2020).
36. Lebeugle, D., Colson, D., Forget, A., Viret, M., Bataille, A. M. & Gukasov, A. "Electric-field-induced spin flop in BiFeO₃ single crystals at room temperature". *Physical Review Letters* **100**, 227602 (2008).
37. Bai, F., Wang, J., Wuttig, M., Li, J., Wang, N., Pyatakov, A. P., Zvezdin, A. K., Cross, L. E. & Viehland, D. "Destruction of spin cycloid in (111)_c-oriented BiFeO₃ thin films by epitaxial constraint: Enhanced polarization and release of latent magnetization". *Applied Physics Letters* **86**, 032511 (2005).
38. Béa, H., Bibes, M., Petit, S., Kreisel, J. & Barthélémy, A. "Structural distortion and magnetism of BiFeO₃ epitaxial thin films: A Raman spectroscopy and neutron diffraction study". *Philosophical Magazine Letters* **87**, 165–174 (2007).
39. Chu, Y.-H., Martin, L. W., Holcomb, M. B., Gajek, M., Han, S.-J., He, Q., Balke, N., Yang, C.-H., Lee, D., Hu, W., Zhan, Q., Yang, P.-L., Fraile-Rodríguez, A., Scholl, A., Wang, S. X. & Ramesh, R. "Electric-field control of local ferromagnetism using a magnetoelectric multiferroic". *Nature Materials* **7**, 478–482 (2008).
40. Heron, J. T., Trassin, M., Ashraf, K., Gajek, M., He, Q., Yang, S. Y., Nikonov, D. E., Chu, Y.-H., Salahuddin, S. & Ramesh, R. "Electric-field-induced magnetization reversal in a ferromagnet-multiferroic heterostructure". *Physical Review Letters* **107**, 217202 (2011).
41. Heron, J. T., Bosse, J. L., He, Q., Gao, Y., Trassin, M., Ye, L., Clarkson, J. D., Wang, C., Liu, J., Salahuddin, S., Ralph, D. C., Schlom, D. G., Iñiguez, J., Huey, B. D. & Ramesh, R. "Deterministic switching of ferromagnetism at room temperature using an electric field". *Nature* **516**, 370–373 (2014).
42. Baettig, P. & Spaldin, N. A. "Ab initio prediction of a multiferroic with large polarization and magnetization". *Applied Physics Letters* **86**, 012505 (2005).
43. Baettig, P., Ederer, C. & Spaldin, N. A. "First principles study of the multiferroics BiFeO₃, Bi₂FeCrO₆, and BiCrO₃: Structure, polarization, and magnetic ordering temperature". *Physical Review B* **72** (2005).

44. Nechache, R., Harnagea, C., Pignolet, A., Normandin, F., Veres, T., Carignan, L.-P. & Ménard, D. "Growth, structure, and properties of epitaxial thin films of first-principles predicted multiferroic $\text{Bi}_2\text{FeCrO}_6$ ". *Applied Physics Letters* **89**, 102902 (2006).
45. Nechache, R., Harnagea, C., Carignan, L.-P., Ménard, D. & Pignolet, A. "Epitaxial $\text{Bi}_2\text{FeCrO}_6$ multiferroic thin films". *Philosophical Magazine Letters* **87**, 231–240 (2007).
46. Nechache, R., Carignan, L.-P., Gunawan, L., Harnagea, C., Botton, G. A., Ménard, D. & Pignolet, A. "Epitaxial thin films of multiferroic $\text{Bi}_2\text{FeCrO}_6$ with B-site cationic order". *Journal of Materials Research* **22**, 2102–2110 (2007).
47. Nechache, R., Harnagea, C., Carignan, L.-P., Ménard, D. & Pignolet, A. "Structure and properties of epitaxial thin films of $\text{Bi}_2\text{FeCrO}_6$: A multiferroic material postulated by ab-initio computation". *Integrated Ferroelectrics* **101**, 152–163 (2008).
48. Nechache, R., Harnagea, C., Carignan, L.-P., Gautreau, O., Pintilie, L., Singh, M. P., Ménard, D., Fournier, P., Alexe, M. & Pignolet, A. "Epitaxial thin films of the multiferroic double perovskite $\text{Bi}_2\text{FeCrO}_6$ grown on (100)-oriented SrTiO_3 substrates: Growth, characterization, and optimization". *Journal of Applied Physics* **105**, 061621 (2009).
49. Nechache, R., Harnagea, C., Gunawan, L., Carignan, L.-P., Maunders, C., Ménard, D., Botton, G. A. & Pignolet, A. "Growth, structure, and properties of BiFeO_3 - BiCrO_3 films obtained by dual cross beam PLD". *IEEE Transactions on Ultrasonics, Ferroelectrics, and Frequency Control* **54**, 2645–2652 (2007).
50. Ichikawa, N., Arai, M., Imai, Y., Hagiwara, K., Sakama, H., Azuma, M., Shimakawa, Y., Takano, M., Kotaka, Y., Yonetani, M., Fujisawa, H., Shimizu, M., Ishikawa, K. & Cho, Y. "Multiferroism at Room Temperature in $\text{BiFeO}_3/\text{BiCrO}_3$ (111) Artificial Superlattices". *Applied Physics Express* **1**, 101302 (2008).
51. Nechache, R., Harnagea, C. & Pignolet, A. "Multiferroic properties-structure relationships in epitaxial $\text{Bi}_2\text{FeCrO}_6$ thin films: recent developments". *Journal of Physics: Condensed Matter* **24**, 096001 (2012).
52. Tauc, J. "Generation of an emf in Semiconductors with Nonequilibrium Current Carrier Concentrations". *Reviews of Modern Physics* **29**, 308–324 (1957).
53. Ruppel, W., von Baltz, R. & Wurfel, P. "The origin of the photo-emf in ferroelectric and non-ferroelectric materials". *Ferroelectrics* **43**, 109–123 (1982).
54. Sturman, B. I. & Fridkin, V. M. *The photovoltaic and photorefractive effects in noncentrosymmetric materials* (Gordon and Breach, Philadelphia, 1992).
55. Glass, A. M., von der Linde, D. & Negran, T. J. "High-voltage bulk photovoltaic effect and the photorefractive process in LiNbO_3 ". *Applied Physics Letters* **25**, 233–235 (1974).
56. Brody, P. S. "High voltage photovoltaic effect in barium titanate and lead titanate-lead zirconate ceramics". *Journal of Solid State Chemistry* **12**, 193–200 (1975).
57. Koch, W., Munser, R., Ruppel, W. & Würfel, P. "Bulk photovoltaic effect in BaTiO_3 ". *Solid State Communications* **17**, 847–850 (1975).

58. Chynoweth, A. G. "Surface Space-Charge Layers in Barium Titanate". *Physical Review* **102**, 705–714 (1956).
59. Koch, W. T. H., Munser, R., Ruppel, W. & Würfel, P. "Anomalous photovoltage in BaTiO₃". *Ferroelectrics* **13**, 305–307 (1976).
60. Chen, F. S. "Optically Induced Change of Refractive Indices in LiNbO₃ and LiTaO₃". *Journal of Applied Physics* **40**, 3389–3396 (1969).
61. Krätzig, E. & Kurz, H. "Photorefractive and Photovoltaic Effects in Doped LiNbO₃". *Optica Acta: International Journal of Optics* **24**, 475–482 (1977).
62. Jösch, W., Munser, R., Ruppel, W. & Würfel, P. "The photovoltaic effect and the charge transport in LiNbO₃". *Ferroelectrics* **21**, 623–625 (1978).
63. Brody, P. S. & Crowne, F. "Mechanism for the high voltage photovoltaic effect in ceramic ferroelectrics". *Journal of Electronic Materials* **4**, 955–971 (1975).
64. Lehovec, K. "The Photo-Voltaic Effect". *Physical Review* **74**, 463–471 (1948).
65. Chapin, D. M., Fuller, C. S. & Pearson, G. L. "A New Silicon p–n Junction Photocell for Converting Solar Radiation into Electrical Power". *Journal of Applied Physics* **25**, 676–677 (1954).
66. Kraut, W. & von Baltz, R. "Anomalous bulk photovoltaic effect in ferroelectrics: A quadratic response theory". *Physical Review B* **19**, 1548–1554 (1979).
67. Glass, A. M., von der Linde, D., Auston, D. H. & Negran, T. J. "Excited state polarization, bulk photovoltaic effect and the photorefractive effect in electrically polarized media". *Journal of Electronic Materials* **4**, 915–943 (1975).
68. Baskin, E. M., Blokh, M. D., Entin, M. V. & Magarill, L. I. "Current quadratic in field and photogalvanic effect in crystals without inversion centre". *physica status solidi (b)* **83**, K97–K100 (1977).
69. Von Baltz, R. & Kraut, W. "Bulk photovoltaic effect in pure pyro- and piezoelectrics". *Physics Letters A* **79**, 364–366 (1980).
70. Von Baltz, R. & Kraut, W. "Theory of the bulk photovoltaic effect in pure crystals". *Physical Review B* **23**, 5590–5596 (1981).
71. Belinicher, V. I., Malinovsky, V. K. & Sturman, B. I. "Photogalvanic effect in a crystal with polar axis". *Journal of Experimental and Theoretical Physics* **1977**, 692–699 (1977).
72. Von Baltz, R. "Theory of the Anomalous Bulk Photovoltaic Effect in Ferroelectrics". *physica status solidi (b)* **89**, 419–429 (1978).
73. Belinicher, V. I. & Sturman, B. I. "The photogalvanic effect in media lacking a center of symmetry". *Soviet Physics Uspekhi* **23**, 199–223 (1980).
74. Kristoffel, N. & Gulbis, A. "Some optical properties of a vibronic ferroelectric and the anomalous bulk photovoltaic effect". *Zeitschrift für Physik B - Condensed Matter* **39**, 143–149 (1980).
75. Von Baltz, R. "The bulk photovoltaic effect in ferro- and piezoelectric materials". *Ferroelectrics* **35**, 131–136 (1981).
76. Sturman, B. I. "Ballistic and shift currents in the bulk photovoltaic effect theory". *Physics-Uspekhi* **63**, 407–411 (2020).

77. Belinicher, V. I., Ivchenko, E. L. & Sturman, B. I. "Kinetic theory of the displacement photovoltaic effect in piezoelectric". *Journal of Experimental and Theoretical Physics* **1982**, 649–661 (1982).
78. Belinicher, V. I. & Sturman, B. I. "The relation between shift and ballistic currents in the theory of photogalvanic effect". *Ferroelectrics* **83**, 29–34 (1988).
79. Fridkin, V. M. "Review of recent work on the bulk photovoltaic effect in ferro and piezoelectrics". *Ferroelectrics* **53**, 169–187 (1984).
80. Burger, A. M., Agarwal, R., Aprelev, A., Schrubba, E., Gutierrez-Perez, A., Fridkin, V. M. & Spanier, J. E. "Direct observation of shift and ballistic photovoltaic currents". *Science Advances* **5**, eaau5588 (2019).
81. Young, S. M. & Rappe, A. M. "First principles calculation of the shift current photovoltaic effect in ferroelectrics". *Physical Review Letters* **109**, 116601 (2012).
82. Young, S. M., Zheng, F. & Rappe, A. M. "First-principles calculation of the bulk photovoltaic effect in bismuth ferrite". *Physical Review Letters* **109**, 236601 (2012).
83. Fridkin, V. M. "Bulk photovoltaic effect in noncentrosymmetric crystals". *Crystallography Reports* **46**, 654–658 (2001).
84. Wilson, D. W., Glytsis, E. N., Hartman, N. F. & Gaylord, T. K. "Beam diameter threshold for polarization conversion photoinduced by spatially oscillating bulk photovoltaic currents in $\text{LiNbO}_3\text{:Fe}$ ". *Journal of the Optical Society of America B* **9**, 1714 (1992).
85. Gallego, S. V., Etxebarria, J., Elcoro, L., Tasci, E. S. & Perez-Mato, J. M. "Automatic calculation of symmetry-adapted tensors in magnetic and non-magnetic materials: a new tool of the Bilbao Crystallographic Server". *Acta Crystallographica Section A* **75**, 438–447 (2019).
86. Landau, L. D. & Lifshits, E. M. *Electrodynamics of continuous media* 2nd ed., rev (Pergamon, Oxford, 1984).
87. Choi, T., Lee, S., Choi, Y. J., Kiryukhin, V. & Cheong, S.-W. "Switchable ferroelectric diode and photovoltaic effect in BiFeO_3 ". *Science* **324**, 63–66 (2009).
88. Yang, S. Y., Martin, L. W., Byrnes, S. J., Conry, T. E., Basu, S. R., Paran, D., Reichertz, L., Ihlefeld, J., Adamo, C., Melville, A., Chu, Y.-H., Yang, C.-H., Musfeldt, J. L., Schlom, D. G., Ager, J. W. & Ramesh, R. "Photovoltaic effects in BiFeO_3 ". *Applied Physics Letters* **95**, 062909 (2009).
89. Ji, W., Yao, K. & Liang, Y. C. "Bulk photovoltaic effect at visible wavelength in epitaxial ferroelectric BiFeO_3 thin films". *Advanced Materials* **22**, 1763–1766 (2010).
90. Yi, H. T., Choi, T., Choi, S. G., Oh, Y. S. & Cheong, S.-W. "Mechanism of the switchable photovoltaic effect in ferroelectric BiFeO_3 ". *Advanced Materials* **23**, 3403–3407 (2011).
91. Yang, S. Y., Seidel, J., Byrnes, S. J., Shafer, P., Yang, C.-H., Rossell, M. D., Yu, P., Chu, Y.-H., Scott, J. F., Ager, J. W., Martin, L. W. & Ramesh, R. "Above-bandgap voltages from ferroelectric photovoltaic devices". *Nature Nanotechnology* **5**, 143–147 (2010).

92. Seidel, J., Fu, D., Yang, S.-Y., Alarcón-Lladó, E., Wu, J., Ramesh, R. & Ager, J. W. "Efficient photovoltaic current generation at ferroelectric domain walls". *Physical Review Letters* **107**, 126805 (2011).
93. Alexe, M. & Hesse, D. "Tip-enhanced photovoltaic effects in bismuth ferrite". *Nature Communications* **2** (2011).
94. Bhatnagar, A., Roy Chaudhuri, A., Heon Kim, Y., Hesse, D. & Alexe, M. "Role of domain walls in the abnormal photovoltaic effect in BiFeO₃". *Nature Communications* **4**, 2835 (2013).
95. Yang, M.-M., Bhatnagar, A., Luo, Z.-D. & Alexe, M. "Enhancement of Local Photovoltaic Current at Ferroelectric Domain Walls in BiFeO₃". *Scientific Reports* **7**, 43070 (2017).
96. Kim, D. J. & Alexe, M. "Bulk photovoltaic effect in monodomain BiFeO₃ thin films". *Applied Physics Letters* **110**, 183902 (2017).
97. Sando, D., Carrétéro, C., Grisolia, M. N., Barthélémy, A., Nagarajan, V. & Bibes, M. "Revisiting the Optical Band Gap in Epitaxial BiFeO₃ Thin Films". *Advanced Optical Materials* **6**, 1700836 (2018).
98. Tablero, C. "An evaluation of BiFeO₃ as a photovoltaic material". *Solar Energy Materials and Solar Cells* **171**, 161–165 (2017).
99. Shockley, W. & Queisser, H. J. "Detailed Balance Limit of Efficiency of p–n Junction Solar Cells". *Journal of Applied Physics* **32**, 510–519 (1961).
100. Würfel, P. *Physik der Solarzellen 2*. [vollst. überarb.] Aufl. (Spektrum Akad. Verl., Heidelberg, 2000).
101. Grinberg, I., West, D. V., Torres, M., Gou, G., Stein, D. M., Wu, L., Chen, G., Gallo, E. M., Akbashev, A. R., Davies, P. K., Spanier, J. E. & Rappe, A. M. "Perovskite oxides for visible-light-absorbing ferroelectric and photovoltaic materials". *Nature* **503**, 509–512 (2013).
102. Nechache, R., Harnagea, C., Licoccia, S., Traversa, E., Ruediger, A., Pignolet, A. & Rosei, F. "Photovoltaic properties of Bi₂FeCrO₆ epitaxial thin films". *Applied Physics Letters* **98**, 202902 (2011).
103. Nechache, R., Harnagea, C., Li, S., Cardenas, L., Huang, W., Chakrabartty, J. & Rosei, F. "Bandgap tuning of multiferroic oxide solar cells". *Nature Photonics* **9**, 61–67 (2015).

CHAPTER 3

Thin Film Synthesis and Characterization Methods

3.1 Pulsed Laser Deposition

Pulsed laser deposition (PLD) was introduced as a new physical vapor deposition (PVD) evaporation technique to produce epitaxial thin films in the 1960s.¹ The interest of using PLD as sample synthesis method revitalized after the successful fabrication of high-temperature superconducting Y-Ba-Cu-O films in the late 1980s.² The highly localized and short heating of the single-source target material using a high-energy laser pulse in ns-range enables an (near-)stoichiometric material transfer in partial oxygen atmosphere. Because of these specifications, PLD is an established and versatile technique to produce complex oxide thin films.³

Figure 3.1a shows the PLD system (SURFACE systems+technology GmbH & Co. KG, Hueckelhoven, Germany) used to fabricate BiFeO_3 and $\text{Bi}_2\text{FeCrO}_6$ thin film heterostructures with optional conductive $\text{La}_{0.7}\text{Sr}_{0.3}\text{MnO}_3$ or SrRuO_3 intermediate electrode layer on single-crystalline substrates. The system is equipped with a KrF (248 nm) excimer laser (COMPexPro 201, Coherent Inc., Santa Clara, USA) and a high-pressure reflection high energy electron diffraction (RHEED) system. The PLD chamber is schematically shown in Figure 3.1b. The pulsed laser beam is focused on the ceramic or single-crystalline target material entering the chamber through an optical window. The target is mounted on the target carousel, enabling a superimposed rotating and toggling movement to ensure a uniform target ablation. The carousel can store four different targets selectable for multi-layer deposition. Each laser pulse with a duration of approximately 25 ns with a sufficiently high energy fluence heats the target material locally and creates a plasma plume as shown in Figure 3.1c,d. The plume rises to a heated single-crystalline substrate mounted on the substrate holder. The high-vacuum ($<10^{-6}$ mbar) is created by a turbomolecular pump and the background gas pressure inside the chamber can be adjusted by introducing gases through the gas inlet (oxygen, argon, nitrogen or a mixture). The introduction of oxygen as reactant gas to grow complex oxides is mandatory to avoid a high density of oxygen vacancies. Additionally, the presence of background gas reduces the kinetic energy of the plasma plume.³ After the deposition process, the oxygen content can be further increased to enable a fast cooling under high oxygen atmosphere and to minimize the occurrence of oxygen vacancies.

3. Thin Film Synthesis and Characterization Methods

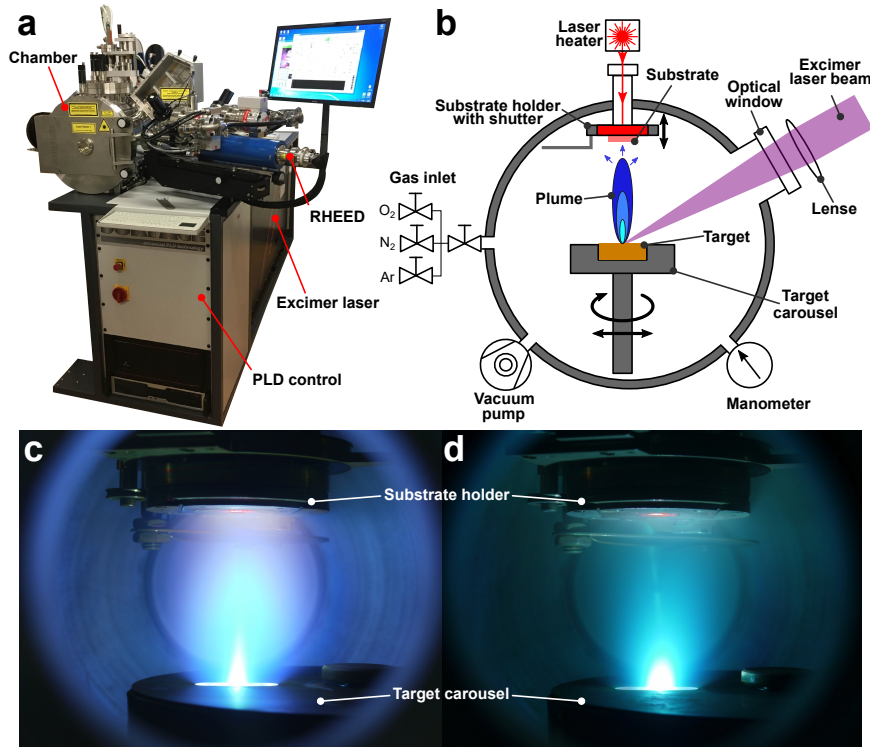


Figure 3.1: **a** Picture of the used PLD system. **b** Schematic of a PLD chamber with main components. Plasma plume of **c** BiFeO_3 and **d** $\text{Bi}_2\text{FeCrO}_6$ generated during thin film growth (photo exposure time 25 s at 2 Hz laser pulse frequency).

The essential growth parameters are the laser energy fluence (0.1 to 10 J cm^{-2}), the pulse frequency (1 to 10 Hz), the background gas pressure and composition ($<0.2 \text{ mbar}$), the substrate temperature ($<1100 \text{ }^\circ\text{C}$), and the substrate-target distance ($\sim 60 \text{ mm}$). Furthermore, the target quality is crucial and can differ with regard to its purity, density and grain size. Ceramic target materials might exhibit an excess of volatile components. Table 3.1 summarizes the used PLD growth parameter.

Table 3.1: Typical pulsed laser deposition growth parameter.

	BiFeO_3 (BFO)	$\text{Bi}_2\text{FeCrO}_6$ (BFCO)	$\text{La}_{0.7}\text{Sr}_{0.3}\text{MnO}_3$ (LSMO)	SrRuO_3 (SRO)
Target supplier	← Praxair Inc., Danbury, USA →			
Sample-target distance (mm)	← 60 →			
O_2 pressure (mbar)	0.145	0.01	0.2	0.067
Heating rate $<500 \text{ }^\circ\text{C}$ ($^\circ\text{C min}^{-1}$)	20	50	a	a
Heating rate $>500 \text{ }^\circ\text{C}$ ($^\circ\text{C min}^{-1}$)	10	50	a	a
Substrate temperature ($^\circ\text{C}$)	725 (625) ^b	700	650 (600) ^b	750
Pulse frequency (Hz)	2	2	2	1
Pulse energy (mJ)	135	135	120	105
Energy fluence (mJ cm^{-2})	1.3	1.3	1.16	1.01
Estimated growth rate (Å s^{-1})	0.46	0.67	0.71	0.38
Cooling rate $>500 \text{ }^\circ\text{C}$ ($^\circ\text{C min}^{-1}$)	20	20	a	a
Cooling rate $<500 \text{ }^\circ\text{C}$ ($^\circ\text{C min}^{-1}$)	20	5	a	a
Cooling O_2 pressure (mbar)	200	800	a	a

^a See corresponding BiFeO_3 or $\text{Bi}_2\text{FeCrO}_6$ parameter.

^b Different temperatures because of new heating and temperature readout system installation.

3.2 Substrate Selection & Treatment

BiFeO_3 and $\text{Bi}_2\text{FeCrO}_6$ films were grown on 500 μm -thick single-crystalline SrTiO_3 and DyScO_3 substrates (CrysTec GmbH, Berlin, Germany).

SrTiO_3 exhibits a cubic crystal structure with $a_c = b_c = c_c = 3.905 \text{ \AA}$.^{4,5} The orientation of the used polished substrates is $(001)_c$ inducing a compressive epitaxial strain to both BiFeO_3 and $\text{Bi}_2\text{FeCrO}_6$ as schematically shown in Figure 3.2a. Prior to deposition, the SrTiO_3 substrates are treated to achieve a single TiO_2 -terminated surface.^{6,7} The substrates were etched in a 1:20 solution of a commercial ammonium fluoride (AF)/hydrofluoric acid (HF) etch mixture (AF 87.5:12.5 HF (VLSI Selectipur, Art.: 51151613), BASF SE, Ludwigshafen, Germany) and de-ionized water for 30 s. The etching procedure was followed by an annealing step in ambient air atmosphere for 3 h at 1050 $^\circ\text{C}$.

The crystal structure of DyScO_3 is orthorhombic with $a_o = 5.440 \text{ \AA}$, $b_o = 5.717 \text{ \AA}$ and $c_o = 7.903 \text{ \AA}$.^{8,9} The surface normal of the substrate is along the $[110]_o$ -direction. Figure 3.2b demonstrates schematically the four pseudo-cubic BiFeO_3 unit cells accommodating at the $(110)_o$ surface of DyScO_3 . In this case, two different in-plane lattice parameter introduce a slightly bi-axial compressive strain to the BiFeO_3 film ($a_{pc} = \frac{1}{2} \sqrt{a_o^2 + b_o^2} = 3.946 \text{ \AA}$, $b_{pc} = \frac{1}{2} c_o = 3.952 \text{ \AA}$). The DyScO_3 substrates were treated for 3 h at 1000 $^\circ\text{C}$ in ambient air atmosphere. Thermal treatment of DyScO_3 $(110)_o$ substrates without additional wet-etching step has been demonstrated to create a single ScO_2 terminated surface.¹⁰

Both substrate types have a small miscut angle of 0.15-0.2 $^\circ$ resulting in the existence of atomic steps schematically shown in Figure 3.2c and visible in the AFM topography images of treated SrTiO_3 and DyScO_3 substrates in Figure 3.2d, respectively.

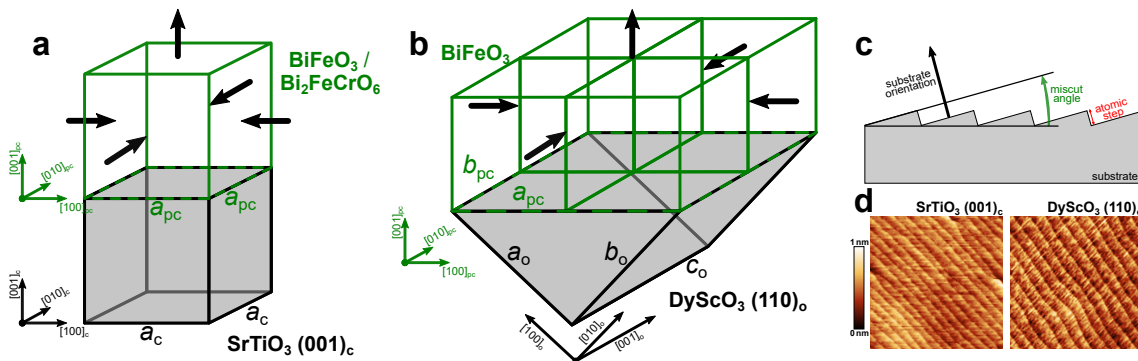


Figure 3.2: Epitaxial relation of film growth using **a** SrTiO_3 $(001)_c$ and **b** DyScO_3 $(110)_o$ single-crystalline substrates. **c** Schematic demonstrating the substrate miscut angle. **d** AFM topography image of SrTiO_3 $(001)_c$ (left) and DyScO_3 $(110)_o$ (right) substrates (miscut angle 0.15-0.2 $^\circ$, both images: $2 \times 2 \mu\text{m}^2$).

3.3 Electrode Structuring and Deposition

Electrodes were deposited on the film surface to enable (photo)electrical measurements. A spin-coating process (4000 RPM, 60 s) of a positive photo-resist layer (AR-P 3540T, Allresist GmbH, Strausberg, Germany) was followed by a soft-baking step on a hot plate (100 °C, 60 to 90 s). A direct-write photolithography machine (MicroWriter ML3, Durham Magneto Optics Ltd, UK) equipped with an ultra-violet (UV) light source was used to expose a programmable pattern to the spin-coated layer (exposure dose 125 to 140 mJ cm⁻²). After the exposure, the photo-resist layer was preserved using a developer (AR-300 44, Allresist GmbH).

For planar top electrode pairs (compare Figure 3.3a), a platinum-palladium alloy (Pt 80:20 Pd) was deposited on top of the structured photo-resist using a conventional direct current sputtering machine (108auto, Cressington Scientific Instruments Ltd, Watford, UK). The 120 s-deposition at an argon leakage pressure of 0.1 mbar with a set current of 40 mA resulted in an electrode thickness of ~60 nm. In₂O₃:Sn was used as transparent top electrode material, enabling (photo)electrical measurements in capacitor geometry (compare Figure 3.3b). To enable measurements throughout the film thickness, a conductive perovskite oxide layer was grown using PLD prior to the BiFeO₃/Bi₂FeCrO₆ thin film deposition. Radio-frequency (RF) sputtering was used to deposit a 125 nm-thick In₂O₃:Sn on the sample surface.

An ultra-sonic acetone bath was used to remove the photo-resist layer after the electrode material deposition.

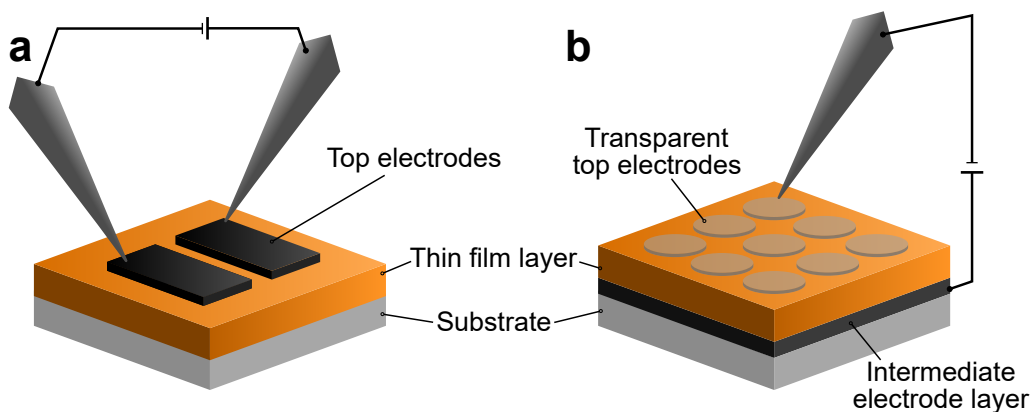


Figure 3.3: **a** Planar top electrode pair enabling in-plane electrical measurements. **b** Transparent circular top electrodes enabling measurement throughout film thickness in capacitor geometry (requires conductive layer between film and insulating substrate).

3.4 Scanning Probe Microscopy

Scanning probe microscopy (SPM) measurements were performed with two different systems (Asylum Research Cypher ES Environmental AFM, Oxford Instruments, UK & Park NX10, Park Systems Corp., South Korea). Detailed measurement information are given in the corresponding experimental sections in Chapter 4, 5 and 6.

SPM techniques are commonly used to investigate the topography and simultaneously functional properties of a sample. All techniques are based on a probe-surface interaction while scanning a certain area line by line. The use of a small probe, usually a nano-meter sharp tip at the end of a cantilever (spring), enables a high spatial resolution. Invented in 1981, scanning tunneling microscopy (STM) was the first implemented SPM technique.¹¹ Because of the limitation of STM to conductive samples, atomic force microscopy (AFM) was developed also enabling the measurement of insulating samples.^{12,13} The basic principle of AFM is shown in Figure 3.4a. A laser beam is positioned on the backside of the cantilever reflecting the beam to a photo diode. The approached probe interacts with the sample's surface and the interaction leads to a deflection of the cantilever. The sample is moved continuously along the fast scanning direction. The position along the slow scanning direction is changed stepwise to scan areas with dimensions typically in micrometer range. The movement is realized using a piezoactuator-driven stage. During scanning, the cantilever deflects and this leads to a shift of the laser beam position on the position-sensitive detector (PSD) diode, which is fed into a feedback loop to adjust the probe height returning to the initial deflection state. The adjustment, e.g. the voltage applied to the piezoactuator, can be used to track the height line profile along the fast scanning direction. After finishing one line, the probe shifts to the next line along the slow scanning direction.

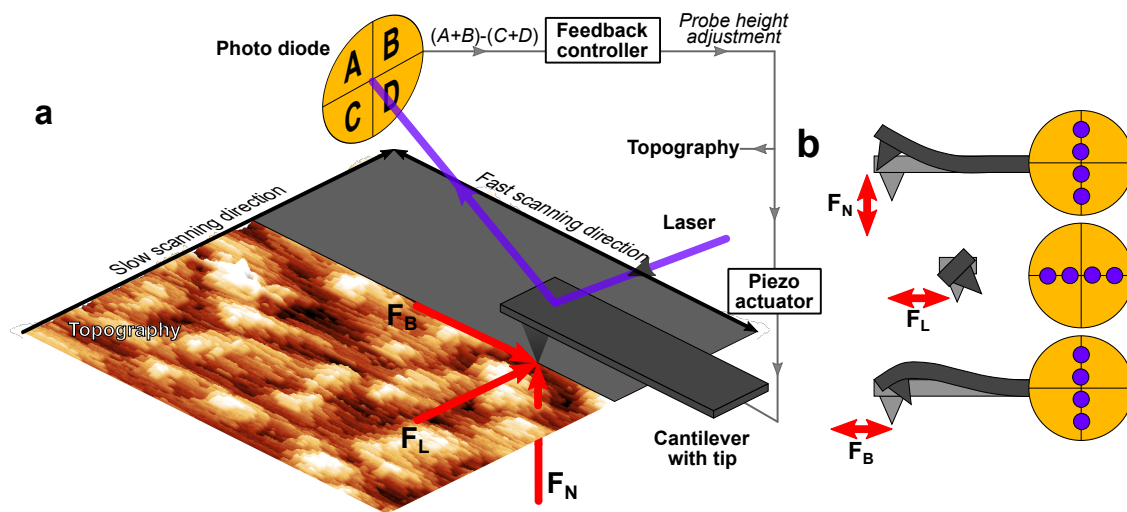


Figure 3.4: **a** Cantilever with sharp tip is approached to the surface of the sample, which is mounted on an XY-stage. While scanning the measurement area, the laser beam is reflected from the backside of the cantilever and any deflection is detected on the photo diode. The photo diode signal is transferred to a feedback control, which adjusts the probe height. The probe height (which is directly connected to the voltage applied to the piezo-actuator) is used to image the topography of the measurement area. **b** Normal force F_N , lateral force F_L and buckling force F_B act on the tip while scanning and lead to different kinds of cantilever deflection.

There are different forces acting on the probe while scanning, as shown in Figure 3.4b. The force normal to the surface F_N leads to a vertical shift of the laser spot position on a PSD diode. Depending on the orientation, the two lateral forces can either lead to a vertical or horizontal shift. The lateral force acting perpendicular to the cantilever F_T induces a torsion and the laser beam shifts horizontally on the photo

diode. The force F_B is oriented parallel to the cantilever and induces a buckling of the cantilever, resulting in a vertical shift, that interferes with the shift caused by F_N .

The normal force acting on the tip F_N can be qualitatively estimated using the Lennard-Jones potential V_{LN} as a function of the probe-sample distance r :¹⁴

$$F_N = \frac{dV_{LN}(r)}{dr} \quad \text{with } V_{LN}(r) = \underbrace{4\epsilon \left(\frac{\sigma}{r}\right)^{12}}_{\text{Pauli repulsion}} - \underbrace{4\epsilon \left(\frac{\sigma}{r}\right)^6}_{\text{Van-der-Waals attraction}} \quad (3.1)$$

whereas σ and γ are material-specific coefficients. V_{LN} is the sum of the short range Pauli repulsion and the long-range Van-der-Waals attraction.

AFM measurements can be performed using three different modes, namely non-contact, tapping and contact mode (compare Figure 3.5). The non-contact mode operates in the regime of strong attractive interaction. Without contacting the surface, the cantilever vibrates close to its resonance frequency with an amplitude of a few nanometers. Any change of the probe-sample distance changes the resonance frequency and oscillation amplitude. Either one can be used as feedback loop control parameter to readjust the probe height. While using non-contact operation mode, there is no tip degradation or sample damage. However, this mode is sensitive to adsorbates on the sample surface. Consequently, high resolution measurements need a high-vacuum environment. AFM measurements in tapping mode overcome this drawback. The mode is similar to the non-contact mode, however, the height of the oscillating probe is further reduced, so that the tip is partially contacting the sample surface. The operation in both regimes (attractive and repulsive forces) enables a better depth resolution while limiting the tip degradation due to a short probe-sample contact time. In contrast to the non-contact and tapping mode, the probe is not oscillating in the contact mode. The probe height is only in the regime of repulsive interaction and the tip is dragging the sample surface. While scanning, the cantilever bends, leading to a deflected laser beam position on the photo diode. This shift on the diode is used to readjust the probe height while keeping the applied force constant. With increasing magnitude of the applied force, both tip degradation and sample damage increase. However, for several functional AFM measurements (PFM, C-AFM), it is required to have a continuous probe-sample contact.

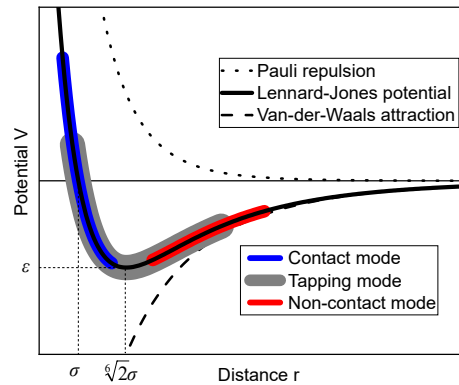


Figure 3.5: Lennard-Jones potential $V_{LN}(r)$ (solid line) as a sum of attractive Van-der-Waals (dashed line) and repulsive Pauli (dotted line) interactions. Highlighted regimes in which contact (blue), tapping (grey) and non-contact (red) modes are operating.

3.4.1 Piezo-response Force Microscopy

Piezo-response force microscopy (PFM) is an AFM extension developed to locally manipulate and characterize ferroelectric samples.¹⁵ The measurement principle is based on the converse piezoelectric effect, existing in all ferroelectrics (compare Section 2.1.1). The technique is used to extract information about the present domain configuration and local ferroelectric properties. The PFM working principle is schematically shown in Figure 3.6. A function generator applies an AC voltage V_{ac} with a frequency f_{ac} ranging from kHz to MHz from the approached conductive tip through the sample to a conductive bottom plate. The applied voltage provokes an alternating contraction and expansion of the piezoelectric material. A lock-in amplifier fixed to f_{ac} subtracts this vibration (usually in pm-range) from the overall response of the PSD diode.

In Figure 3.6b-e, the situation during a PFM measurement of a sample with two domains of opposed polarization direction is demonstrated. If the electric field is parallel (Figure 3.6b,e) or antiparallel (Figure 3.6c,d) to the polarization, there will be an expansion or contraction, respectively. The time-dependent responses are shown in Figure 3.6f. The amplitude of the vibration is the same for both domains. However, whereas the response of the domain with upward polarization is in phase, the response of the downward-polarized domain is shifted with regard to V_{ac} . This phase shift is extracted and used to determine and visualize the differently oriented domains. Phase shift and amplitude of the piezo-response as a function of the tip position x are shown in Figure 3.6g. Within the domain wall, the interface between the two domains, the phase shift rises from 0° to 180° . The amplitude drops within the domain wall and recovers back to the same value.

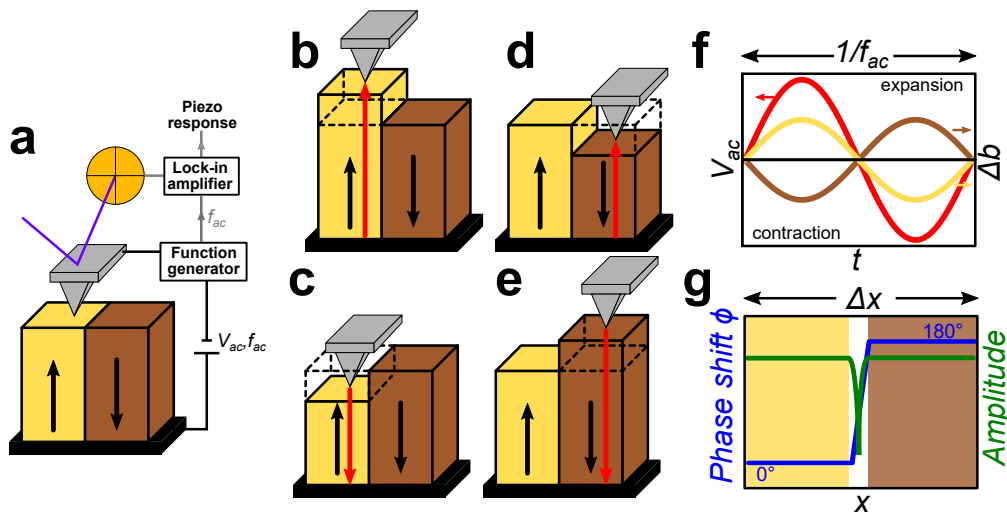


Figure 3.6: a PFM measurements require a function generator and lock-in amplifier in addition to the AFM setup. The working principle, based on the converse piezoelectric effect, is demonstrated with a simple two-domain structure (polarization up (yellow) and down (brown)). Electric fields pointing parallel to polarization provokes an expansion (b, e), antiparallel a contraction (c, d). f Because of the alternating orientation of the electric field (applied by the function generator), a vibration is provoked, whereas the vibration of the up-polarized and down-polarized domain is in-phase and phase-shifted, respectively. g During PFM measurements, the lock-in amplifier extracts both amplitude and phase of the piezo-response from the overall signal.

The scenario shown above only involves polarization pointing normal (vertical) to the sample's surface. Therefore, the visualization of the domains is realized using vertical piezo-response force microscopy (VPFM) in which the lock-in amplifier subtracts the response from the vertical photo diode signal $(A+B)-(C+D)$. In typical BiFeO_3 (BFO) and $\text{Bi}_2\text{FeCrO}_6$ (BFCO) thin films, there is an in-plane polarization component as well. In addition to VPFM, lateral piezo-response force microscopy (LPFM) measurements are needed to complete the information about the present domain configuration. In this scenario, the piezoresponse is subtracted from the lateral photo diode shift $(A+C)-(B+D)$. VPFM and LPFM measurements can be performed simultaneously using two separate lock-in amplifiers.

AFM, VPFM and LPFM images of a $\text{BiFeO}_3(200\text{ nm})//\text{DyScO}_3$ film simultaneously acquired in one scan are shown in Figure 3.7. The out-of-plane polarization component is uniformly down-polarized (compare Figure 3.7b). The LPFM phase and amplitude (Figure 3.7c,d) reveal a striped domain arrangement. The corresponding line scans in Figure 3.7e show that the phase changes clearly from one to the other stripe domain and the amplitude drops at domain walls (as described in Figure 3.6g). As demonstrated in Figure 3.7f, it is not possible to clearly identify the present domain variants. The result of the LPFM measurement depends on the orientation of the cantilever with respect to the polarization vector. Therefore, several LPFM measurements are needed to resolve the in-plane domain configuration, whereas the VPFM measurements are independent from the cantilever orientation.

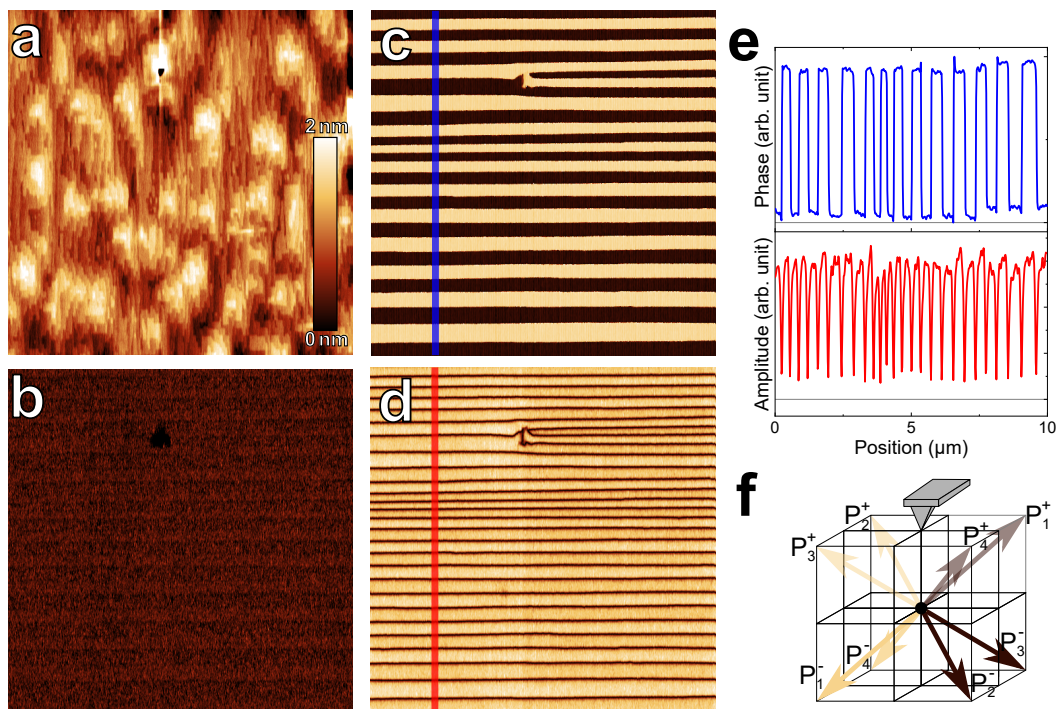


Figure 3.7: **a** Topography (RMS roughness ~ 0.20 nm), **b** VPFM phase, LPFM **c** phase and **d** amplitude images of a 200 nm thick BiFeO_3 on DyScO_3 . All images: $10 \times 10 \mu\text{m}^2$, $V_{ac} = 3$ V. **e** Schematic representation of distinguishable domain variants in used LPFM scanning configuration. **f** Line scan of LPFM phase and amplitude image, respectively.

The PFM mode can also be used to test the switchable character of the ferroelectric polarization. The results of a stationary spectroscopy measurement of a $\text{BiFeO}_3(200\text{ nm})/\text{La}_{0.7}\text{Sr}_{0.3}\text{MnO}_3//\text{DyScO}_3$ sample are shown in Figure 3.8a. The VPFM phase as a function of the bias voltage (top) clearly mimics the hysteretic behavior of the polarization (compare Figure 2.1a). At $+10\text{ V}$ and -10 V , the phase saturates indicating a complete reversal of the ferroelectric polarization. The VPFM amplitude as a function of the bias voltage (bottom) reveals a ferroelectric-characteristical "butterfly" loop.

The possibility of local modulation of the ferroelectric domain structure in PFM is demonstrated in Figure 3.8b-d. As indicated in the AFM topography image, an opposed bias voltages while scanning were applied to the area. The application of a -10 V pre-poling voltage created a uniform up-polarization and a subsequent $+10\text{ V}$ voltage were applied to write the letters 'ZIK' into the area. In doing so new domains and domain walls were created as demonstrated in VPFM phase and amplitude images (Figure 3.8c,d), respectively.

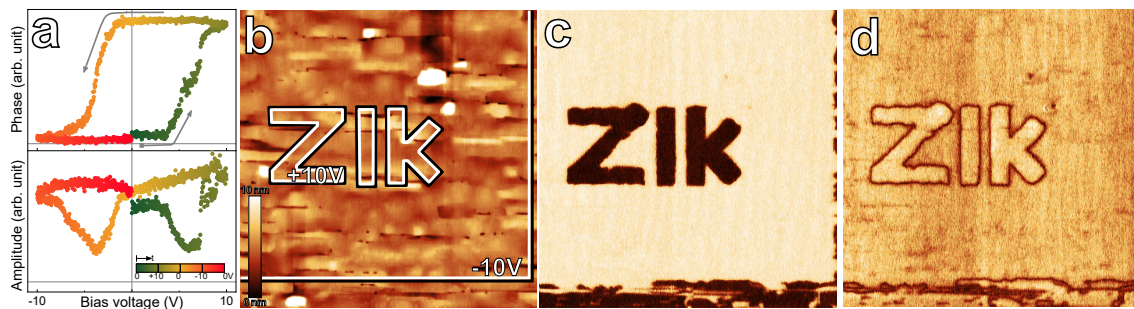


Figure 3.8: **a** VPFM phase (top) and amplitude (bottom) as a function of the applied (DC) bias voltage ($V_{ac} = 3\text{ V}$). **b** AFM topography image (RMS roughness 1.81 nm) with indication of manipulated areas (**ZIK**: $+10\text{ V}$, square: -10 V). VPFM **c** phase and **d** amplitude images after applying different bias voltages locally. All images: $10 \times 10\ \mu\text{m}^2$, $V_{ac} = 3\text{ V}$.

3.4.2 Conductive Atomic Force Microscopy

Conductive atomic force microscopy (C-AFM) is another AFM extension mode introduced to probe the local electrical resistance.¹⁶ Analogous to PFM, C-AFM requires a conductive tip and scanning in contact mode. Contrary to PFM, two separate detection systems are used to obtain information of both the topography and the electrical resistance simultaneously. In addition to the the laser-PSD-diode topography detection system, a current amplifier connected to the tip is tracking the current flow under an applied bias supplied from a voltage source. The used SPM system (Asylum Research Cypher ES Environmental AFM, Oxford Instruments, UK) is equipped with dual-gain optimized resistance conductance amplifier (ORCA). The C-AFM images shown in Section 6.2 are recorded with the high gain stage with a detectable current range of $\pm 10\text{ nA}$ and a typical noise amplitude of 3 pA .

3.5 X-ray Diffraction Analysis

Diffraction occurs when electromagnetic radiation of suitable wavelength λ interacts with periodic structures. In case of crystal structures with interatomic distances d of several angstroms ($1 \text{ \AA} = 0.1 \text{ nm}$), X-ray radiation with wavelengths ranging from several picometers to several nanometers is needed. The periodic arrangement of atoms acts as a three-dimensional diffraction grid. The analysis of resulting X-ray diffraction (XRD) patterns is widely used to characterize crystal structures. Depending on the orientation of the X-ray beam with respect to the crystal, destructive and constructive interference of light waves occur. Different X-ray intensities, depending on the orientation towards the atomic planes and their plane distance, can be detected. Bragg's law was postulated to describe the necessary condition for constructive interference:

$$n\lambda = 2d \sin \theta \quad n \in \mathbb{N}. \quad (3.2)$$

For specific incidence angles of the X-ray beam with respect to sample θ , Bragg's law (compare Figure 3.9a) is fulfilled and a diffraction peak appears. Waves reflected from two subsequent atomic planes will interfere constructively, if the path difference ($2d \sin \theta$) is equal to an integral multiple of the X-ray's wavelength.

Symmetric $2\theta/\omega$ scans are commonly used to prove the epitaxial relation between single-crystalline substrate and thin film. Figure 3.9b shows the schematic setup of XRD $2\theta/\omega$ measurements. The sample can be adjusted with three different rotational axes (ϕ , ψ , ω). ϕ and ψ are used to justify the sample along a crystallographic axis of the substrate, ω is used to tilt the sample and therefore to change the incidence angle of the X-ray beam during the measurement. For a change of the sample tilt $\Delta\omega$, the rotational position of the detector has to be moved by $2\Delta\omega = 2\theta$. Depending on the inter-atomic distances of planes parallel to the sample's surface, Bragg's law will be fulfilled during the scan and resulting in an intensity peak measured by the detector.

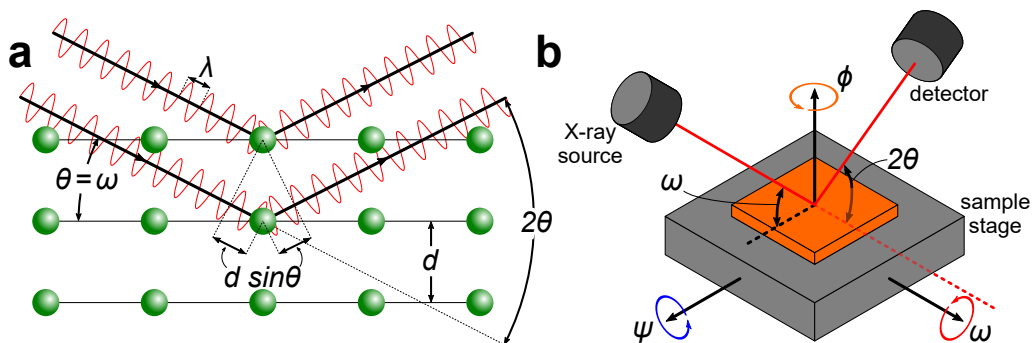


Figure 3.9: **a** Schematic demonstrating Bragg's law leading to constructive interference of two X-ray waves scattered at a crystal with periodic arranged atoms. **b** Schematic of X-ray diffraction measurement in $2\theta/\omega$ scan.

Whereas $2\theta/\omega$ scans can only provide information about the out-of-plane lattice spacing, additional information can be obtained by reciprocal space mapping/maps (RSM) measurements. RSM measurements allow to gain information about the in-plane lattice parameter and therefore about epitaxial relation between film and substrate or about the existence of different (ferroelastic) domain variants. By recording several asymmetric $2\theta/\omega$ scans with an offset angle $\alpha = \theta - \omega$, a Bragg plane that is

different to the plane parallel to the surface, can be selected. A high-resolution X-ray diffractometer (D8 Discover, Bruker Corporation, Billerica, USA) was used to acquire XRD data.

3.6 Photoelectrical Measurements

The BPV effect depends on the light polarization state (compare Section 2.3). The experimental setup shown in Figure 3.10a enables the adjustment of the laser beam light to any polarization state. The elliptical light polarization can be described by the ellipticity ratio ϵ (also known as polarization extinction ratio):

$$\epsilon = \frac{I_{major}}{I_{minor}} \quad (3.3)$$

I_{major} and I_{minor} are the light intensity along major and minor axis of the ellipse, respectively. There are two special cases of elliptical light polarization. Ideally, ϵ becomes infinite for purely linearly-polarized light, whereas it is $\epsilon = 1$ for purely circularly-polarized light or unpolarized light.

The illumination source is a diode laser (Cobolt 06-MLD, Cobolt AB, Solna, Sweden; $\lambda = 405$ nm, $P < 120$ mW, $d = 700$ μ m, $\epsilon = 200$). The following Glan-Thompson polarizer (GTH10M-A, Thorlabs Inc., New Jersey, USA) significantly increases the ellipticity ratio to $\epsilon = 1 \times 10^5$. An arbitrary light polarization state for a broad wavelength range can be set by a Berek variable wave plate (also known as Berek compensator)¹⁷ (5540M, Newport Corporation, Irvine, USA). The wave plate consists out of a single birefringent MgF₂ plate (ordinary and extraordinary refractive index n_o and n_e) with the extraordinary axis normal to the plate. Therefore, there is no retardation of light with normal incidence and the polarization state is not changing while passing the compensator (compare Figure 3.10b left). The ordinary and extraordinary ray experience the refractive index n_o . When increasing the tilt angle θ_R with respect to the light beam direction, the effective refractive index of the extraordinary beam n'_e changes (compare Figure 3.10b right):¹⁷

$$\frac{1}{n'_e} = \sqrt{\frac{\cos^2 \theta_R}{n_o^2} + \frac{\sin^2 \theta_R}{n_e^2}}. \quad (3.4)$$

An accurate rotation stage (red arrow in Figure 3.10a) enables a precise adjustment of the plate tilting and a continuous change of the retardation of the incoming light, thus the outgoing light polarization. A second rotation stage (green arrow in Figure 3.10a) enables to reorient the orientation of the birefringence fast axis.

A rotatable half-wave plate (WPH10M-405, Thorlabs Inc.) enables the subsequent reorientation of the light polarization ellipse (blue arrow in Figure 3.10a). To verify the outgoing light polarization, a second Glan-Thompson polarizer and a Si-based photo detector can be added to the setup. The ellipticity ratio ϵ as a function of the Berek compensator tilt θ_R is shown in Figure 3.10c. The polarization changes from linear ($\epsilon \approx 300$ for $\theta_R < 1.1^\circ$) to circular ($\epsilon \approx 1$ for $\theta_R \approx 5.2^\circ$). Elliptical polarization exists for intermediate tilts ($1.1^\circ < \theta_R < 5.2^\circ$). Depending on the orientation of the Berek compensator's fast axis, the chirality of the elliptical and circular light polarization is right-handed (red) or left-handed (blue).

3. Thin Film Synthesis and Characterization Methods

The sample is mounted on an XY-stage with micrometer screws enabling the positioning of the laser beam spot with respect to the electrodes. The electrical connection is realized with two sharp probing tips. These are connected to a source measure unit (SMU) device (6517B electrometer or 2450 sourcemeter, Keithley Instruments Corporation, Solon, USA).

Measurements under 1.5AM illumination were performed using a separate setup without the optical components shown in Figure 3.10a,b. A diode-based solar simulator (SINUS-70, WAVELABS Solar Metrology Systems GmbH, Leipzig, Germany) with a calibrated spectrum was used as the illumination source.

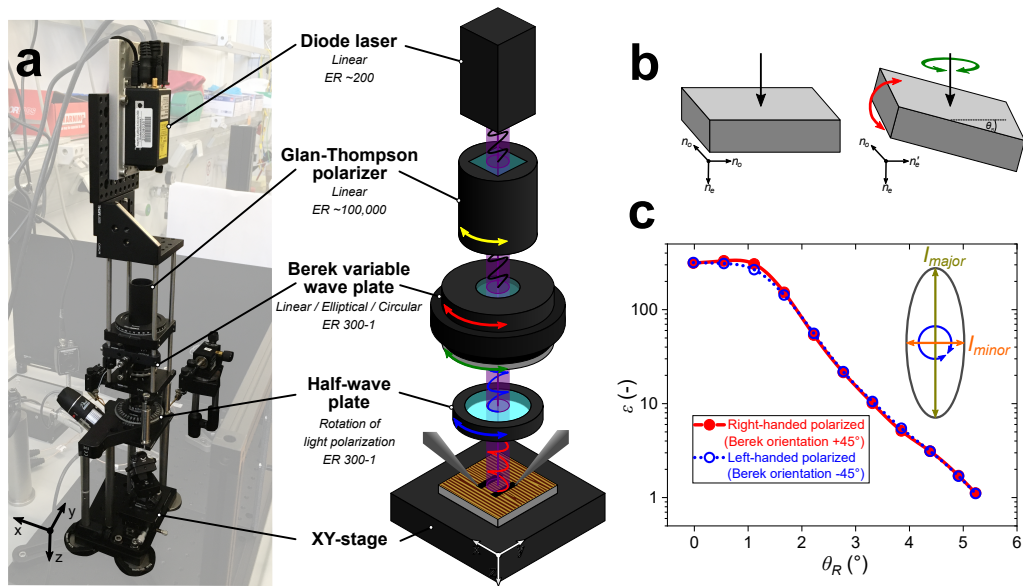


Figure 3.10: **a** Experimental setup for bulk photovoltaic measurements with a diode laser, a Glan-Thompson polarizer, a Berek variable wave plate and a half-wave plate. The sample is mounted on a XY-stage and two probes are used to contact the electrodes to the SMU device. **b** Untilted and tilted Berek compensator¹⁷ **c** Ellipticity ratio ϵ as a function of the Berek compensator tilt angle σ_R measured by replacing the sample with a second Glan-Thompson polarizer and Si-based photo detector.

References - CHAPTER 3

1. Smith, H. M. & Turner, A. F. "Vacuum Deposited Thin Films Using a Ruby Laser". *Applied Optics* **4**, 147 (1965).
2. Dijkkamp, D., Venkatesan, T., Wu, X. D., Shaheen, S. A., Jisrawi, N., Min-Lee, Y. H., McLean, W. L. & Croft, M. "Preparation of Y–Ba–Cu oxide superconductor thin films using pulsed laser evaporation from high T_c bulk material". *Applied Physics Letters* **51**, 619–621 (1987).
3. *Pulsed laser deposition of thin films: Applications-led growth of functional materials* (ed Eason, R.) (Wiley-Interscience, Hoboken, NJ, 2007).
4. Lytle, F. W. "X-Ray Diffractometry of Low-Temperature Phase Transformations in Strontium Titanate". *Journal of Applied Physics* **35**, 2212–2215 (1964).
5. Uecker, R., Bertram, R., Brützam, M., Galazka, Z., Gesing, T. M., Guguschev, C., Klimm, D., Klupsch, M., Kwasniewski, A. & Schlom, D. G. "Large-lattice-parameter perovskite single-crystal substrates". *Journal of Crystal Growth* **457**, 137–142 (2017).
6. Kawasaki, M., Takahashi, K., Maeda, T., Tsuchiya, R., Shinohara, M., Ishiyama, O., Yonezawa, T., Yoshimoto, M. & Koinuma, H. "Atomic Control of the SrTiO₃ Crystal Surface". *Science* **266**, 1540–1542 (1994).
7. Koster, G., Kropman, B. L., Rijnders, G. J. H. M., Blank, D. H. A. & Rogalla, H. "Quasi-ideal strontium titanate crystal surfaces through formation of strontium hydroxide". *Applied Physics Letters* **73**, 2920–2922 (1998).
8. Veličkov, B., Kahlenberg, V., Bertram, R. & Bernhagen, M. "Crystal chemistry of GdScO₃, DyScO₃, SmScO₃ and NdScO₃". *Zeitschrift für Kristallographie* **222**, 466–473 (2007).
9. Uecker, R., Veličkov, B., Klimm, D., Bertram, R., Bernhagen, M., Rabe, M., Albrecht, M., Fornari, R. & Schlom, D. G. "Properties of rare-earth scandate single crystals (Re=Nd–Dy)". *Journal of Crystal Growth* **310**, 2649–2658 (2008).
10. Dirsyte, R., Schwarzkopf, J., Wagner, G., Fornari, R., Lienemann, J., Busch, M. & Winter, H. "Thermal-induced change in surface termination of DyScO₃(110)". *Surface Science* **604**, L55–L58 (2010).
11. Binnig, G. & Rohrer, H. "Scanning tunneling microscopy". *Surface Science* **126**, 236–244 (1983).
12. Binnig, Quate & Gerber. "Atomic force microscope". *Physical Review Letters* **56**, 930–933 (1986).
13. Meyer, G. & Amer, N. M. "Novel optical approach to atomic force microscopy". *Applied Physics Letters* **53**, 1045–1047 (1988).
14. Kittel, C. *Introduction to solid state physics* Global edition, [9th edition] (Wiley, Hoboken, NJ, 2018).
15. Güthner, P. & Dransfeld, K. "Local poling of ferroelectric polymers by scanning force microscopy". *Applied Physics Letters* **61**, 1137–1139 (1992).

16. Murrell, M. P., Welland, M. E., O'Shea, S. J., Wong, T. M. H., Barnes, J. R., McKinnon, A. W., Heyns, M. & Verhaverbeke, S. "Spatially resolved electrical measurements of SiO₂ gate oxides using atomic force microscopy". *Applied Physics Letters* **62**, 786–788 (1993).
17. Berek, M. in *Centralblatt für Mineralogie, Geologie und Paläontologie* (eds Bauer, M., Frech, F. & Liebisch, T.) 388, 427, 464, 580 (E. Schweizerbart'sche Verlagshandlung, 1900-1924, Stuttgart, 1913).

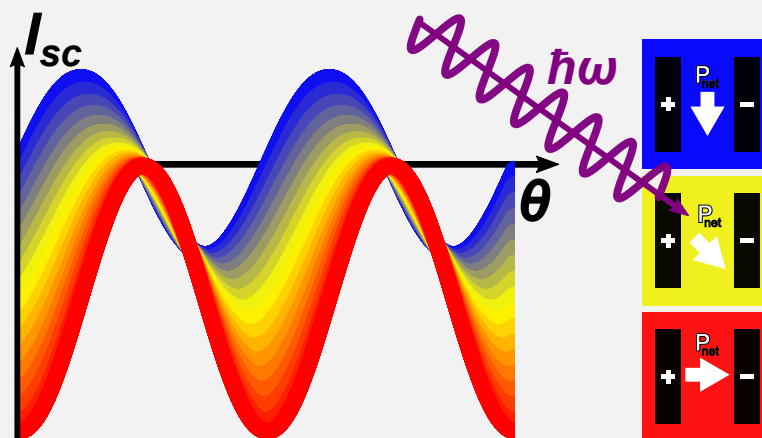
CHAPTER 4

Domain and Switching Control of the Bulk Photovoltaic Effect in Epitaxial BiFeO₃ Thin Films

The non-centrosymmetric crystal structure is the underlying origin of ferroelectricity and the BPV effect. Consequently, both physical quantities are inextricably linked. The first aim of the initial part of this thesis was to explore the intrinsic link between ferroelectricity and the BPV effect; more precisely, the linear BPV effect (compare Section 2.3). For this, systematic light-polarization-dependent photoelectrical measurements of BiFeO₃ thin films with unordered and ordered ferroelectric domain structure were performed. Another logical consequence of this link is the simultaneous modulation of both the ferroelectric polarization and the BPV effect under high electrical fields. Therefore, the second aim was the demonstration of the continuous electric-field adjustability of both quantities and characterize the switching behavior.

PUBLISHED AS:

Knoche, David S., Yun, Y., Ramakrishnegowda, N., Mühlenbein, L., Li, X. & Bhatnagar, A. "Domain and Switching Control of the Bulk Photovoltaic Effect in Epitaxial BiFeO₃ Thin Films". *Scientific Reports* **9**, 13979 (2019)



ToC Figure 4.0: Schematic demonstration of the adjustability of the bulk photovoltaic effect: Short-circuit current I_{sc} as a function of linear light polarization orientation angle θ undergoes a offsetting and phase shifting (left) while the ferroelectric polarization P_{net} is rotated as high electric fields are applied (right).

OPEN

Domain and Switching Control of the Bulk Photovoltaic Effect in Epitaxial BiFeO₃ Thin Films

David S. Knoche, Yeseul Yun, Niranjana Ramakrishnegowda, Lutz Mühlenbein, Xinye Li & Akash Bhatnagar

Received: 28 March 2019
Accepted: 6 September 2019
Published online: 27 September 2019

Absence of inversion symmetry is the underlying origin of ferroelectricity, piezoelectricity, and the bulk photovoltaic (BPV) effect, as a result of which they are inextricably linked. However, till now, only the piezoelectric effects (inverse) have been commonly utilized for probing ferroelectric characteristics such as domain arrangements and resultant polarization orientation. The bulk photovoltaic effect, despite sharing same relation with the symmetry as piezoelectricity, has been mostly perceived as an outcome of ferroelectricity and not as a possible analytical method. In this work, we investigate the development of BPV characteristics, i.e. amplitude and angular dependency of short-circuit current, as the ferroelastic domain arrangement is varied by applying electric fields in planar devices of BiFeO₃ films. A rather sensitive co-dependency was observed from measurements on sample with ordered and disordered domain arrangements. Analysis of the photovoltaic response manifested in a mathematical model to estimate the proportion of switched and un-switched regions. The results unravel the potential utility of BPV effect to trace the orientation of the polarization vectors (direction and amplitude) in areas much larger than that can be accommodated in probe-based techniques.

The observation of the photovoltaic (PV) effect in BiFeO₃ (BFO) has revitalized interests in the field of photo-ferroics, i.e. in the interplay between ferroic orders and photo-electronic characteristics. The possibility to tune one by the other has laid the platform to conceptualize novel opto-electronic devices. Several investigations have considered the role of depolarization field and band bending at the electrode-film interface in separating the charge carriers for the resultant PV effect^{1–4}. As a consequence, the PV effect in BFO has been demonstrated to be affected by the state of ferroelectric polarization^{4–6}. This aspect has been conversely utilized to read the change in the state of polarization, i.e. up to down or vice versa⁷. However, for certain applications, mere knowledge about the sign of polarization is not sufficient, and information about the orientation is equally desired. This is particularly true for planar devices wherein the electric fields are applied in-plane. For instance, functioning of BFO-based magneto-electric devices largely depends upon the canted magnetic moment that is associated with the in-plane projection of the polarization⁸. Stripe-patterned ferroelastic domains separated by 71° domain walls in BFO films, with a large in-plane polarization component, have been successfully utilized to align the magnetic easy axis of the ferromagnetic top layer^{9,10}. Recent discovery pertaining to electric field control of skyrmions in bi-layered heterostructures will motivate further research in such devices¹¹. In all of these scenarios, knowledge about the in-plane polarization in terms of magnitude and orientation is necessary. Scanning probe techniques are typically used for this purpose, albeit with measurable areas limited to few tens of micrometers. Lately, second harmonic generation (SHG) has been also explored to detect the orientation of the in-plane polarization component¹². Here, the absence of inversion symmetry in ferroelectric materials causes the impinging light waves to undergo frequency doubling. The emitted light wave can then be resolved to extract information about the polarization state, and distinguish between ordered and disordered domain configurations^{12,13}.

Interestingly, another consequence of the absence of inversion symmetry is the generation of shift photocurrents under appropriate illumination¹⁴. The resultant photovoltaic effect is referred to as bulk photovoltaic (BPV) effect, and exhibits anomalous characteristics such as open-circuit voltages (V_{oc}) that can well exceed the band gap of the material¹⁵. The photoresponse can be represented in the form of a tensor, which is analogous to the piezoelectric tensor and derived from the crystal symmetry. One of the critical consequences is the dependency of

Zentrum für Innovationskompetenz SiLi-nano, Martin-Luther-Universität Halle-Wittenberg, Halle (Saale), 06120, Germany. Correspondence and requests for materials should be addressed to A.B. (email: akash.bhatnagar@physik.uni-halle.de)

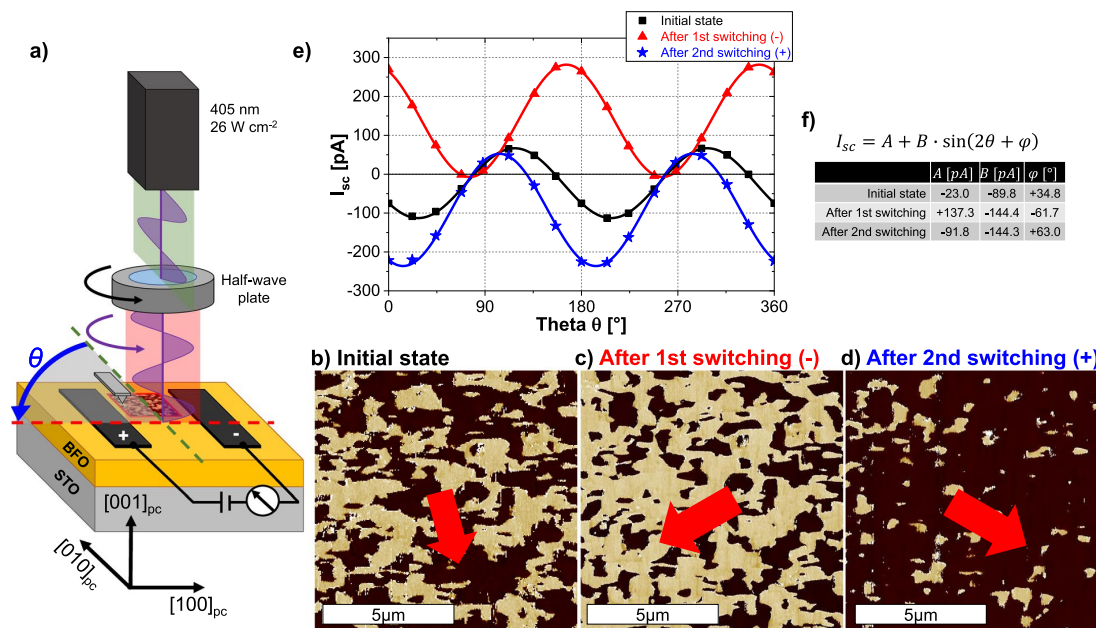


Figure 1. (a) Schematic setup of the measurements on BFO/STO: Orientation of linearly polarized laser light (green) is rotated by a half-wave plate by the angle θ (red). The beam spot is placed in between the electrodes, which are running along $[010]_{pc}$. LPFM phase image (PFM probe along $[010]_{pc}$, $10 \times 10 \mu\text{m}^2$) of (b) the initial state, (c) after applying negative and (d) after applying positive electric fields, respectively. Red arrows indicate the direction of P_{net} . (e) I_{sc} as a function of θ for the state shown in (b–d). Solid lines depict the fit of the data points with Eq. (1). (f) Values of A , B and φ extracted from fitting.

the PV current on the orientation of the linearly polarized light with respect to the measurement gap, and on BPV tensor coefficients β_{ij} . In the case of single domain samples, and measurement along the polar axis, sinusoidal and cosinusoidal dependencies have been observed with a single tensor coefficient (β_{22}) acting as a proportionality constant¹⁶. However, in the case of samples with poly-domain configurations, the resultant response can have contributions from multiple tensor coefficients. Mathematically it has been shown that the arrangement of polarization vectors of different domains results in such non-trivial solutions¹⁷. Therefore, it can be perceived that any change in the domain arrangement and net polarization will directly impact the BPV response. Conversely, the BPV effect can be also used to determine the domain arrangement and the effective state of polarization.

Till now, the BPV effect has been mostly studied in relation to single domain states with emphasis only on the observation rather than manipulation. In this work, we analyze the evolution of the BPV effect as the domains are switched upon the application of electric fields. The defining characteristics of the short-circuit current (I_{sc}), viz. magnitude and angular dependence, were found to be surprisingly sensitive to the rotation of the in-plane net polarization (P_{net}). Our analysis henceforth unravels the potential utility of the BPV effect in determining the orientation of P_{net} in areas of size that are not typically measurable with probe-based methods. We use planar top electrodes separated by a gap, which allows to observe the domain configuration using piezoresponse force microscopy (PFM) and to measure the corresponding BPV characteristics. Experiments were conducted with disordered and ordered domain arrangements.

Results

BFO films with a thickness of ~ 220 nm were deposited on (001) oriented SrTiO₃ (STO) and (110) oriented DyScO₃ (DSO) substrates using pulsed laser deposition. The respective samples will be referred to as BFO/STO and BFO/DSO. The resultant topography of the samples and the corresponding X-ray diffraction $2\theta/\omega$ -scans prove the epitaxial relation between the film and substrate. The details are provided in Supplementary Fig. S1. Planar electrodes, with a length of $950 \mu\text{m}$ and separated by approximately $40 \mu\text{m}$, were fabricated on the surface of the samples. The setup of the photoelectrical (PE) and PFM measurements is shown schematically in Fig. 1a. PE measurements were performed at room temperature with a diode laser of wavelength 405 nm (3.05 eV) as the illumination. The orientation of the linearly polarized light was rotated using a half-wave plate. The angle θ represents the orientation of electric field plane of the light with respect to the $[010]_{pc}$ direction. The short-circuit current I_{sc} can be represented with the following equations¹⁷:

$$\begin{aligned} \mathbf{P}_{\text{net}} \parallel \text{electrodes} \quad I_{\text{sc}}(\theta) &= EA_{\text{cs}} \left(\frac{\beta_{33}}{3\sqrt{3}} - \frac{\beta_{31}}{3\sqrt{3}} + \frac{2\beta_{22}}{3\sqrt{6}} + \frac{\beta_{15}}{3\sqrt{3}} \right) \sin(2\theta + \varphi) \\ &= A + B \sin(2\theta + \varphi) \end{aligned} \quad (1)$$

$$\begin{aligned} \mathbf{P}_{\text{net}} \perp \text{electrodes} \quad I_{\text{sc}}(\theta) &= EA_{\text{cs}} \left(\frac{\beta_{33}}{3\sqrt{3}} + \frac{2\beta_{31}}{3\sqrt{3}} - \frac{\beta_{22}}{3\sqrt{6}} + \frac{\beta_{15}}{3\sqrt{3}} \right) \\ &\quad + EA_{\text{cs}} \left(\frac{2\beta_{22}}{\sqrt{6}} + \frac{\beta_{15}}{\sqrt{3}} \right) \sin(2\theta + \varphi) \\ &= C + D \sin \left(2\theta + \frac{\pi}{2} + \varphi \right) \\ &= C + D \cos(2\theta + \chi) \end{aligned} \quad (2)$$

The equations have been derived for BFO films with an ordered array of domains that are separated by 71° domain walls. To simplify the equations, we have replaced the associated constants, namely, BPV coefficients β_{ip} , light intensity E and the cross-sectional area A_{cs} , with condensed notations B , C and D . Angles φ and χ have been added in Eqs (1) and (2), respectively, to incorporate any tilt of P_{net} with respect to the electrodes. In addition, A has been included as an offset in Eq. (1), and bears no physical relevance.

Due to the in-plane compressive strain and homogeneous TiO₂ termination of the STO substrate, only four out of the eight possible domain variants are present that are uniformly aligned along the out-of-plane direction^{18–20} and the out-of-plane component of the polarization does not change throughout our experiments. Therefore, only the lateral PFM (LPFM) phase images will be henceforth presented. Figure 1b shows the disordered domain arrangement in the initial state of the BFO/STO sample wherein the ratio of dark to bright regions is ~55:45. An additional LPFM phase image was acquired with the cantilever aligned along the [100]_{pc} direction and is shown in Supplementary Fig. S2. The dark-to-bright ratio is around ~65:35. It can be inferred from these images that P_{net} is tilted within the electrode gap, as indicated by the red arrow in Fig. 1b. The subsequent PE measurement (Fig. 1e, black) resulted in an I_{sc} and V_{oc} that varies as the electric field plane of the light is rotated by an angle θ (V_{oc} values of the investigated samples can be found in Supplementary Fig. S3). This proves the dominance of the BPV effect in these samples. The variations in I_{sc} are in good agreement with Eq. (1) which describes the PV current when P_{net} is parallel to the electrodes. The measured values of the current were analyzed with Eq. (1) and the respective coefficients extracted from the fitting are summarized in Fig. 1f. The values of φ , A and B are 35°, 23 pA and 89.9 pA, respectively. The non-zero value of coefficient A and the substantial value of φ suggest a tilt of P_{net} with respect to the electrodes, as was also inferred from the PFM analysis. In the next step, electric fields were applied across the electrodes to rearrange the domain configuration and associated P_{net} . Negative fields were applied and PFM scans were acquired from the same area as in Fig. 1b. The LPFM phase image (Fig. 1c) clearly depicts an evident reduction of the dark-to-bright ratio which confirms the tendency of P_{net} to align with the direction of the electric field. The subsequent PE measurement reveals a shift of $I_{\text{sc}}(\theta)$ along the y - and x -axis (Fig. 1e, red). The coefficients A and φ undergo a change in their respective signs, while B attains a higher value. An increment in B is related to an overall higher magnitude of P_{net} which is manifested by a higher ordering of the domains after the switching process. On the other hand, φ approaches 90° in conjunction with a higher value of A . Therefore, the PV response seems more alike the relation given in Eq. (2), which is valid when P_{net} is perpendicular to the electrodes. Thereafter, positive electric fields were applied and the rearranged domain configuration from the same area is shown in Fig. 1d. Apparently, the dark-to-bright ratio exceeds the value of the initial state. The analysis of the PV response with Eq. (1) results in a similar value of B suggesting a nearly unchanged magnitude of P_{net} . Coefficients φ and A undergo a change of sign which largely emulates a flip of P_{net} to align along the direction of the electric field, although the magnitudes slightly differ. A possible reason for the difference could be a non-uniform switching arising from inhomogeneous electric fields close to the edges of the surficial top electrodes²¹ and the large size of the gap. From these observations it can be proposed that the analysis of the BPV response with Eqs (1) and (2) present an efficient framework to determine the orientation of the polarization. The extracted coefficients contain information about the orientation and magnitude of P_{net} . Also, noteworthy to mention is the size of the gap under consideration, $40 \times 950 \mu\text{m}^2$, which is much larger than the areas typically measurable in a single image scan of a probe-based technique such as PFM. However, to gain further insight into the intricate correlations, it is imperative to study the PV response from samples which have a long-range ordering of domains with a known direction of P_{net} .

For this purpose, BFO films grown on DSO substrates, exhibiting 71° domain walls and P_{net} pointing along the [010]_{pc}-direction, were used. Prior investigations were performed to determine the direction of the polarization, and electrodes were aligned perpendicular (PPP configuration) and parallel (PPL configuration) to P_{net} . Figure 2a schematically depicts the PE and PFM measurement in the PPP configuration. Figure 2b is a representative LPFM image acquired from in between the gap with the PFM probe aligned along [100]_{pc}. The uniform color confirms the direction of P_{net} perpendicular to the electrodes. The typical stripe-like pattern associated with the 71° domain walls was also imaged but with the probe aligned along [010]_{pc}, and will be discussed later. The PE measurement from the initial state demonstrates a rather excellent agreement between the I_{sc} and Eq. (2) (Fig. 2f,g), with the angular offset χ bearing a minimal value of 2°.

Thereafter, the gap was switched to an intermediate state to have a nearly equal proportion of areas with oppositely aligned P_{net} s, as shown in Fig. 2c. Additional LPFM images revealing the presence of a global domain wall between switched and unswitched regions are shown in Supplementary Fig. S4. The resultant PV response loses

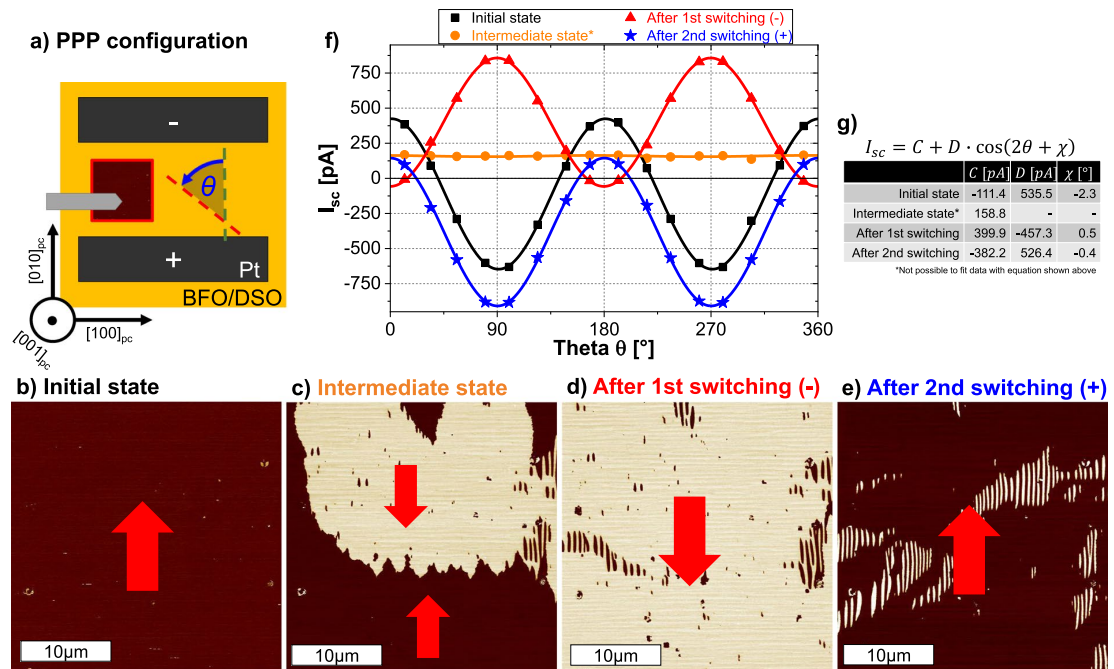


Figure 2. (a) Schematic setup of the measurements in the PPP configuration (P_{net} perpendicular to electrodes) on BFO/DSO. LPFM phase image (PFM probe along $[100]_{pc}$, $30 \times 30 \mu\text{m}^2$) (b) of the initial state, (c) of intermediate state (negative electric fields applied), (d) after applying higher negative and (e) after applying positive electric fields, respectively. Red arrows indicate the direction of P_{net} . (f) I_{sc} as a function of θ for the state shown in (b–e). Solid lines depict the fit of the data points with Eq. (2). (g) Values of C , D and χ extracted from fitting.

the cosinusoidal θ -dependency and a steady I_{sc} of around 160 pA was measured. The comparison with Eq. (2) suggests an apparent drop in the value of D , which comprises of β_{22} and β_{15} . The measured I_{sc} can then be attributed primarily to the θ -independent quantity C which has additional contributions from β_{31} and β_{33} . Subsequently, higher electric fields were applied with the objective to completely switch the gap, and the LPFM phase image in Fig. 2d confirms this scenario. The corresponding PV response regains the cosinusoidal dependency on θ with coefficients C and D bearing high values, and χ assuming a value of 180° implying a complete inversion of P_{net} . The variation in the values of D (i.e. 535 pA in the initial state \rightarrow zero in the intermediate state \rightarrow -457 pA after first switching) clearly mimics the magnitude of P_{net} . To further confirm this, electric fields were applied to switch the gap back to the initial state (Fig. 2e). As expected, a nearly identical value of D was obtained. The relevance of C is also worthy to be mentioned. The sign of C clearly follows the direction P_{net} , but the value seems to have a correlation with the domain width (size of domain in the $[010]_{pc}$ -direction) which was observed to be significantly larger as new domains were formed (see Supplementary Fig. S5). Thus it can be concluded that the switching process in the PPP configuration does not involve any substantial rotation of P_{net} . The antiparallel and parallel alignment of the electric field with respect to P_{net} only leads to a lowering and subsequent gain of the magnitude of P_{net} .

For the next set of experiments, the PPL configuration (Fig. 3a) was used, which apparently also allowed us to observe and investigate the rotation of P_{net} . The initial state of the gap was confirmed to have P_{net} aligned parallel to the electrodes with the imaging of long stripe like patterned domains along $[100]_{pc}$ (Fig. 3b). As a result, the PV response was found to be in good agreement with Eq. (1) with minimal values of coefficient A and angle φ of around 11 pA and 5° , respectively. Upon the application of a moderate electric field, the P_{net} in some regions aligns along the electric field, while in other regions remains unchanged (Fig. 3c). Therefore, the gap adopts an intermediate state with P_{net} tilted by an angle of $\sim 45^\circ$. Precisely this scenario is also visible in the PV response wherein the angle φ assumes a value of 48.1° . As higher fields are applied, the gap uniformly switches (Fig. 3d) and the PV response changes from sinusoidal to cosinusoidal shape. This change is related to an orthogonal rotation of P_{net} and is illustrated by the change of φ to 82.6° and A assuming a non-negligible value of -289 pA. Applying electric fields of opposite polarity confirms this (Fig. 3e), and likewise the PPP case, a PV response with similar values of A and B is observed with $\varphi = 89.7^\circ$. It is evident from these measurements, that the electric field forces P_{net} to re-orient stepwise from the parallel to a perpendicular configuration. This situation can be effectively modeled by combining Eqs (1) and (2). The resultant equation is of the type:

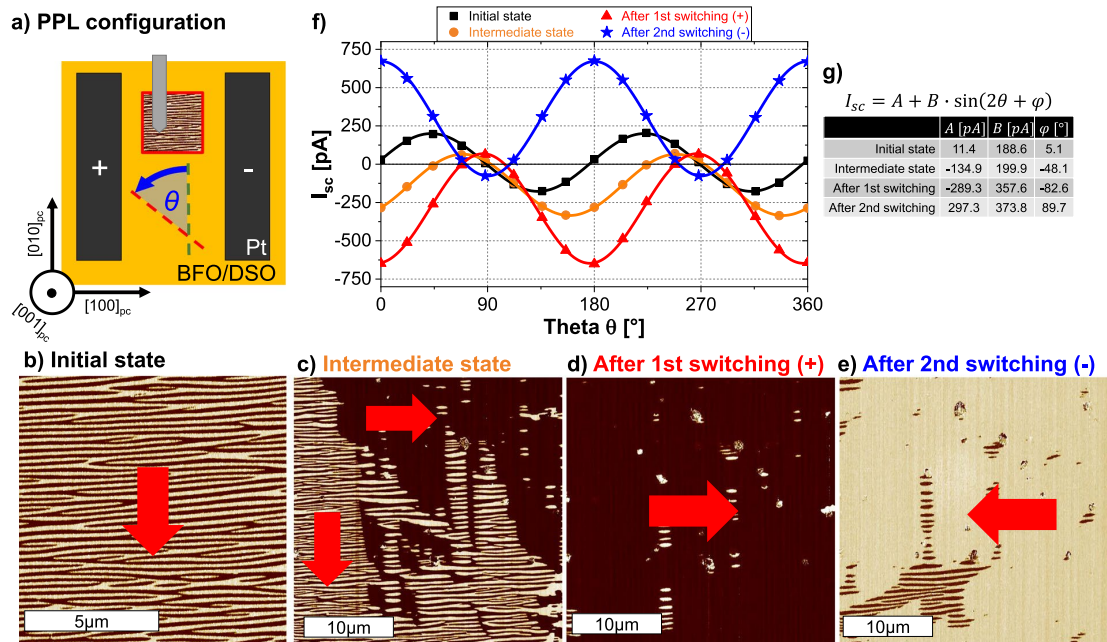


Figure 3. (a) Schematic setup of the measurements in the PPL configuration (P_{net} parallel to electrodes) on BFO/DSO. LPFM phase image (PFM probe along $[100]_{pc}$) (b) of the initial state, (c) of intermediate state (negative electric fields applied), (d) after applying higher negative and (e) after applying positive electric fields, respectively. Red arrows indicate the direction of P_{net} . (f) I_{sc} as a function of θ for the state shown in (b–e). Solid lines depict the fit of the data points with Eq. (1). (g) Values of A, B and φ extracted from fitting.

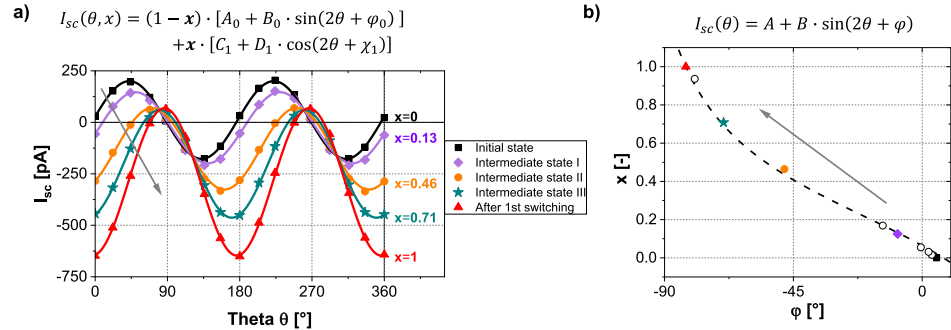


Figure 4. (a) I_{sc} as a function of θ in the initial state (black), in the intermediate state (purple, orange, green) and after applying the highest (positive) electric field (red). Data points correspond to the PE measurements at certain angles θ fitted with Eq. (3) (solid lines). Parameter x represents the extent of switching. (b) The extent of switching x plotted as a function of the angle φ (acquired from fitting measured values with Eq. (1)) for the initial state, several intermediate states, and the state after the first switching. The fit emphasizes the possibility to use φ as a probing parameter to measure the extent of switching and thus the tilt of P_{net} (Derivation of fitting function can be found in the Supplementary Information).

$$I_{sc}(\theta, x) = (1 - x) \cdot [A_0 + B_0 \sin(2\theta + \varphi_0)] + x \cdot [C_1 + D_1 \cos(2\theta + \chi_1)] \quad (3)$$

wherein x and $(1 - x)$ represent the fraction of area with changed and unchanged orientation of P_{net} , respectively. To investigate the validity of this relation, first, a series of PE measurements were conducted to acquire PV responses from differently switched states of the gap. The values of the coefficients A_0 , B_0 , φ_0 and C_1 , D_1 , χ_1 were determined from the initial (PPL) and final (PPP) state, respectively. Thereafter, all the responses were analyzed with Eq. (3), by keeping the coefficients fixed and allowing the variation of only x . All of the acquired PV responses are in excellent agreement with Eq. (3) as visible in Fig. 4a, which also allows to extract information about the proportion of the switched area x . In addition, the intermediate switched states were analyzed with Eq. (1)

to acquire the different values of angle φ . The plot between x and φ is shown in Fig. 4b and demonstrates the sensitivity of the BPV response to smallest changes in the orientation of P_{net} . Hence we can propose that the angle φ can be effectively utilized as a probing parameter for P_{net} . Assuming an ideal alignment of P_{net} in the initial state, the angle φ can vary from 0° to $\pm 90^\circ$ irrespective of the PV current magnitudes. The sign associated with φ explicitly is related to the direction of P_{net} in reference to the electrodes, while the absolute value indicates the extent of the switching and the connected tilt angle of P_{net} . This is also analogous to the phase of the locked-in signal measured in PFM which undergoes a $\sim 180^\circ$ phase shift as domains with opposite polarization are scanned. An analogous description of the switching progress in the PPP configuration is shown in Supplementary Fig. S6.

Discussion

With the above results in perspective, we are now in a position to draw some comparisons with the present state of knowledge and discuss some applicability issues. Earlier studies have demonstrated a switchable PV effect in BFO films in capacitor or out-of-plane geometries^{6,22}. However, the origin of the PV effect in such scenarios has been found to be susceptible to the ferroelectric-electrode interface, and also to the overall conduction of the gap¹. As a result, I_{sc} can be merely utilized to determine the direction of polarization.

The planar geometries used in this work allowed us to focus on the I_{sc} originating from the BPV effect, which is evident from the angular-dependent characteristics. Similar planar geometries have been used in the past for studying photo-related processes in BFO films^{15,23–28}. However, the use of either white light or light with fixed plane of polarization restricted the studies to switching of ferroelectricity and observation of switchable PV effect^{23–26}. Likewise the vertical or capacitor geometries, even in planar configuration high electric fields can result in other effects as well, such as migration of oxygen vacancies and accumulation of charges at the electrode-ferroelectric interface²⁴. In addition, domain walls separating head-to-head domains can be created which have been demonstrated to show sub-band gap photoresponse^{25,26}. But large sized gaps and above band-gap illumination (necessary for BPV effect) allowed us to circumvent such secondary contributions and focus only on the bulk photoresponse. This is also evident from I_{sc} and V_{oc} measurements which always exhibited an angular dependency on light polarization, i.e. in pristine, semi- and completely switched states.

Our analysis of I_{sc} , in conjunction with the domain arrangement, provided an insight into the evolution of the BPV effect. The responses were compared with previously calculated relations, which manifested the extraction of crucial coefficients. Henceforth, a model was proposed which can be utilized for estimating not only the orientation and magnitude of P_{net} , but also the proportion of switched regions. The measured areas are much larger than the areas that can be typically accommodated in a single image scan of a probe-based technique. These results therefore unravel the potential of the BPV phenomenon, typically perceived as an outcome of domain and polarization configuration, as a means of detection. The simplicity of the method presented in this work can be much appreciated upon comparison with the well-established SHG technique. In addition, the possibility to estimate the proportion of switched/un-switched region is yet to be demonstrated with SHG based methods.

However, one of the main drawbacks of this method is the necessity of the ferroelectric to exhibit BPV characteristics. But, as per rules of symmetry, all ferroelectric materials are capable of such an effect. For instance, anomalous photoresponse has been reported and studied in LiNbO₃²⁹, KNbO₃¹⁶, BaTiO₃³⁰ and PbTiO₃³¹. Therefore, further calibrations will certainly strengthen the framework presented here for the determination of polarization related parameters in a variety of ferroelectric materials.

Methods

Thin film growth. The BiFeO₃ thin films were grown on single crystalline SrTiO₃ and DyScO₃ substrates using a pulsed laser deposition system (SURFACE PLD-Workstation). During deposition, the substrate was kept at 625 °C and exposed to an oxygen partial pressure of 0.145 mbar. The KrF excimer laser was set to an energy density of $\sim 1.45 \text{ J cm}^{-2}$ with a pulse frequency of 2 Hz.

Electrode deposition. The electrodes were structured using a standard photolithography process. DC sputtering was used to deposit the electrode material (Pt:Pd, 80:20) with a thickness of $\sim 70 \text{ nm}$.

Piezoresponse force microscopy. PFM images were acquired with a Park NX10 system combined with an external lock in amplifier (Zurich Instruments). The AC voltage (3 V, 20 kHz) was applied through a cantilever equipped with a platinum coated tip (MikroMasch NSC 14).

Photoelectrical measurements. A high impedance electrometer (Keithley 6517B) acted as a voltage source (IV-characteristics, switching voltage) and simultaneously measured the current. The samples were illuminated by a diode laser (Cobolt 06 MLD) with a wavelength of 405 nm and 100 mW power.

Switching experiments. During the switching process the maximum applied voltage was increased in 50 V steps. The voltage was ramped up from zero to the maximum voltage of the switching step with a rate of 5 V s^{-1} . IV characteristics were acquired after each switching step for a fixed angle θ . PFM measurement and θ -dependent PE measurements were performed after certain switching steps.

References

- Pintilie, L., Vrejoiu, I., Rhun, G. L. & Alexe, M. Short-circuit photocurrent in epitaxial lead zirconate-titanate thin films. *Journal of Applied Physics* **101**, 064109, <https://doi.org/10.1063/1.2560217> (2007).
- Pintilie, L., Dragoi, C. & Pintilie, I. Interface controlled photovoltaic effect in epitaxial Pb(Zr, Ti)O₃ films with tetragonal structure. *Journal of Applied Physics* **110**, 044105, <https://doi.org/10.1063/1.3624738> (2011).
- Basu, S. R. *et al.* Photoconductivity in BiFeO₃ thin films. *Applied Physics Letters* **92**, 091905, <https://doi.org/10.1063/1.2887908> (2008).

4. Choi, T., Lee, S., Choi, Y. J., Kiryukhin, V. & Cheong, S.-W. Switchable ferroelectric diode and photovoltaic effect in BiFeO₃. *Science* **324**, 63–66, <https://doi.org/10.1126/science.1168636> (2009).
5. Lee, D. *et al.* Polarity control of carrier injection at ferroelectric/metal interfaces for electrically switchable diode and photovoltaic effects. *Physical Review B* **84**, <https://doi.org/10.1103/physrevb.84.125305> (2011).
6. Yi, H. T., Choi, T., Choi, S. G., Oh, Y. S. & Cheong, S.-W. Mechanism of the switchable photovoltaic effect in ferroelectric BiFeO₃. *Advanced Materials* **23**, 3403–3407, <https://doi.org/10.1002/adma.201100805> (2011).
7. Guo, R. *et al.* Non-volatile memory based on the ferroelectric photovoltaic effect. *Nature Communications* **4**, <https://doi.org/10.1038/ncomms2990> (2013).
8. Heron, J. T. *et al.* Electric-field-induced magnetization reversal in a ferromagnet-multiferroic heterostructure. *Physical Review Letters* **107**, <https://doi.org/10.1103/physrevlett.107.217202> (2011).
9. You, L. *et al.* Uniaxial magnetic anisotropy in La_{0.7}Sr_{0.3}MnO₃ thin films induced by multiferroic BiFeO₃ with striped ferroelectric domains. *Advanced Materials* **22**, 4964–4968, <https://doi.org/10.1002/adma.201001990> (2010).
10. Chu, Y.-H. *et al.* Electric-field control of local ferromagnetism using a magnetoelectric multiferroic. *Nature Materials* **7**, 478–482, <https://doi.org/10.1038/nmat2184> (2008).
11. Wang, L. *et al.* Ferroelectrically tunable magnetic skyrmions in ultrathin oxide heterostructures. *Nature Materials* **17**, 1087–1094, <https://doi.org/10.1038/s41563-018-0204-4> (2018).
12. Trassin, M., Luca, G. D., Manz, S. & Fiebig, M. Probing ferroelectric domain engineering in BiFeO₃ thin films by second harmonic generation. *Advanced Materials* **27**, 4871–4876, <https://doi.org/10.1002/adma.201501636> (2015).
13. Denev, S. A., Lummen, T. T. A., Barnes, E., Kumar, A. & Gopalan, V. Probing ferroelectrics using optical second harmonic generation. *Journal of the American Ceramic Society* **94**, 2699–2727, <https://doi.org/10.1111/j.1551-2916.2011.04740.x> (2011).
14. Sturman, B. I. & Fridkin, V. M. *The Photovoltaic and Photorefractive Effects in Noncentrosymmetric Materials* (Gordon and Breach Science Publishers, 1992).
15. Nakashima, S., Hayashimoto, R., Fujisawa, H. & Shimizu, M. Bulk photovoltaic effects in mn-doped BiFeO₃ thin films and the optical strains. *Japanese Journal of Applied Physics* **57**, 11UF11, <https://doi.org/10.7567/jjap.57.11uf11> (2018).
16. Avakyan, E. M., Belabaev, K. G., Odulov, S. G. & Oleinik, O. I. Photogalvanic currents in reduced lithium tantalum crystals. *Izvestiya Akademii Nauk, SSSR Seriya Fizicheskaya* **47**, 656–659 (1983).
17. Bhatnagar, A., Chaudhuri, A. R., Kim, Y. H., Hesse, D. & Alexe, M. Role of domain walls in the abnormal photovoltaic effect in BiFeO₃. *Nature Communications* **4**, <https://doi.org/10.1038/ncomms3835> (2013).
18. Solmaz, A. *et al.* Domain selectivity in BiFeO₃ thin films by modified substrate termination. *Advanced Functional Materials* **26**, 2882–2889, <https://doi.org/10.1002/adfm.201505065> (2016).
19. Yun, Y., Ramakrishnegowda, N., Park, D.-S. & Bhatnagar, A. Long range ordering of 71° domain walls in epitaxial BiFeO₃ thin films. *Applied Physics Letters* **113**, 042901, <https://doi.org/10.1063/1.5037512> (2018).
20. Yu, P. *et al.* Interface control of bulk ferroelectric polarization. *Proceedings of the National Academy of Sciences* **109**, 9710–9715, <https://doi.org/10.1073/pnas.1117990109> (2012).
21. Balke, N. *et al.* Direct observation of capacitor switching using planar electrodes. *Advanced Functional Materials* **20**, 3466–3475, <https://doi.org/10.1002/adfm.201000475> (2010).
22. Ji, W., Yao, K. & Liang, Y. C. Bulk photovoltaic effect at visible wavelength in epitaxial ferroelectric BiFeO₃ thin films. *Advanced Materials* **22**, 1763–1766, <https://doi.org/10.1002/adma.200902985> (2010).
23. Yang, S. Y. *et al.* Above-bandgap voltages from ferroelectric photovoltaic devices. *Nature Nanotechnology* **5**, 143–147, <https://doi.org/10.1038/nnano.2009.451> (2010).
24. Moubah, R. *et al.* Photoelectric effects in single domain BiFeO₃ crystals. *Advanced Functional Materials* **22**, 4814–4818, <https://doi.org/10.1002/adfm.201201150> (2012).
25. Lee, W.-M. *et al.* Spatially resolved photodetection in leaky ferroelectric BiFeO₃. *Advanced Materials* **24**, OP49–OP53, <https://doi.org/10.1002/adma.201102816> (2012).
26. Sung, J. H. *et al.* Single ferroelectric-domain photovoltaic switch based on lateral BiFeO₃ cells. *NPG Asia Materials* **5**, e38–e38, <https://doi.org/10.1038/am.2013.1> (2013).
27. Gao, R. *et al.* Ferroelectric photovoltaic effect. In *Ferroelectrics and Their Applications*, <https://doi.org/10.5772/intechopen.78238> (InTech, 2018).
28. Yang, M.-M., Luo, Z.-D., Kim, D. J. & Alexe, M. Bulk photovoltaic effect in monodomain BiFeO₃ thin films. *Applied Physics Letters* **110**, 183902, <https://doi.org/10.1063/1.4983032> (2017).
29. Fridkin, V. M. & Magomadov, R. M. Anomalous photovoltaic effect in LiNbO₃:Fe in polarized light. *JETP Letters* **30**, 686–688 (1979).
30. Koch, W. T. H., Munser, R., Ruppel, W. & Würfel, P. Anomalous photovoltage in BaTiO₃. *Ferroelectrics* **13**, 305–307, <https://doi.org/10.1080/00150197608236596> (1976).
31. Fridkin, V. M., Popov, B. N., Kuznetsov, V. A. & Barsukova, M. L. The photoconductivity and photovoltaic effect in PbTiO₃. *Ferroelectrics* **19**, 109–110, <https://doi.org/10.1080/00150197808237837> (1978).

Acknowledgements

The authors thank Professor Kathrin Dörr and Dr. Diana Rata for the X-ray measurements, Marian Lisca for the technical support, Dr. Bodo Fuhrmann and Dipl.-Phys. Sven Schlenker for their support with the facilities at the Interdisziplinäre Zentrum für Materialwissenschaften (IZM), and Professor Dietrich Hesse for carefully reading this manuscript. Financial support from Bundesministerium für Bildung und Forschung (BMBF) Project No. 03Z22HN12, Deutsche Forschungsgemeinschaft (DFG) within Sonderforschungsbereiche (SFB) 762 (project A12), and Europäischen Fonds für regionale Entwicklung (EFRE) Sachsen-Anhalt is gratefully acknowledged.

Author Contributions

A.B. and D.S.K. designed and conceived the experiments. D.S.K. was responsible for thin film growth, PFM analysis and photoelectric measurements. Y.Y., N.R., L.M. and X.L. participated in thin film growth and structural characterization. A.B. and D.S.K. co-wrote the manuscript with inputs from all the co-authors.

Additional Information

Supplementary information accompanies this paper at <https://doi.org/10.1038/s41598-019-50185-1>.

Competing Interests: The authors declare no competing interests.

Publisher's note Springer Nature remains neutral with regard to jurisdictional claims in published maps and institutional affiliations.

www.nature.com/scientificreports/



Open Access This article is licensed under a Creative Commons Attribution 4.0 International License, which permits use, sharing, adaptation, distribution and reproduction in any medium or format, as long as you give appropriate credit to the original author(s) and the source, provide a link to the Creative Commons license, and indicate if changes were made. The images or other third party material in this article are included in the article's Creative Commons license, unless indicated otherwise in a credit line to the material. If material is not included in the article's Creative Commons license and your intended use is not permitted by statutory regulation or exceeds the permitted use, you will need to obtain permission directly from the copyright holder. To view a copy of this license, visit <http://creativecommons.org/licenses/by/4.0/>.

© The Author(s) 2019

4.S Supplementary Information

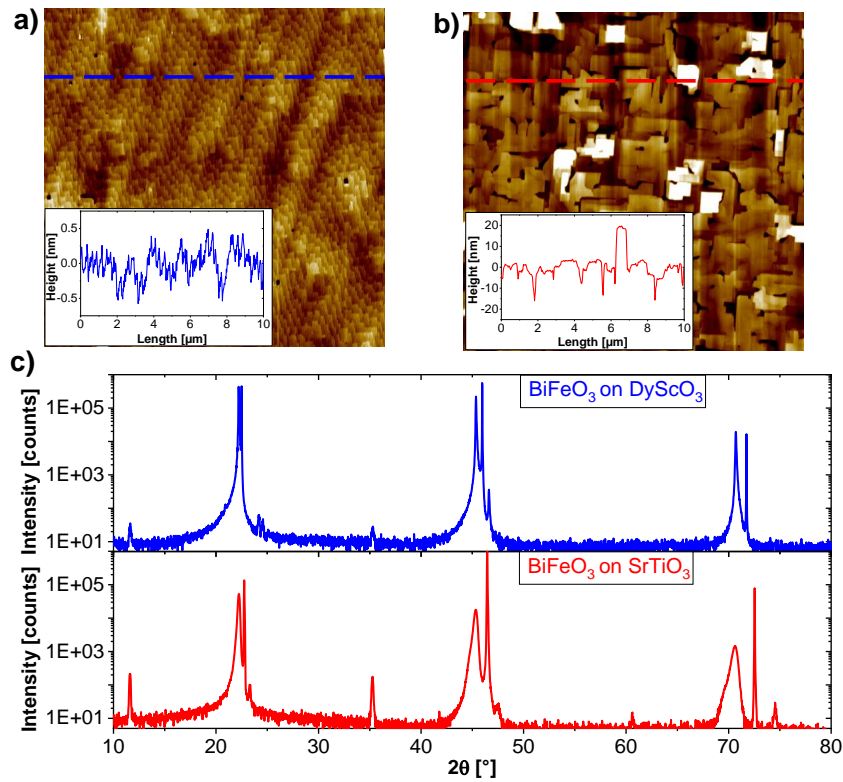


Figure 4.S1: Topography scan ($10 \times 10 \mu\text{m}^2$) of (a) BFO/DSO and (b) BFO/STO sample acquired by AFM. The insets show the respective line profile along the dotted line. (c) X-ray diffraction $2\theta/\omega$ -scan of both samples.

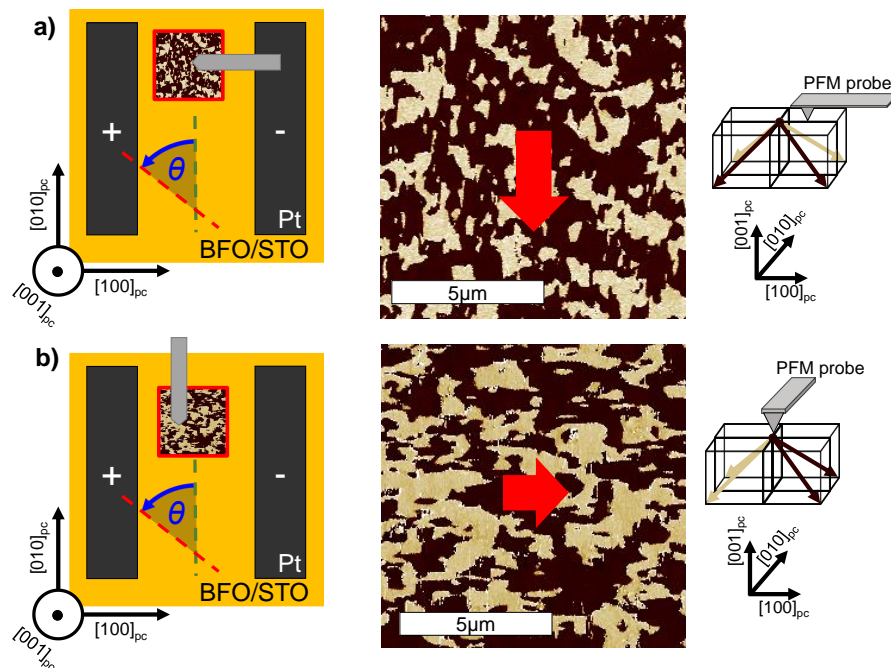


Figure 4.S2: LPFM phase images of the BFO/STO when PFM probe was aligned along (a) [100]_{pc} and (b) [010]_{pc}, respectively, reveal different dark-to-bright ratios.

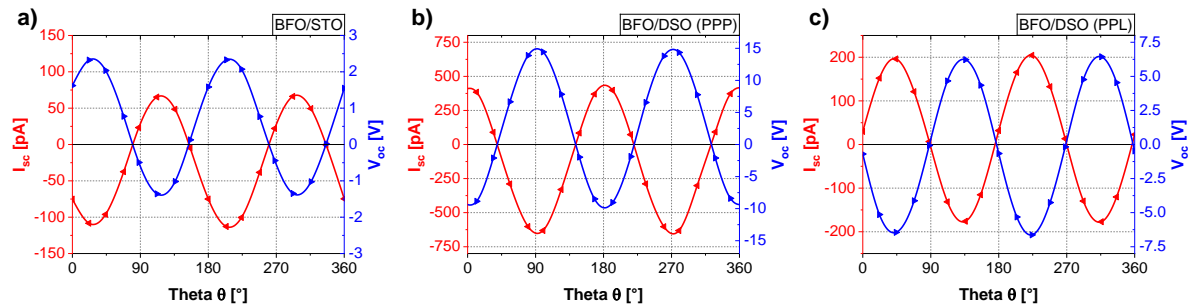


Figure 4.S3: I_{sc} and V_{oc} as a function of θ in the initial state of (a) BFO/STO, (b) BFO/DSO PPP configuration and (c) BFO/DSO PPL configuration.

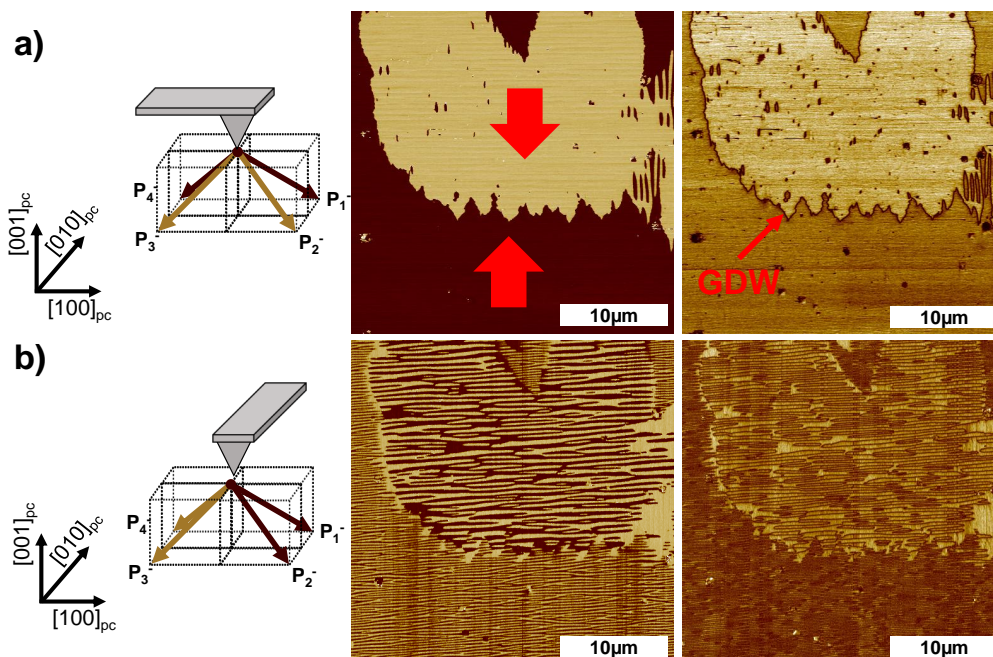


Figure 4.S4: LPFM phase and amplitude images of the intermediate switching state, when cantilever was aligned along a) $[100]_{pc}$ and b) $[010]_{pc}$, respectively. The global domain wall (GDW) separates switched and unswitched regions with opposite direction of P_{net} .

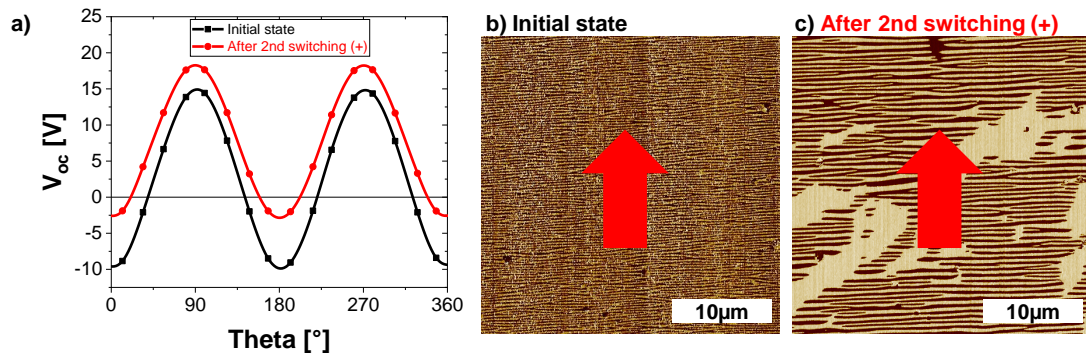


Figure 4.S5: a) V_{oc} as function of θ of the initial state and after the second switching. The maximum value increased from ~ 15 V to ~ 18 V. The corresponding LPMF phase images show an increased domain width (c) after the 2nd switching compared to (b) the initial state.

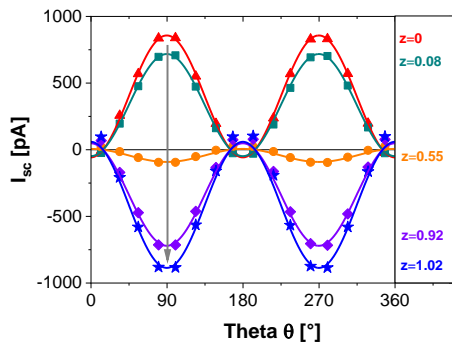
Additional Information FIG. 4 - Derivation of Fitting Function

Equation 1 = Equation 3 (Main text)

$$\Leftrightarrow A + B \sin(2\theta + \varphi) = (1 - x)(A_0 + B_0 \sin(2\theta + \varphi_0)) + x(C_1 + D_1 \cos 2\theta + \chi_1)$$

$$\Rightarrow x(\varphi) = \left[1 + \frac{D_1(\sin(\chi_1) + \cos(\chi_1) \tan(\frac{\pi}{2} - \varphi))}{B_0(\cos(\varphi_0) - \sin(\varphi_0) \tan(\frac{\pi}{2} - \varphi))} \right]^{-1} \quad (4.S1)$$

a) $I_{sc} = (1 - z) \cdot (C_1 + D_1 \cdot \cos(2\theta + \chi_1)) - z \cdot (C_1 + D_1 \cdot \cos(2\theta + \chi_1))$



b) $I_{sc} = C + D \cdot \cos(2\theta + \chi)$

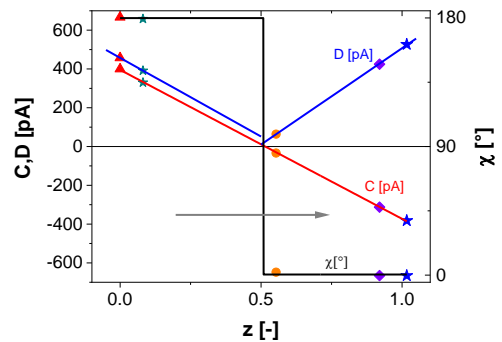


Figure 4.S6: (a) I_{sc} as a function of θ for switching steps of within the second switching cycle (positive electric fields). Parameters z indicates the extent of switching extracted from fitting with the equation shown above the graph. (b) Corresponding values of C , D and χ extracted from fitting with Equation 2 as a function of the extent of switching z .

Summary - CHAPTER 4

Two type of epitaxial BiFeO₃ thin film heterostructures were grown on SrTiO₃ and DyScO₃ substrates using PLD. AFM and XRD measurements were used to confirm high thin film quality and examine the epitaxial relation between film and substrate (Figure 4.S1). The ferroelectric character of the thin films was tested by the use of a detailed PFM analysis. The LPFM measurements of the BiFeO₃//SrTiO₃ heterostructures revealed a random arrangement of patched domains with different in-plane polarization directions. A detailed PFM analysis demonstrated the existence of four out of eight possible domain variants with a slight in-plane net polarization (Figure 4.S2). Large-scale planar top electrodes on the film surface (950 μm length, 40 μm gap distance) enabled the BPV measurement and the application of electric fields. First measurement of the BPV response revealed a dependency of the short-circuit current on the linear light polarization direction. After the application of high electric fields, the BPV response undergoes a phase shift and an offsetting compared to the initial state (Figure 4.1). Due to the tensorial nature of the BPV effect, the direction of the in-plane polarization projection was concluded from a careful analysis of the light-polarization-dependent photovoltaic measurements. To further elucidate the possibility to gain information about the present ferroelectric polarization state, BiFeO₃ films grown on DyScO₃ with a highly-ordered striped ferroelectric domain arrangement were investigated as well. The stripe domain arrangement originates from an anisotropic strain applied by the DyScO₃ substrates. The PFM analysis revealed the existence of only two polarization variants. This alternate arrangement of striped domains leads to a large net in-plane polarization along a specific crystallographic direction. BPV measurements with different electrode orientations (perpendicular and parallel to resulting in-plane net polarization) were in agreement with analytical tensorial calculations. On one hand, the application of electric fields antiparallel to the net in-plane polarization forced a flip of both the polarization and the BPV response (Figure 4.2) The measurements of intermediate states demonstrated the absence of gradual phase shifting during the switching process. This can be explained by the fact that there is no polarization rotation involved. On the other hand, electric fields perpendicular to the net polarization force the ferroelectric polarization to rotate and align parallel to the electric field direction. This rotation of the ferroelectric polarization results in a phase shift of the BPV response (Figure 4.3). The results clearly demonstrated the tensor-nature of the photovoltaic effect in BiFeO₃. Consequently, it was possible to utilize the phase shift of the BPV response to track the polarization rotation and the switching progress (Figure 4.4). Whereas other techniques are restricted to small areas (e.g. PFM) or require the application of electric fields larger than the coercive field for polarization determination (e.g. standard thin film testing devices), the measurements and analysis of the BPV effect can give information about the polarization direction on large read-out areas non-destructively.

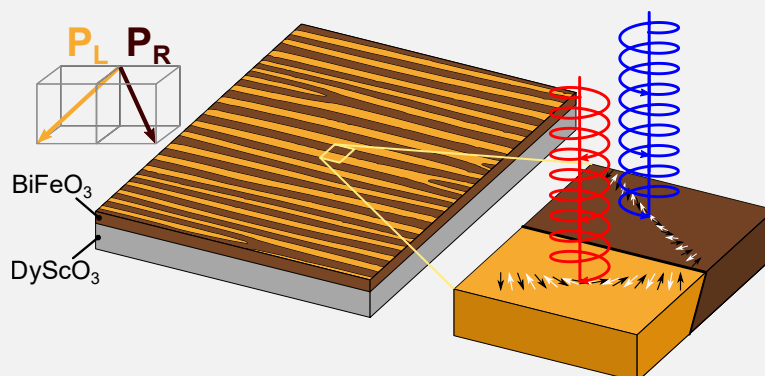
CHAPTER 5

Anomalous Circular Bulk Photovoltaic Effect in BiFeO₃ Thin Films with Stripe-Domain Pattern

In the first part of this thesis, linearly polarized light was utilized to characterize the photovoltaic properties systematically and to demonstrate the direct link between the BPV effect and the ferroelectric polarization direction. Due to the gyrotropic character of BiFeO₃, there are non-zero components of the circular BPV tensor β_{ij}^C (compare Section 2.3). The aim of the second part of this thesis was to investigate, for the first time, the circular (and elliptical) BPV effect in BiFeO₃. For this, the experimental setup was extended to enable the continuous adjustment of the light polarization from linear to elliptical to circular. The experimental findings confirmed the existence of the circular BPV effect in BiFeO₃, however, an anomalous character of the effect was observed and further elucidated.

PUBLISHED AS:

Knoche, David S., Steimecke, M., Yun, Y., Mühlenbein, L. & Bhatnagar, A. "Anomalous circular bulk photovoltaic effect in BiFeO₃ thin films with stripe-domain pattern". *Nature Communications* **12**, 282 (2021)



ToC Figure 5.0: Schematic of striped domain arrangement in BiFeO₃ (left). The detailed investigation of the BiFeO₃ thin films revealed the existence of an anomalous circular bulk photovoltaic effect. Possible reason for this behavior is a domain-specific differential interaction between the different domain variants and circularly-polarized light of different helicity originated from the chiral anti-ferromagnetic spin cycloid (right).




ARTICLE



<https://doi.org/10.1038/s41467-020-20446-z>

OPEN

Anomalous circular bulk photovoltaic effect in BiFeO₃ thin films with stripe-domain pattern

David S. Knoche ^{1,2}, Matthias Steimecke ³, Yeseul Yun^{1,2}, Lutz Mühlenbein^{1,2} & Akash Bhatnagar ^{1,2}✉

Multiferroic bismuth ferrite, BiFeO₃, offers a vast landscape to study the interplay between different ferroic orders. Another aspect which is equally exciting, and yet underutilized, is the possibility of large-scale ordering of domains. Along with symmetry-driven bulk photovoltaic effect, BiFeO₃ presents opportunities to conceptualize novel light-based devices. In this work, we investigate the evolution of the bulk photovoltaic effect in BiFeO₃ thin films with stripe-domain pattern as the polarization of light is modulated from linear to elliptical to circular. The open-circuit voltages under circularly polarized light exceed ± 25 V. The anomalous character of the effect arises from the contradiction with the analytical assessment involving tensorial analysis. The assessment highlights the need for a domain-specific interaction of light which is further analyzed with spatially-resolved Raman measurements. Appropriate positioning of electrodes allows observation of a switch-like photovoltaic effect, i.e., ON and OFF state, by changing the helicity of circularly polarized light.

¹Zentrum für Innovationskompetenz SiLi-nano, Martin-Luther-Universität Halle-Wittenberg, Halle (Saale) 06120, Germany. ²Institut für Physik, Martin-Luther-Universität Halle-Wittenberg, Halle (Saale) 06120, Germany. ³Institut für Chemie, Technische Chemie, Martin-Luther-Universität Halle-Wittenberg, Halle (Saale) 06120, Germany. ✉email: akash.bhatnagar@physik.uni-halle.de

The re-discovery photovoltaic effect in ferroelectrics has far reaching implications that have been till now demonstrated. The obvious ones include the realization of junction free-photovoltaic modules¹, and tracing polarization components, both in-plane² and out-of-plane³, via non-destructive methodologies. Generation of above bandgap open-circuit voltage (V_{oc}) under suitable illumination is another outcome which has garnered immense attention^{1,4}. The underlying symmetry-driven charge-separation mechanism is even more enticing which has fueled research for materials with broken inversion symmetry. Conversely, the effect itself has been also utilized to detect the status of inversion symmetry in a wide range of materials such as oxides⁵, topological insulators⁶, and inorganic-organic perovskites^{7,8}. In this context, the circular bulk photovoltaic effect (CBPV) is of particular interest. In general, the photovoltaic effect in materials without inversion symmetry can be resolved into two parts, linear and circular⁵. Much of the work till now has been focused on the linear bulk photovoltaic effect (LBPV) wherein the resulting photovoltaic current depends on the orientation of the linearly polarized (LP) light⁵.

The CBPV, on the other hand, results in a photocurrent which depends on the helicity of the CP light^{9–12}. An essential prerequisite for the manifestation of such an intriguing phenomenon, apart from the absence of inversion symmetry, is a split in the conduction or valence band of the material in reciprocal space, which is also known as Rashba and Dresselhaus effect^{9,11,13}. As a result, light of a given helicity excites charges with spin up \uparrow , while of opposite helicity charges of spin down \downarrow . Consequently, the CBPV has been often utilized as probing methodology to detect Rashba splitting in different bulk material systems such as BiTeBr¹⁴ and ZnO¹⁵, and even in heterostructures comprising of AlGaIn-GaN¹⁶. In addition, measurements of the CBPV have been instrumental in confirming the absence of inversion symmetry in different organic-inorganic perovskite-structured systems, which has assisted in the pursuit of finding the origin of charge separation mechanisms in these materials system¹⁷.

Therefore, it is rather intriguing that the CBPV has never been investigated in BiFeO₃, although all the essential criteria are evidently satisfied. The rhombohedral polar space group R3c of bulk BiFeO₃ leads to ferroelectricity¹⁸ and the existence of the LBPV. The crystal symmetry also allows gyrotropy and thus the CBPV should be observable in BiFeO₃⁵. This becomes more interesting with BiFeO₃ having a bandgap ($E_g \approx 2.7\text{eV}$)¹⁹ which lies within the visible range of solar spectrum and a corresponding photovoltaic effect that has been shown to be governed by the symmetry.

The ferroelectric domain arrangement can be engineered in a periodic array by tuning growth conditions, such as substrate symmetry²⁰ and termination²¹, gas pressure, and related composition²². The room temperature multiferroic character of BiFeO₃ manifests in a rather intricate coupling between the polarization vector and magnetic order²³. Consequently, the control of the magnetic order by the application of electric fields has been predicted and demonstrated successfully in thin film-based devices. Furthermore, the magnetic order in BiFeO₃ is currently under intense investigation which exhibits a non-collinear antiferromagnetic spin cycloidal structure and is a potential candidate for future antiferromagnetic spintronic devices²⁴. An in-depth view of the magnetic order was recently provided that explicitly illustrated the existence of spin cycloids within each domain having a propagation vector aligned orthogonal to the polarization²⁵. Consequently, the periodic ferroelectric domain pattern essentially renders an equally ordered magnetic texture of BiFeO₃ thin films grown on a variety of different substrates²⁶. This evidently presents some interesting opportunities to analyze domain-specific light-matter interactions, inherent to materials which have chiral textures²⁷. Therefore, it becomes apparent that BiFeO₃ thin films provide a lucrative landscape to study the overlap of these rather discrete aspects.

In this work, we investigate the CBPV in epitaxially grown BiFeO₃ thin films. The LBPV is first utilized to establish the photovoltaic activity of the samples with V_{oc} well above the bandgap. The BPV is investigated systematically by modulating the polarization of the light from linear to circular. A changed CP light helicity (left \leftrightarrow right) generates V_{oc} of opposite polarities, albeit with nearly half of the magnitude in comparison to the maximum response under LP light. Analysis of the response with the CBPV tensor suggests a rather compelling scenario involving domain-specific interaction of the CP light. This aspect is tested with different measurement geometries which results in a switch-like state exhibiting a chirality-dependent ON and OFF state of the photovoltaic effect. Spatially-resolved Raman measurements, and related analysis, further bolster the arguments.

Results

Thin-film growth and characterization. BiFeO₃ thin films with a thickness of around 200 nm were deposited on single-crystalline DyScO₃ (110)_{orth} substrates using a pulsed laser deposition system. Further details on sample growth can be found in the Methods sections. The topography of the resultant samples appears to be smooth (root-mean-square roughness $R_q \approx 850\text{pm}$) with stripes along $[100]_{pc}$ as shown in Fig. 1a. The lateral signal, phase (Fig. 1b), and amplitude, acquired from piezo force

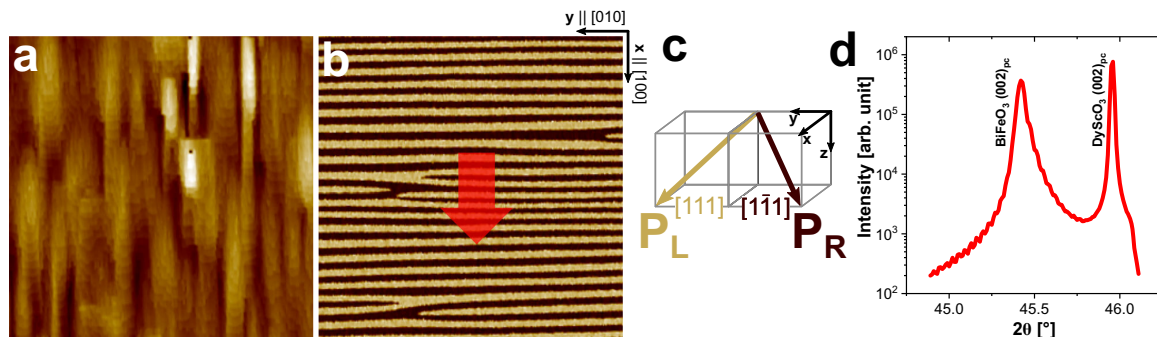


Fig. 1 Domain and structural characterization of BiFeO₃ thin film. **a** Surface morphology visualized using atomic force microscopy ($R_q \approx 850\text{pm}$) and **b** corresponding in-plane PFM phase image (cantilever aligned along $[100]_{pc}$, $7.5 \times 7.5\ \mu\text{m}^2$). Red arrow indicates the in-plane net polarization resulting from the stripe-ordered domain arrangement of only two polarization variant P_L and P_R shown schematically in **c**. **d** X-Ray diffraction $2\theta - \omega$ scan around $(002)_{pc}$ substrate peak.

microscopy (PFM) reveal a periodic domain pattern and the domains stretch across the entire width of the scan (7.5 μm) on many instances. The striped domain arrangement reveals an average period length around 170 nm in $[100]_{\text{pc}}$. As the vertical signal from PFM was largely consistent in color (Supplementary Fig. 1), the existence of only two variants, out of the eight possible, which are separated by 71° domain walls can be implied. This periodic arrangement of stripe domains lead to a resulting net polarization in $[101]_{\text{pc}}$. The crystallinity and phase purity of the samples were confirmed by X-ray analysis and a $2\theta - \omega$ scan around the $[002]_{\text{pc}}$ substrate peak is presented in Fig. 1d. Because of the mismatch between the lattice parameter of the film $a_{\text{BiFeO}_3, \text{pc}} = 3.965 \text{ \AA}$ ¹⁸ and the substrate $a_{\text{DyScO}_3, \text{pc}} = 3.946 \text{ \AA}$, $b_{\text{DyScO}_3, \text{pc}} = 3.952 \text{ \AA}$ ²⁸ an anisotropic compressive strain is implied during the epitaxial thin film growth. The respective mismatch between the in-plane lattice constant of -0.33% and -0.48% leads to a resultant increased out-of-plane lattice constant of BiFeO₃ $c_{\text{BiFeO}_3, \text{pc}} = 3.991 \text{ \AA}$. The value is in agreement with other studies wherein, similar c and strain were observed due to the largely identical in-plane lattice constants of the BiFeO₃ film and DyScO₃ substrates^{20,26}.

Bulk photovoltaic effect. The samples were first measured with LP light with a wavelength of 405 nm (3.06 eV). In Fig. 2a, the measurement geometry is schematically depicted with electrodes running along x-direction perpendicular to the domain walls. The generated photovoltaic current (density) j_i^L for an ordered striped domain arrangement with 71° domain walls can be described with following equation (Details: Supplementary Fig. 2/Eqs. (1)–(15)):

$$j_i^L = I \begin{pmatrix} \left(\frac{\beta_{33}^L}{3\sqrt{3}} + \frac{2\beta_{31}^L}{3\sqrt{3}} + \frac{\beta_{22}^L}{3\sqrt{6}} + \frac{\beta_{15}^L}{6\sqrt{3}} \right) + \left(\frac{\beta_{22}^L}{\sqrt{6}} + \frac{\beta_{15}^L}{2\sqrt{3}} \right) \cos(2\theta) \\ \left(\frac{\beta_{33}^L}{3\sqrt{3}} - \frac{\beta_{31}^L}{3\sqrt{3}} - \frac{2\beta_{22}^L}{3\sqrt{6}} + \frac{\beta_{15}^L}{6\sqrt{3}} \right) \sin(2\theta) \\ \left(\frac{2\beta_{22}^L}{3\sqrt{6}} + \frac{\beta_{15}^L}{3\sqrt{3}} - \frac{\beta_{33}^L}{3\sqrt{3}} - \frac{2\beta_{31}^L}{3\sqrt{3}} \right) \end{pmatrix} \quad (1)$$

wherein I is the light intensity, β_{ij}^L are the LBPV coefficients, and θ is the angle describing the rotation of the electric field plane of the LP light around the z-axis. The rotation is achieved by using a half-wave ($\frac{\lambda}{2}$) plate.

The measured values of the photovoltaic current (density) in y-direction are largely similar to the previously reported values^{1,2}. The dependency on the light orientation θ match qualitatively the predicted sinusoidal response in Eq. (1) and confirms the dominance of the BPV. In addition, the photovoltaic effect was found to be switchable in its characteristics as electric fields above the coercive field were applied across the electrodes. The resultant response largely mimics ferroelectric switching which further validates the dominance of ferroelectric/bulk photovoltaic effect in these samples (Supplementary Fig. 3). It must be emphasized here that the magnitude of photovoltaic current scales up linearly with the intensity of light. On the contrary, the V_{oc} should remain constant above a threshold light intensity²⁹. We also tested this condition by gradually scaling up the light intensity and observed a distinct saturation of V_{oc} above a certain intensity of light. Furthermore, the current-voltage characteristics are linear with an unchanged slope for different light orientation θ (Supplementary Fig. 4/5) Therefore, both j_i and V_{oc} can be used to describe the observed photovoltaic effect, however, because of the insensitivity towards slight light intensity changes, from hereon, only the extracted values of V_{oc} will be presented.

The photovoltaic current (density) originating from the CBPV j_i^C depends on the helicity of the CP light (Details: Supplementary Eqs. (16)–(23)):

$$\text{LCP : } j_i^{\text{LCP}} = \frac{I}{\sqrt{3}} \begin{pmatrix} 0 \\ +\beta_{12}^C \\ 0 \end{pmatrix} \quad (2a)$$

$$\text{RCP : } j_i^{\text{RCP}} = \frac{I}{\sqrt{3}} \begin{pmatrix} 0 \\ -\beta_{12}^C \\ 0 \end{pmatrix} \quad (2b)$$

wherein j_i^{LCP} and j_i^{RCP} are the generated CBPV current density under illumination with left-handed circularly polarized (LCP) and right-handed circularly polarized (RCP) light, respectively. For both light chiralities, the current depends on the light intensity I and the CBPV coefficient β_{12}^C . The current in x- and z-direction is zero, whereas in y-direction reverses its direction from LCP to RCP light.

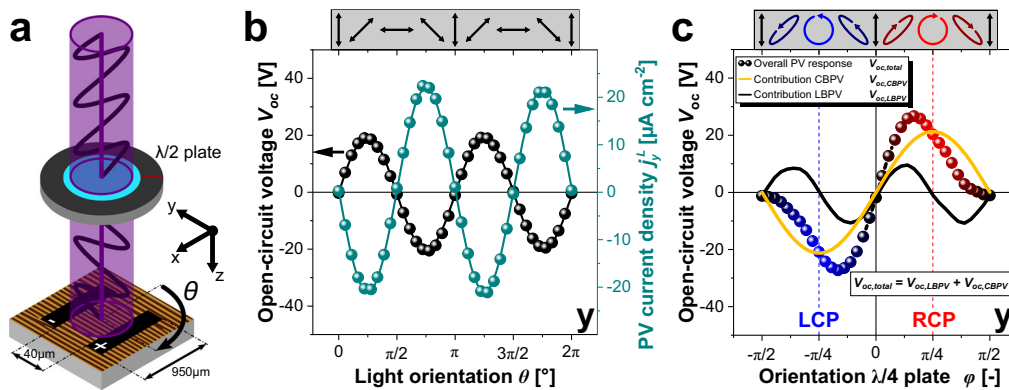


Fig. 2 Photoelectrical measurements revealing LBPV and CBPV in BiFeO₃ thin films. **a** Schematic of the experimental setup (not to scale): A $\frac{\lambda}{2}$ plate is used to rotate the orientation of the incoming LP light (rotation described by θ). The light propagates in z-direction and the electrodes run along the x-direction to enable photoelectrical measurements in y-direction. **b** LBPV measurement: V_{oc} and j_y^L as a function of the light orientation θ . The two-sided arrows indicate the orientation of LP light. **c** CBPV measurement: $\frac{\lambda}{4}$ plate placed before $\frac{\lambda}{2}$ plate to enable modification of the light polarization state. The flip of the light helicity due to the presence of the $\frac{\lambda}{2}$ plate is considered in the experimental data. V_{oc} as a function of the $\frac{\lambda}{4}$ plate orientation ϕ . The light polarization varies from linear ($\phi \in \{\pm\frac{\pi}{2}, 0\}$), to elliptical ($\phi \in \{\pm\frac{\pi}{4}, \pm\frac{3\pi}{4}, 0\}$) and to circular ($\phi \in \{\pm\frac{\pi}{2}\}$). The helicity of the light polarization changes from left-handed ($-\frac{\pi}{2} < \phi < 0$) (blue) to right-handed ($0 < \phi < \frac{\pi}{2}$) (red). The overall V_{oc} can be divided into the contribution from the CBPV (yellow solid line) and the LBPV (black solid line).

A quarter-wave ($\frac{1}{4}$) plate was used to change the light polarization. The angle between the the fast axis of the $\frac{1}{4}$ plate and the polarization plane of incident LP light is defined as ϕ . A variation in ϕ apparently modulates the circularity of the light following $P_c = \sin(2\phi)$. As ϕ is varied, the light polarization gradually changes from linear to elliptical, and eventually to circular at $\phi = \pm\frac{\pi}{4}$. The V_{oc} as a function of ϕ is presented in Fig. 2c. The corresponding light polarization is shown in the schematic above. The V_{oc} peaks at $\phi = \pm\frac{\pi}{6}$ with a corresponding magnitude of $\pm 27V$, which is in the regime of elliptical light polarization. The elliptical polarization can be considered as a sum of linear and circular polarization, and consequently, the net measured response is a sum of contributions from LBPV and CBPV. The CBPV response scales up linearly with P_c , which makes it possible to extract the respective contribution (yellow solid line, $V_{oc,CBPV}(\phi) = 21.3V \sin(2\phi)$) from the overall response. The LBPV contribution (black solid line) can be obtained by subtracting the CBPV contribution from the overall response. This was confirmed by an additional measurement conducted with the outgoing light polarization rotated by 90°. The extracted LBPV contribution is shifted while the CBPV contribution remains unchanged (Supplementary Fig. 6).

Similar responses have been also reported in Tellurium^{9,11}, in BiTeBr¹⁴, and more recently in organic-inorganic halide perovskites⁸. In all of these materials systems, the extreme values appear at $\phi = \pm\frac{\pi}{4}$ corresponding to LCP and RCP light. This can be attributed to spin splitting and the excitation of carriers either in $k_x > 0$ or $k_x < 0$ by LCP and RCP light, respectively. The eventual relaxation of the carrier to the corresponding bottom and top of conduction and valence band, respectively, results in photocurrent of opposite direction under illumination with RCP and LCP light, respectively^{8,30}. However, this not the case in our measurements wherein the maximum response appears at $\phi = \pm\frac{\pi}{6}$ because of the superimposed contribution from the LBPV.

Linear to circular bulk photovoltaic effect. In order to distinctly differentiate between the responses arising from LBPV and CBPV, we modified the setup by replacing the $\frac{1}{4}$ plate with a Berek compensator (tunable wave plate). This allowed us to obtain light polarization with different ellipticity ratios ϵ ranging from $\epsilon \approx 1$

(CP light) to $\epsilon > 300$ (LP light) without rotating the main axis of the light polarization ellipse ($\parallel [001]_{pc}$, see Fig. 3d). Details about the light polarization characterization can be found in Supplementary Fig. 7. A subsequent $\frac{1}{2}$ plate enabled the clockwise rotation of the out-coming light by an angle θ (compare Fig. 2b).

In the first instance, identical geometry as depicted in Fig. 2 was used (electrodes \parallel x-direction). Fig. 3b shows the V_{oc} as a function of θ for light with different ϵ . The LP light ($\epsilon > 300$) generates an expected sinusoidal response with maximum $V_{oc} = \pm 19.2V$ (Compare Fig. 2b, Eq. (1)). Interestingly, the right-handed elliptically polarized (EP) light (with $\epsilon = 3$, $\epsilon = 10$) results in higher maxima of around 27.6V (Compare Fig. 2c), and the response is visibly less dependent on θ . As ϵ is further reduced to 1, the angle θ is rendered redundant and a consistent V_{oc} of 20.6 V is observed. Conversely, this also signifies the precession of the CP light. As the helicity of light is changed from right to left, the response of generated V_{oc} follows a similar trend, but with negative polarity. The results with this setup reveal a more detailed insight into the individual contributions arising from LBPV and CBPV. The results are also in coherence with those shown in Fig. 2c and Eq. (2a). The direction of the V_{oc} arising from the CBPV depends on the helicity of the light polarization.

The same measurements were repeated with a different pair of electrodes which were fabricated to measure the response in x-direction. The LBPV response follows now a cosinusoidal relation, instead of sinusoidal, which agrees with Eq. (1). It exhibits higher V_{oc} maxima of around 54V at $\theta \in \{\frac{\pi}{2}, \frac{3\pi}{2}\}$ (Fig. 3c). Upon illumination with EP light, the maximum V_{oc} values drop but remain alike for opposite helicity, i.e., for left-handed and right-handed EP light. The trend continues for the CP light as the V_{oc} values remain independent of the helicity of the light and are around 20V. This is rather surprising for two reasons. Firstly, the substantial response measured in x-direction completely contradicts Eq. (2b), according to which response to CP light should be zero. And secondly, the response is independent of the light helicity.

To analyze this anomaly, we shift our focus to the individual CBPV responses arising from each of the two domain variants. The responses are summarized in Table 1 comprising Equation (3a)–(3d). Interestingly, the calculated current originating from the CBPV is perpendicular to corresponding polarization vector, i.e., for domain variant P_L with polarization pointing in $[111]_{pc}$, RCP and LCP light leads to a photovoltaic current in $[1\bar{1}0]_{pc}$ and $[\bar{1}10]_{pc}$, respectively.

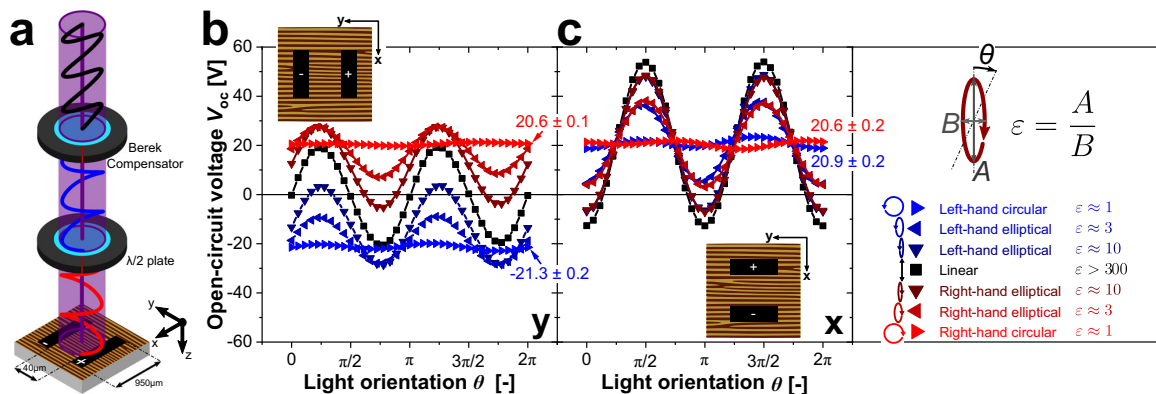


Fig. 3 Deconvolution of the BPV response into linear and circular effects. **a** Schematic of the extended setup (not to scale) comprising a Berek compensator (tunable waveplate) to set arbitrary polarization state of the light ϵ with a subsequent $\frac{1}{2}$ plate to rotate the orientation of the light polarization by θ . V_{oc} as a function of the light polarization orientation θ for different light polarization states measured in **b** y-direction and **c** x-direction. Right- and left-handedness of light is colored red and blue, respectively. The light polarization state as varied from linear ($\epsilon > 300$) over two elliptical ($\epsilon \approx 10$, $\epsilon \approx 3$) to circular ($\epsilon \approx 1$) light polarization.

Also, it is imperative to state that the tensorial assessment is based on a presumption that, both, RCP and LCP light interact equally with domains exhibiting different polarization variants P_L and P_R . However, an alternative situation can be also presumed wherein RCP light interacts with only domains of one explicit domain variant, in this case P_R , while LCP light interacts with domains of the other variant. In this case, the photovoltaic response in y-direction will exhibit opposite polarity under RCP and LCP light, while, will be identical and non-zero in x-direction. This is in complete coherence with the experimental findings.

Analysis of the CBPV and differential light interaction. Based on the analytical assessment, we designed a measurement geometry to focus separately on the CBPV response from each variant under LCP and RCP light. Electrodes were engineered at an angle of $\pm 45^\circ$ with respect to the domain walls. In doing so, the electrodes are aligned parallel to the projection of the polarization vector of P_L or P_R in the xy-plane, while the in-plane projection of the other variant is orthogonal to the electrode. Keeping in perspective the calculated response given in Table 1, the expected V_{oc} arising from variant P_L and P_R are schematically shown in Fig. 4a. For the -45° electrode geometry, the LCP light should provoke a considerable photovoltaic response, whereas with RCP the response should vanish. A reversed

behavior is expected in the $+45^\circ$ electrode geometry. This scenario is confirmed experimentally. It is amply evident that in the -45° configuration depicted in the Fig. 4b only LCP light results in a substantial V_{oc} of 26.0V, while the RCP light induces a V_{oc} of negligible magnitudes ($-0.9V$). In the $+45^\circ$ configuration, instead of LCP, the RCP results in a V_{oc} of 25.0V and LCP induces a minimalistic V_{oc} of $-0.9V$ (Fig. 4c). The experimental findings agree with the scenario derived from the tensorial analysis in Table 1 and schematically demonstrated in Fig. 4a.

The agreement evidently suggests the need of differential interaction between CP light and domain variants. The interaction could be either involving absorption, i.e., circular dichroism (CD), or scattering. We conducted Raman scattering experiments similar to Raman optical activity (ROA) measurements. ROA is a known tool to investigate circular dichroic behavior³¹. Details about the Raman experiments can be found in the Supplementary Discussion and in the Methods section. Spatially-resolved Raman scattering experiment with CP light excitation in combination with principle component analysis (PCA) enabled the visualization of the ferroelectric domain arrangement, which was also confirmed by PFM measurements of the same region on the sample (Supplementary Fig. 8). Because of the usage of CP light, the observed changes in the Raman spectra, unlike other Raman scattering experiments (using LP light excitation)^{32,33}, cannot be explained by a different orientation of the light towards each domain variants. The change must originate from a differential interaction of CP light and the different domain variants and therefore, the Raman experiments further strengthen the presumed domain-specific light interaction.

However, it is imperative to mention that domain-selective light absorption, i.e. CD, cannot be ruled out and is a plausible scenario. As a matter of fact, differential circular dichroic behavior has been reported in poly-domain BiFeO₃ single crystal using (polarized) photo electron emission microscopy (PEEM)³⁴. But the investigation of the dichroic behavior in domains with widths of only a few hundreds of nanometers is challenging because of the limited spatial resolution of typical characterization methods.

Nevertheless, the differential light-domain interactions (absorption or scattering) are an outcome of chirality. In the case of BiFeO₃, the crystal structure itself does not possess any chirality. However, a chiral order linked with the existence of a

Table 1 CBPV contribution from each ferroelectric domain variant.			
	Right-handed circularly polarized light RCP \odot		Left-handed circularly polarized light LCP \ominus
Domain variant P_L	$j_1^{RCP,P_L} = \frac{j_1^c}{2\sqrt{3}} \begin{pmatrix} +1 \\ -1 \\ 0 \end{pmatrix}$ (3a)		$j_1^{LCP,P_L} = \frac{j_1^c}{2\sqrt{3}} \begin{pmatrix} -1 \\ +1 \\ 0 \end{pmatrix}$ (3b)
Domain variant P_R	$j_1^{RCP,P_R} = \frac{j_1^c}{2\sqrt{3}} \begin{pmatrix} -1 \\ -1 \\ 0 \end{pmatrix}$ (3c)		$j_1^{LCP,P_R} = \frac{j_1^c}{2\sqrt{3}} \begin{pmatrix} +1 \\ +1 \\ 0 \end{pmatrix}$ (3d)

Calculated CBPV response for the different domain variants P_L and P_R under illumination with RCP and LCP light, respectively. With respect to presumed the domain-specific light interaction, the CBPV current densities j_1^{RCP,P_L} (Equation 3a) and j_1^{LCP,P_R} (Equation 3d) vanish. The resulting CBPV response consists out of j_1^{LCP,P_L} (Equation 3b) generated in P_L under LCP light illumination and j_1^{RCP,P_R} (Equation 3c) generated in P_R under RCP light illumination. NOTE: Direction of V_{oc} is antiparallel to the direction of j_1 (Compare Fig. 2b).

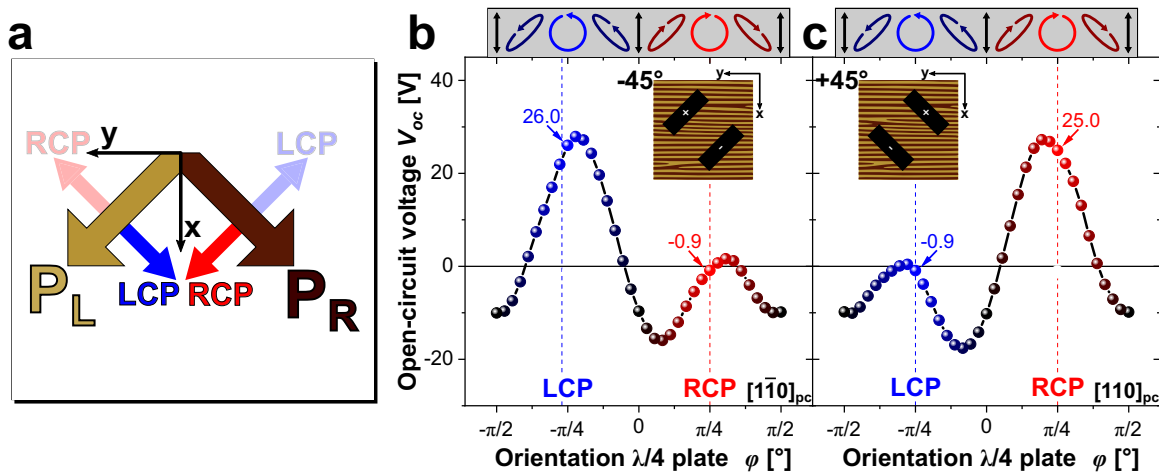


Fig. 4 Electrode alignments to show dominance of LCP over RCP response and vice versa. **a** Direction of V_{oc} based on the proposed scenario above to describe the observed CBPV response (Equation 3b/3c in Table 1). The red and blue arrows implicate the direction of the V_{oc} corresponding to RCP and LCP light, respectively. V_{oc} as a function of $\lambda/4$ plate orientation ϕ measured with electrodes aligned along **b** $[1\bar{1}0]_{pc}$ (-45°), and **c** $[110]_{pc}$ ($+45^\circ$).

cycloidal antiferromagnetic spin texture has been concluded from neutron diffraction measurements in BiFeO₃ ceramics³⁵. This was also confirmed with neutron scattering³⁶ and hard X-ray magnetic scattering measurements³⁷ in single-crystalline BiFeO₃. Very recent studies conducted with nitrogen-vacancy magnetometry, and involving BiFeO₃ thin films, have explicitly revealed the alignment of antiferromagnetic order in the form of cycloid which in simple terms can be perceived as a periodic magnetic object with a chiral character. The spin cycloid propagates within individual and periodically arranged ferroelectric domains in BiFeO₃/DyScO₃ thin films^{25,26,38}. The propagation vector of the cycloid remains perpendicular to the direction of ferroelectric polarization in each domain. Therefore, in a periodic domain pattern, of the kind utilized here, the propagation direction of the spin cycloid sequentially changes from one domain to the other by 90°. Furthermore, the configuration of the cycloid was found to be particularly sensitive to the strain in the film arising from the mismatch between the in-plane lattice parameters of the BiFeO₃ and substrates²⁶. As a result, compressive strain of around 0.35% forces the propagation vector of cycloid to remain in the (111)_{pc} plane, while under tensile strain the vector is restricted to (110)_{pc}^{24,26,39}. From the state of strain and domain arrangement in the BiFeO₃/DyScO₃ thin films analyzed in this study, the existence of spin cycloid can be postulated. Presuming a chirality flip associated with different cycloidal propagation direction, the observed behavior could arise from the differential interaction of CP light with the chiral magnetic texture, as has been also observed with soft resonant elastic X-ray scattering experiments^{26,38}. Interestingly, a recent work has also demonstrated chiral arrangement of electric polarization within 71° domain walls³⁸. Hence it becomes apparent that there are two chiral textures at play within the BiFeO₃/DyScO₃ samples under investigation in this work.

Furthermore, under higher compressive strain, the cycloid breaks and is replaced by G-type antiferromagnetic order^{24,40}. A similar scenario is also encountered in BiFeO₃ films grown directly on SrTiO₃ (001)_{pc} or SrTiO₃ (111)_{pc} wherein the cycloidal order is absent^{40–42}. Curiously, a periodic domain pattern is also missing in such samples which certainly hints towards its necessity for the manifestation of an ordered or harmonic spin cycloid arrangement. Precisely this aspect has been also observed with BiFeO₃ films grown on DyScO₃, albeit with mosaic domain pattern. Mössbauer spectroscopy was implemented to confirm that despite favorable epitaxial strain, a mosaic-like domain pattern is associated with an anharmonic cycloidal order due to significantly higher density of domain walls⁴³. Therefore, it can be postulated that in such mosaic-like domain patterns the domain-specific light interaction, and anomalous CBPV effect, will be also substantially suppressed. We attempted to assess this condition with BiFeO₃ sample grown directly on SrTiO₃ and of similar thickness (Supplementary Fig. 9). The presence of four domain variants culminates in a mosaic-like domain pattern. A distinct LBPV response was measured and the results are in agreement with our previous study. However, the difference between the responses acquired with RCP and LCP light is around 2.5 V which is much less than measured in samples with stripe-like domain pattern (40V in Fig. 2c/3b).

Discussion. In this work we have demonstrated the photovoltaic response in BiFeO₃ under illumination with CP light. The periodic array of domains was critical for the observation of some rather compelling characteristics. Initially, as the polarization of the light was gradually varied from linear to elliptical to circular, the photovoltaic response was found to be notably higher for the elliptical polarization. The overall

response was found to be a sum of contributions arising from linear and circular BPV effect. A modified setup allowed us to separate the resultant photovoltaic effect into its distinct contributions.

Analysis of the CBPV response with the associated tensors explicitly suggests the anomalous character of the BPV effect and the necessity of helicity-dependent interaction of light with domain variants. Recent studies have shown that films with periodic domain arrangement exhibit a magnetic texture formed by the regular arrangement of spin cycloid, orthogonally connected with the polarization vector of each domain. This chiral magnetic texture could be the origin of the differential light–domain interactions. As a matter of fact, analogous principles are also utilized to investigate the profile of the magnetic order and unambiguously differentiate between chiral and non-chiral arrangement³⁷. However, the metallicity of the material itself restricts the usable wavelength to only X-rays in scattering mode. Other modes such as reflection and fluorescence have been also employed based on the insulating character of the material. In this regard, BiFeO₃ presents some apparent advantages. First, the bandgap of BiFeO₃ falls within visible range and a photon energy of 3.06 eV is sufficient for the BPV to arise, providing a direct evidence of light–matter interaction. Second, the periodic arrangement of domains in thin films essentially also assists in achieving a connected chiral antiferromagnetic order. The overlap of these two aspects presents a probable explanation for the observed effects.

Methods

Pulsed laser deposition (PLD) growth. The BiFeO₃ thin films were grown on single-crystalline DyScO₃ (110)_{orth} and SrTiO₃ (001)_c substrates using a pulsed laser deposition system (SURFACE PLD-Workstation). During deposition, the substrate was kept at 625 °C and exposed to an oxygen partial pressure of 0.145 mbar. The distance between the stoichiometric ceramic BiFeO₃ target and the substrate is set to 60 mm. The KrF excimer laser was set to energy densities in the range of 1.2–1.34 J cm⁻² with a pulse frequency of 2Hz.

Piezo-response force microscopy (PFM). PFM images were acquired with a Park NX10 system combined with an external lock-in amplifier (Zurich Instruments). The AC voltage (3 V, 20 kHz) was applied through a cantilever equipped with a platinum-coated tip (MikroMasch NSC 14).

Device fabrication. A conventional photolithography process has been used to structure the rectangular top electrode pairs (950 × 400 μm², 40 μm spacing). A subsequent evaporation with platinum-palladium alloy (Pt:Pd 80:20) with a thickness of ~70 nm were achieved using a DC sputter machine.

Photoelectrical measurements. A high impedance electrometer (Keithley 6517B) acted as a voltage source (IV-characteristics, switching voltage) and simultaneously measured the current. The samples were illuminated by a diode laser (Cobolt 06 MLD) with a wavelength of 405 nm and 30 mW power.

Raman spectroscopy. Spatial-resolved Raman scattering experiments were recorded using a confocal Raman microscope setup (Renishaw, inVia) which was equipped with a 532 nm laser as excitation source, notch filter, a turnable grating (1800 lines mm⁻¹), and a CCD camera. Circular laser polarization was provided by inserting a quarter-wave plate into the excitation laser beam. A ×100 objective was used to focus the laser spot (1 μm) on the sample and to collect the scattered Raman light, respectively. A spatial resolution below the laser spot size was achieved by using the StreamLine™ high-resolution mode of the Raman instrument. In this mode, an increased spatial resolution is achieved by reducing the read-out area of the CCD detector during signal recording. Prior to the measurement, the instrument was calibrated to a band at 520.4 cm⁻¹ of a polycrystalline silicon disc. The sample was placed on a xy-stage (Renishaw) and an area of 7.6 × 7.6 μm² was scanned using streamline-high resolution mode. The laser intensity was set to 5% (~1.5 mW) and spectra between 100 and 700 cm⁻¹ were recorded for 2 s per measurement point. Data were analyzed by a principle component analysis (PCA) with two components using the WiRE 3.4 software (Renishaw).

Data availability

The data that support the findings of this study are available from the corresponding author upon reasonable request.

Received: 7 July 2020; Accepted: 1 December 2020;

Published online: 12 January 2021

References

- Bhatnagar, A., Roy Chaudhuri, A., Heon Kim, Y., Hesse, D. & Alexe, M. Role of domain walls in the abnormal photovoltaic effect in BiFeO₃. *Nat. Commun.* **4**, 143 (2013).
- Knoche, D. S. et al. Domain and switching control of the bulk photovoltaic effect in epitaxial BiFeO₃ thin films. *Sci. Rep.* **9**, 13979 (2019).
- Pintilie, L., Vrejoiu, I., Le Rhun, G. & Alexe, M. Short-circuit photocurrent in epitaxial lead zirconate-titanate thin films. *J. Appl. Phys.* **101**, 064109 (2007).
- Yang, S. Y. et al. Above-bandgap voltages from ferroelectric photovoltaic devices. *Nat. Nanotechnol.* **5**, 143–147 (2010).
- Sturman, P. J. & Fridkin, V. M. *Photovoltaic and Photo-refractive Effects in Noncentrosymmetric Materials* (Taylor & Francis Ltd, 1992).
- Zhang, Y., de Juan, F., Grushin, A. G., Felser, C. & Sun, Y. Strong bulk photovoltaic effect in chiral crystals in the visible spectrum. *Phys. Rev. B* **100**, 245206 (2019).
- Li, J. & Haney, P. M. Circular photogalvanic effect in organometal halide perovskite CH₃NH₃PbI₃. *Appl. Phys. Lett.* **109**, 193903 (2016).
- Liu, X. et al. Circular photogalvanic spectroscopy of Rashba splitting in 2d hybrid organic-inorganic perovskite multiple quantum wells. *Nat. Commun.* **11**, 323 (2020).
- Ivchenko, E. L. & Pikus, G. E. New photogalvanic effect in gyrotropic crystals. *Sov. J. Exp. Theor. Phys. Lett.* **27**, 604 (1978).
- Belinicher, V. Space-oscillating photocurrent in crystals without symmetry center. *Phys. Lett. A* **66**, 213–214 (1978).
- Asnin, V. M. et al. Observation of a photo-emf that depends on the sign of the circular polarization of the light. *ZhETF Pisma Redaktsiiu* **28**, 80–84 (1978).
- Belinicher, V. I. & Sturman, B. I. The photogalvanic effect in media lacking a center of symmetry. *Sov. Phys. Uspekhi* **23**, 199–223 (1980).
- Rashba, E. Properties of semiconductors with an extremum loop. 1. cyclotron and combination resonance in a magnetic field perpendicular to the plane of the loop. *Sov. Phys. Solid State* **2**, 1109–1122 (1960).
- Ogawa, N., Bahramy, M. S., Kaneko, Y. & Tokura, Y. Photocontrol of Dirac electrons in a bulk Rashba semiconductor. *Phys. Rev. B* **90**, 125122 (2014).
- Zhang, Q. et al. Strong circular photogalvanic effect in ZnO epitaxial films. *Appl. Phys. Lett.* **97**, 041907 (2010).
- Weber, W. et al. Demonstration of Rashba spin splitting in gan-based heterostructures. *Appl. Phys. Lett.* **87**, 262106 (2005).
- Niesner, D. et al. Structural fluctuations cause spin-split states in tetragonal CH₃NH₃PbI₃ as evidenced by the circular photogalvanic effect. *Proc. Natl Acad. Sci. USA* **115**, 9509–9514 (2018).
- Kubel, F. & Schmid, H. Structure of a ferroelectric and ferroelastic monodomain crystal of the perovskite BiFeO₃. *Acta Crystallogr. Sect. B Struct. Sci.* **B46**, 698–702 (1990).
- Sando, D. et al. Revisiting the optical band gap in epitaxial BiFeO₃ thin films. *Adv. Optical Mater.* **6**, 1700836 (2018).
- Johann, F., Morelli, A., Biggemann, D., Arredondo, M. & Vrejoiu, I. Epitaxial strain and electric boundary condition effects on the structural and ferroelectric properties of BiFeO₃ films. *Phys. Rev. B* **84**, 094105 (2011).
- Solmaz, A. et al. Domain selectivity in BiFeO₃ thin films by modified substrate termination. *Adv. Funct. Mater.* **26**, 2882–2889 (2016).
- Yun, Y., Ramakrishnegowda, N., Park, D.-S. & Bhatnagar, A. Long range ordering of 71° domain walls in epitaxial BiFeO₃ thin films. *Appl. Phys. Lett.* **113**, 042901 (2018).
- Zhao, T. et al. Electrical control of antiferromagnetic domains in multiferroic BiFeO₃ films at room temperature. *Nat. Mater.* **5**, 823–829 (2006).
- Sando, D. et al. Crafting the magnonic and spintronic response of BiFeO₃ films by epitaxial strain. *Nat. Mater.* **12**, 641–646 (2013).
- Gross, I. et al. Real-space imaging of non-collinear antiferromagnetic order with a single-spin magnetometer. *Nature* **549**, 252–256 (2017).
- Haykal, A. et al. Antiferromagnetic textures in BiFeO₃ controlled by strain and electric field. *Nat. Commun.* **11**, 1704 (2020).
- Dürr, H. A. Chiral magnetic domain structures in ultrathin FePd films. *Science* **284**, 2166–2168 (1999).
- Uecker, R. et al. Properties of rare-earth scandate single crystals (Re = Nd-Dy). *J. Cryst. Growth* **310**, 2649–2658 (2008).
- Fridkin, V. M. *Photoferroelectrics*, vol. 9 of *Springer series in solid-state sciences* (Springer-Vlg, Berlin and New York, 1979).
- Picozzi, S. Ferroelectric Rashba semiconductors as a novel class of multifunctional materials. *Frontiers in Physics* **2**, 10 (2014).
- Barron, L. D. *Molecular Light Scattering and Optical Activity*, vol. 39 (Cambridge University Press, 2009).
- Talkenberger, A. et al. Raman spectroscopic investigations of epitaxial BiFeO₃ thin films on rare earth scandate substrates. *J. Raman Spectrosc.* **46**, 1245–1254 (2015).
- Himcinschi, C. et al. Ferroelastic domain identification in BiFeO₃ crystals using Raman spectroscopy. *Sci. Rep.* **9**, 379 (2019).
- Sander, A., Christl, M., Chiang, C.-T., Alexe, M. & Widdra, W. Domain imaging on multiferroic BiFeO₃ (001) by linear and circular dichroism in threshold photoemission. *J. Appl. Phys.* **118**, 224102 (2015).
- Sosnowska, I., Neumaier, T. P. & Steichele, E. Spiral magnetic ordering in bismuth ferrite. *Phys. Lett. A* **15**, 4835–4846 (1982).
- Lebeugle, D. et al. Electric-field-induced spin flop in BiFeO₃ single crystals at room temperature. *Phys. Rev. Lett.* **100**, 227602 (2008).
- Johnson, R. D. et al. X-ray imaging and multiferroic coupling of cycloidal magnetic domains in ferroelectric monodomain BiFeO₃. *Phys. Rev. Lett.* **110**, 217206 (2013).
- Chauléau, J.-Y. et al. Electric and antiferromagnetic chiral textures at multiferroic domain walls. *Nat. Mater.* **19**, 386–390 (2020).
- Agbelele, A. et al. Strain and magnetic field induced spin-structure transitions in multiferroic BiFeO₃. *Adv. Mater.* **29**, 1602327 (2017).
- Bertinshaw, J. et al. Direct evidence for the spin cycloid in strained nanoscale bismuth ferrite thin films. *Nat. Commun.* **7**, 12664 (2016).
- Bai, F. et al. Destruction of spin cycloid in (111)_c-oriented BiFeO₃ thin films by epitaxial constraint: enhanced polarization and release of latent magnetization. *Appl. Phys. Lett.* **86**, 032511 (2005).
- Béa, H., Bibes, M., Petit, S., Kreisel, J. & Barthélémy, A. Structural distortion and magnetism of BiFeO₃ epitaxial thin films: a Raman spectroscopy and neutron diffraction study. *Philos. Mag. Lett.* **87**, 165–174 (2007).
- Sando, D. et al. Interfacial strain gradients control nanoscale domain morphology in epitaxial BiFeO₃ multiferroic films. *Adv. Funct. Mater.* **30**, 2000343 (2020).

Acknowledgements

We thank Prof. Kathrin Dörr and Dr. Diana Rata for the X-ray measurements, Marian Lisa for the technical support, Dr. Bodo Fuhrmann and Dipl.-Phys. Sven Schlenker for their support with the facilities at the Interdisziplinäre Zentrum für Materialwissenschaften (IZM). Financial support from Bundesministerium für Bildung und Forschung (BMBF) Project No. 03Z22HN12, Deutsche Forschungsgemeinschaft (DFG) within Sonderforschungsbereiche (SFB) 762 (project A12), and Europäischen Fonds für regionale Entwicklung (EFRE) Sachsen-Anhalt is gratefully acknowledged.

Author contributions

A.B. and D.S.K. designed and conceived the experiments. D.S.K. was responsible for thin film growth, PFM analysis, and photoelectric measurements. Y.Y. and L.M. participated in structural characterization. M.S. performed the Raman scattering experiments. A.B. and D.S.K. co-wrote the manuscript with inputs from all the co-authors

Funding

Open Access funding enabled and organized by Projekt DEAL.

Competing interests

The authors declare no competing interests.

Additional information

Supplementary information is available for this paper at <https://doi.org/10.1038/s41467-020-20446-z>.

Correspondence and requests for materials should be addressed to A.B.

Peer review information *Nature Communications* thanks the anonymous reviewer(s) for their contribution to the peer review of this work. Peer reviewer reports are available.

Reprints and permission information is available at <http://www.nature.com/reprints>

Publisher's note Springer Nature remains neutral with regard to jurisdictional claims in published maps and institutional affiliations.



Open Access This article is licensed under a Creative Commons Attribution 4.0 International License, which permits use, sharing, adaptation, distribution and reproduction in any medium or format, as long as you give appropriate credit to the original author(s) and the source, provide a link to the Creative Commons license, and indicate if changes were made. The images or other third party material in this article are included in the article's Creative Commons license, unless indicated otherwise in a credit line to the material. If material is not included in the article's Creative Commons license and your intended use is not permitted by statutory regulation or exceeds the permitted use, you will need to obtain permission directly from the copyright holder. To view a copy of this license, visit <http://creativecommons.org/licenses/by/4.0/>.

© The Author(s) 2021

5.S Supplementary Information

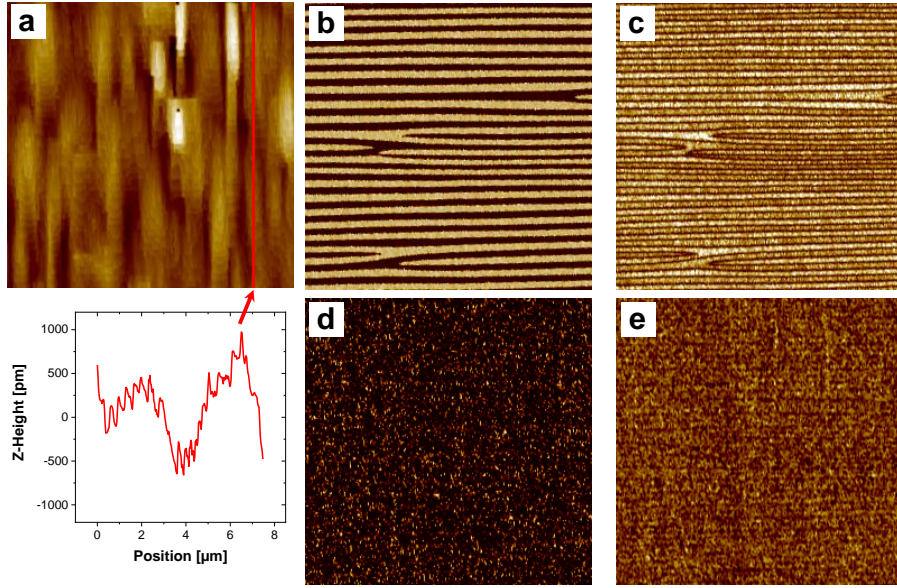


Figure 5.S1: Scanning Probe Microscopy. **a** Atomic force microscopy image revealing the surface of a BiFeO₃/DyScO₃ thin film (top) and line scan of marked line (bottom). Lateral **b** phase and **c** amplitude piezo-response force microscopy (PFM) images. Vertical **d** phase and **e** amplitude PFM image. All images acquired simultaneously with a scanning area of 7.5 × 7.5 μm².

Tensorial Analysis of the BPV Effect in BiFeO₃

Derivation of BPV tensors

Application of symmetry operation for point group 3m to general 3rd rank tensor

Symmetry operations matrices:

Threefold rotation (3) parallel to Z₃ and mirror (m) parallel to Z₁:

$$3 \parallel Z_3 \begin{pmatrix} -\frac{1}{2} & \frac{\sqrt{3}}{2} & 0 \\ -\frac{\sqrt{3}}{2} & -\frac{1}{2} & 0 \\ 0 & 0 & 1 \end{pmatrix}, m \perp Z_1 \begin{pmatrix} -1 & 0 & 0 \\ 0 & 1 & 0 \\ 0 & 0 & 1 \end{pmatrix} \quad (5.S1)$$

Resulting 3rd rank tensor:¹

$$\begin{pmatrix} 0 & \beta_{222} & \beta_{223} & -\beta_{222} & 0 & 0 & \beta_{311} & 0 & 0 \\ -\beta_{222} & 0 & 0 & 0 & \beta_{222} & \beta_{223} & 0 & \beta_{311} & 0 \\ \beta_{131} & 0 & 0 & 0 & \beta_{131} & 0 & 0 & 0 & \beta_{333} \end{pmatrix} \quad (5.S2)$$

Phenomenological expression of BPV²

The BPV effect can be described with following equation:

$$j_i = I\beta_{ijk}E_jE_k^* \quad (5.S3)$$

The real part of β_{ijk} is symmetric and imaginary part of β_{ijk} is antisymmetric:

$$\text{Re } \beta_{ijk} = \text{Re } \beta_{ikj} = \beta_{ijk}^L; \quad \text{Im } \beta_{ijk} = -\text{Im } \beta_{ikj} = \beta_{ijk}^C \quad (5.S4)$$

The current expression becomes:

$$j_i = j_i^L + j_i^C = I (\beta_{ijk}^L + i\beta_{ijk}^C) E_j E_k^* \quad (5.S5)$$

The nonsymmetric elements of the general 3rd rank tensor can be rewritten as having symmetric and antisymmetric parts. This leads to the symmetric part (LBPV) and antisymmetric part (CBPV).

Separation of 3rd rank tensor in symmetric and antisymmetric part

$$\beta_{ijk}^L = \left(\begin{array}{ccc|ccc} 0 & -\beta_{222}^L & \beta_{131}^L & -\beta_{222}^L & 0 & 0 \\ -\beta_{222}^L & 0 & 0 & 0 & \beta_{222}^L & \beta_{131}^L \\ \beta_{131}^L & 0 & 0 & 0 & \beta_{131}^L & 0 \\ \hline \beta_{311}^L & 0 & 0 & 0 & \beta_{311}^L & 0 \\ 0 & \beta_{311}^L & 0 & 0 & 0 & \beta_{333}^L \end{array} \right) \quad (5.S6)$$

$$\beta_{ijk}^C = \left(\begin{array}{ccc|ccc} 0 & 0 & -\beta_{131}^C & 0 & 0 & 0 \\ 0 & 0 & 0 & 0 & 0 & -\beta_{131}^C \\ \beta_{131}^C & 0 & 0 & 0 & \beta_{131}^C & 0 \\ \hline 0 & 0 & 0 & 0 & 0 & 0 \\ 0 & 0 & 0 & 0 & 0 & 0 \\ 0 & 0 & 0 & 0 & 0 & 0 \end{array} \right) \quad (5.S7)$$

Transformation of LBPV (symmetric BPV) tensor into matrix notation^{3,4}

(5.S6) is transformed into the corresponding 3x6 matrix β_{il}^L . If $l = 1, 2, 3$, then $\beta_{il}^L = \beta_{iil}^L$ and if $l = 4, 5, 6$, then $\beta_{il}^L = 2\beta_{ijk}^L$.

$$\beta_{il}^L = \begin{pmatrix} 0 & 0 & 0 & 0 & \beta_{15}^L & -2\beta_{22}^L \\ -\beta_{22}^L & \beta_{22}^L & 0 & \beta_{15}^L & 0 & 0 \\ \beta_{31}^L & \beta_{31}^L & \beta_{33}^L & 0 & 0 & 0 \end{pmatrix} \quad (5.S8)$$

The appearance of β_{il}^L is analogous to the piezoelectric tensor d_{ij} .

Transformation of CBPV (antisymmetric BPV) into 2nd rank pseudo-tensor⁵

(5.S7) can be transformed into a pseudo-tensor using the Levi-Civita symbol ϵ_{ijk} :

$$\beta_{il}^C = \epsilon_{ijk} \beta_{ijk}^A \quad (5.S9)$$

The resulting 2nd rank pseudo-tensor is:

$$\beta_{ij}^C = \begin{pmatrix} 0 & +\beta_{12}^C & 0 \\ -\beta_{12}^C & 0 & 0 \\ 0 & 0 & 0 \end{pmatrix} \quad (5.S10)$$

The appearance β_{ij}^C is analogous to the gyrotropic axial (pseudo-)tensor g_{lk} , which is connected to the natural optical activity tensor γ_{ij}^A using the Levi-Civita symbol ϵ_{ijk} .^{6,7}

Tensorial calculation for ordered striped 71° domain pattern

Relation between coordinate system based on hexagonal and pseudo-cubic crystal system

The standard axes of physical properties follow the IEEE standard setting. For trigonal crystals, the convention is based on the hexagonal crystal system. Therefore, the z axis of physical properties is set along the c crystallographic axis. The x axis is set along the a crystallographic axis and the y axis is orthogonal to the other completing the right-hand cartesian coordinate system. To calculate the BPV response for the experimental setup, it is necessary to move to a coordinate system which is related to the used axis in the setup.

A three-dimensional coordinate system can be transformed into another arbitrary three-dimensional coordinate system using a 3x3 matrix. Regarding the symmetry relations shown in Figure 5.S2, the coordinate system of the physical properties based on the hexagonal crystal system (x_h, y_h, z_h) can be transformed into the pseudo-cubic coordinate system (x_{pc}, y_{pc}, z_{pc}) using following matrix:

$$a_{ij} = a_{P_L} = \begin{pmatrix} 0 & \frac{2}{\sqrt{6}} & \frac{1}{\sqrt{3}} \\ -\frac{1}{\sqrt{2}} & -\frac{1}{\sqrt{6}} & \frac{1}{\sqrt{3}} \\ \frac{1}{\sqrt{2}} & -\frac{1}{\sqrt{6}} & \frac{1}{\sqrt{3}} \end{pmatrix} \quad (5.S11)$$

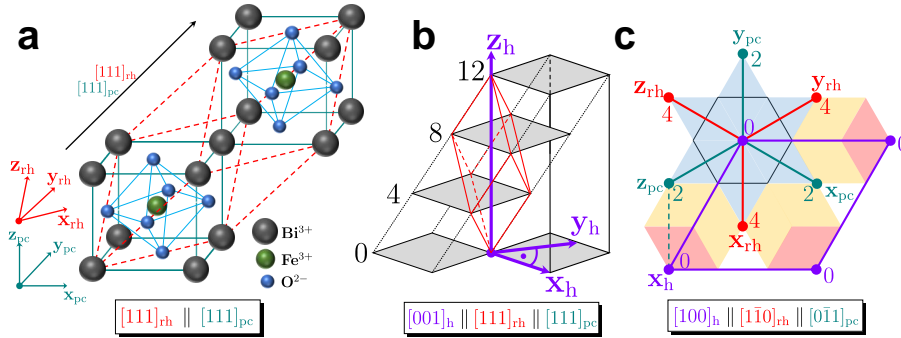


Figure 5.S2: Coordinate system transformation between different crystal systems.

a Relation between pseudo-cubic and rhombohedral coordinate system.⁸ The rhombohedral unit cell can be described with two ABO_3 cubic unit cells. **b** Relation between rhombohedral and hexagonal crystal system (Adapted from⁹). **c** Projection along triad axis (Adapted from¹⁰). The numbers depict the position height with respect to the hexagonal unit cell (unit: $c_h/12$).

The index P_L refers to the domain variants P_L (Figure 1 (c),(d) main text) with the polarization pointing along the $[111]_{pc}$ direction. To describe the response for the domain variants P_R the resulting response has been rotated by $+90^\circ$ (CCW) around the $[001]_{pc}$ direction:

$$a_{P_R} = \begin{pmatrix} \cos(\frac{\pi}{2}) & \sin(\frac{\pi}{2}) & 0 \\ -\sin(\frac{\pi}{2}) & \cos(\frac{\pi}{2}) & 0 \\ 0 & 0 & 1 \end{pmatrix} a_{P_L} = \begin{pmatrix} 0 & 1 & 0 \\ -1 & 0 & 0 \\ 0 & 0 & 1 \end{pmatrix} a_{P_L} = \begin{pmatrix} -\frac{1}{\sqrt{2}} & -\frac{1}{\sqrt{6}} & \frac{1}{\sqrt{3}} \\ 0 & -\frac{2}{\sqrt{6}} & -\frac{1}{\sqrt{3}} \\ \frac{1}{\sqrt{2}} & -\frac{1}{\sqrt{6}} & \frac{1}{\sqrt{3}} \end{pmatrix} \quad (5.S12)$$

LBPV response

For light wave with linear polarization propagating along [001]_{pc}:

$$(E_j)_{\text{L}}^{\text{pc}} = \begin{pmatrix} \cos \theta \\ \sin \theta \\ 0 \end{pmatrix}, (E_j)_{\text{L}}^{\text{h}} = a_{\text{L}}^{\text{T}}(E_j)_{\text{L}}^{\text{pc}} = \begin{pmatrix} -\frac{\sin(\theta)}{\sqrt{2}} \\ \frac{2\cos(\theta)}{\sqrt{6}} - \frac{\sin(\theta)}{\sqrt{3}} \\ \frac{\sin(\theta)}{\sqrt{3}} + \frac{\cos(\theta)}{\sqrt{3}} \end{pmatrix} \quad (5.S13)$$

The orientation of the light wave with respect to the R-configuration is shifted by 90° clockwise, which leads to:

$$(E_j)_{\text{R}}^{\text{pc}} = \begin{pmatrix} \cos(\theta + \frac{\pi}{2}) \\ \sin(\theta + \frac{\pi}{2}) \\ 0 \end{pmatrix} = E_j^{\text{pc}} = \begin{pmatrix} -\sin \theta \\ \cos \theta \\ 0 \end{pmatrix}, (E_j)_{\text{R}}^{\text{h}} = a_{\text{L}}^{\text{T}}(E_j)_{\text{R}}^{\text{pc}} = \begin{pmatrix} -\frac{\cos(\theta)}{\sqrt{2}} \\ -\frac{2\sin(\theta)}{\sqrt{6}} - \frac{\cos(\theta)}{\sqrt{3}} \\ \frac{\cos(\theta)}{\sqrt{3}} - \frac{\sin(\theta)}{\sqrt{3}} \end{pmatrix} \quad (5.S14)$$

The overall response in the pseudo-cubic coordinate system can be now calculated:

$$j_{\text{L}}^{\text{L}} = \frac{I}{2} [[a_{\text{R}}[\beta_{ij}^{\text{L}}[(EE)_{\text{R}}]_{\text{R}}^{\text{h}}] + a_{\text{L}}[\beta_{ij}^{\text{L}}[(EE)_{\text{L}}]_{\text{L}}^{\text{h}}]]]$$

$$= I \begin{pmatrix} \left(\frac{\beta_{33}^{\text{L}}}{3\sqrt{3}} + \frac{2\beta_{31}^{\text{L}}}{3\sqrt{3}} + \frac{\beta_{22}^{\text{L}}}{3\sqrt{6}} + \frac{\beta_{15}^{\text{L}}}{6\sqrt{3}} \right) + \left(\frac{\beta_{22}^{\text{L}}}{\sqrt{6}} + \frac{\beta_{15}^{\text{L}}}{2\sqrt{3}} \right) \cos(2\theta) \\ \left(\frac{\beta_{33}^{\text{L}}}{3\sqrt{3}} - \frac{\beta_{31}^{\text{L}}}{3\sqrt{3}} - \frac{2\beta_{22}^{\text{L}}}{3\sqrt{6}} + \frac{\beta_{15}^{\text{L}}}{6\sqrt{3}} \right) \sin(2\theta) \\ \left(\frac{2\beta_{22}^{\text{L}}}{3\sqrt{6}} + \frac{\beta_{15}^{\text{L}}}{3\sqrt{3}} - \frac{\beta_{33}^{\text{L}}}{3\sqrt{3}} - \frac{2\beta_{31}^{\text{L}}}{3\sqrt{3}} \right) \end{pmatrix} \quad (5.S15)$$

CBPV response

The circularly-polarized light propagates in [001]_{pc} direction.

Left-handed circularly polarized light (LCP)

Jones vector:

$$\mathbf{e}_{\text{LCP,pc}} = \begin{pmatrix} \frac{1}{\sqrt{2}} \\ \frac{i}{\sqrt{2}} \\ 0 \end{pmatrix}, \mathbf{e}_{\text{LCP,h}} = \begin{pmatrix} -\frac{i}{2} \\ \frac{\sqrt{2}}{\sqrt{6}} - \frac{i}{\sqrt{2}\sqrt{6}} \\ \frac{1}{\sqrt{2}\sqrt{3}} + \frac{i}{\sqrt{2}\sqrt{3}} \end{pmatrix} \quad (5.S16)$$

CBPV response for LCP light for each domain variant:

$$j_{\text{i,PL}}^{\text{LCP}} = \frac{I}{2} a_{\text{PL}} \beta_{ij}^{\text{C}} i [\mathbf{e}_{\text{LCP,h}} \times \mathbf{e}_{\text{LCP,h}}^*] = \frac{I}{2\sqrt{3}} \begin{pmatrix} -\beta_{12}^{\text{C}} \\ +\beta_{12}^{\text{C}} \\ 0 \end{pmatrix} \quad (5.S17)$$

$$j_{\text{i,PR}}^{\text{LCP}} = \frac{I}{2} a_{\text{PR}} \beta_{ij}^{\text{C}} i [\mathbf{e}_{\text{LCP,h}} \times \mathbf{e}_{\text{LCP,h}}^*] = \frac{I}{2\sqrt{3}} \begin{pmatrix} +\beta_{12}^{\text{C}} \\ +\beta_{12}^{\text{C}} \\ 0 \end{pmatrix} \quad (5.S18)$$

Overall CBPV response for LCP light:

$$j_i^{\text{LCP}} = \frac{I}{2} [a_{\text{PR}} (\beta_{ij}^{\text{C}} i [\mathbf{e}_{\text{LCP,h}} \times \mathbf{e}_{\text{LCP,h}}^*]) + a_{\text{PL}} (\beta_{ij}^{\text{C}} i [\mathbf{e}_{\text{LCP,h}} \times \mathbf{e}_{\text{LCP,h}}^*])] = \frac{I}{\sqrt{3}} \begin{pmatrix} 0 \\ +\beta_{12}^{\text{C}} \\ 0 \end{pmatrix} \quad (5.S19)$$

Right-handed circularly polarized light (RCP)

$$\mathbf{e}_{\text{RCP,pc}} = \begin{pmatrix} \frac{1}{\sqrt{2}} \\ -\frac{i}{\sqrt{2}} \\ 0 \end{pmatrix}, \mathbf{e}_{\text{RCP,h}} = \begin{pmatrix} \frac{\sqrt{2}}{\sqrt{6}} + \frac{i}{2} \\ \frac{1}{\sqrt{2}\sqrt{3}} - \frac{i}{\sqrt{2}\sqrt{3}} \\ 0 \end{pmatrix} \quad (5.S20)$$

CBPV response for RCP light for each domain variant:

$$j_{i,\text{PL}}^{\text{RCP}} = \frac{I}{2} a_{\text{PL}} \beta_{ij}^{\text{C}} i [\mathbf{e}_{\text{RCP,h}} \times \mathbf{e}_{\text{RCP,h}}^*] = \frac{I}{2\sqrt{3}} \begin{pmatrix} +\beta_{12}^{\text{C}} \\ -\beta_{12}^{\text{C}} \\ 0 \end{pmatrix} \quad (5.S21)$$

$$j_{i,\text{PR}}^{\text{RCP}} = \frac{I}{2} a_{\text{PR}} \beta_{ij}^{\text{C}} i [\mathbf{e}_{\text{RCP,h}} \times \mathbf{e}_{\text{RCP,h}}^*] = \frac{I}{2\sqrt{3}} \begin{pmatrix} -\beta_{12}^{\text{C}} \\ -\beta_{12}^{\text{C}} \\ 0 \end{pmatrix} \quad (5.S22)$$

Overall CBPV response for RCP light:

$$j_i^{\text{RCP}} = \frac{I}{2} [a_{\text{PR}} (\beta_{ij}^{\text{C}} i [\mathbf{e}_{\text{RCP,h}} \times \mathbf{e}_{\text{RCP,h}}^*]) + a_{\text{PL}} (\beta_{ij}^{\text{C}} i [\mathbf{e}_{\text{RCP,h}} \times \mathbf{e}_{\text{RCP,h}}^*])] = \frac{I}{\sqrt{3}} \begin{pmatrix} 0 \\ -\beta_{12}^{\text{C}} \\ 0 \end{pmatrix} \quad (5.S23)$$

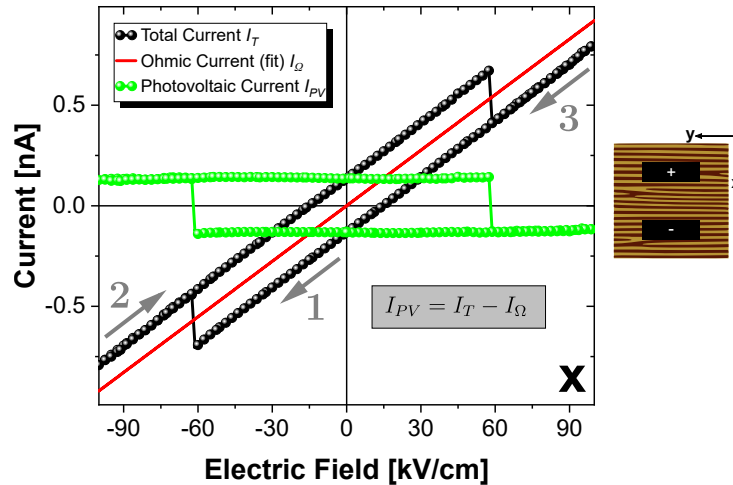


Figure 5.S3: Switchability of the photovoltaic effect. Current as a function of applied electric field under illumination with linearly polarized laser light $\lambda = 405$ nm in $[100]_{\text{pc}}$ (black). At ± 60 kV cm⁻¹, there is an abrupt current rise/drop. This apparent change is connected to the ferroelectric switching and therefore an opposing of the BPV orientation. By subtracting the ohmic conduction (red) from the overall response, a hysteretic behavior of the photovoltaic current (green) can be subtracted.

5. Anomalous Circular BPV Effect in BiFeO₃ Thin Films with Stripe-Domain Pattern

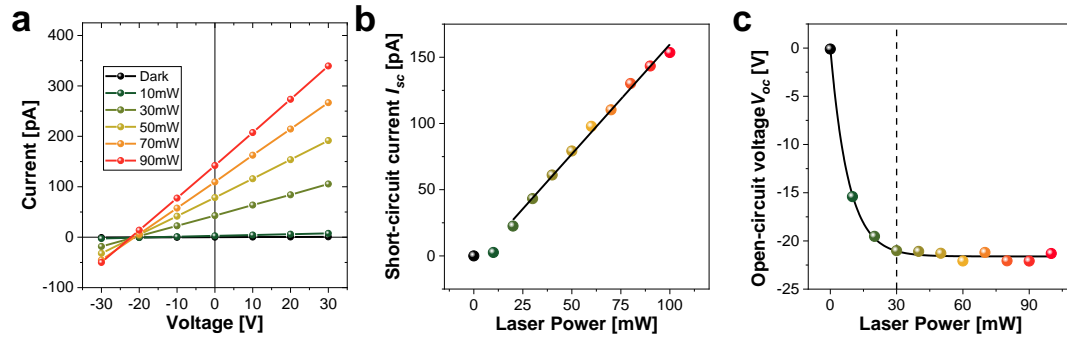


Figure 5.S4: Photovoltaic properties as a function of light intensity. **a** Current-voltage characteristic under illumination with right-handed circularly polarized (LCP) light with different laser power settings. **b** Extracted short-circuit current I_{sc} and **c** open-circuit voltage V_{oc} as a function of the laser power.

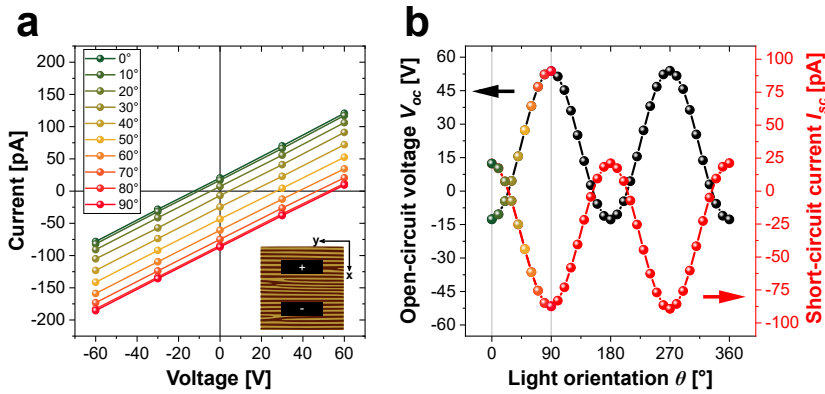


Figure 5.S5: Extraction of photovoltaic properties from current-voltage characteristics. **a** Current-voltage (IV) characteristics for different orientations ($0^\circ \parallel \mathbf{x}$, CCW rotation) of the linearly polarized light. The electrode geometry is shown in the inset. **b** Open-circuit voltage V_{oc} and short-circuit current I_{sc} as a function of the light orientation θ . Both photovoltaic properties can be extracted from a linear fit of the IV characteristics.

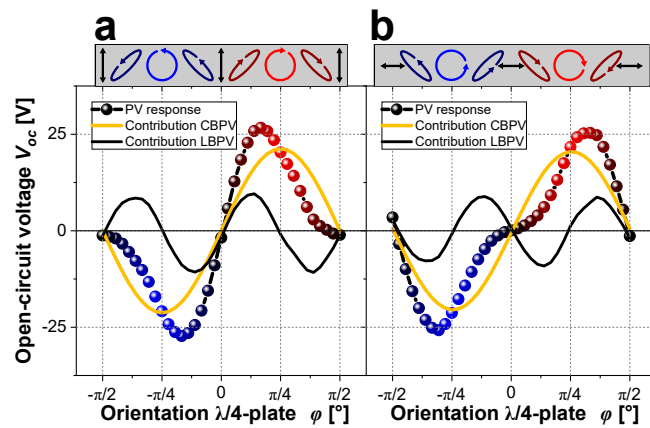


Figure 5.S6: Comparison between different orientations of outgoing light polarization. Open-circuit voltage V_{oc} as a function of the $\lambda/4$ plate orientation ϕ for two different adjustments of the subsequent $\lambda/2$ plate. The starting linear light polarization is aligned along **a** $[100]_{pc}$ and **b** $[010]_{pc}$, respectively (Compare schematics of the polarization state shown at the top).

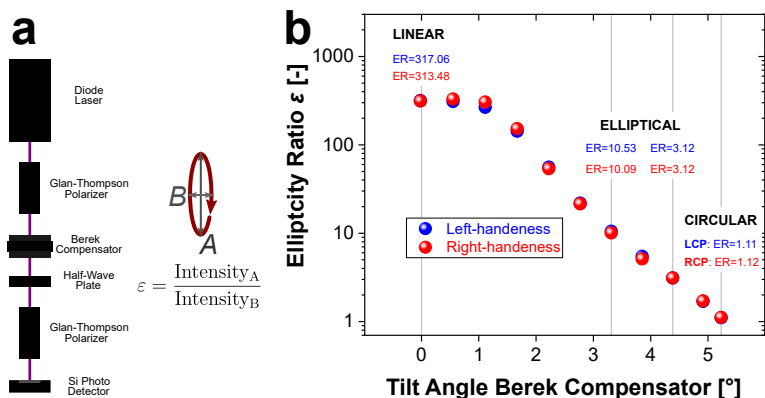


Figure 5.S7: Light polarization characterization. **a** Schematic of the light polarization characterization setup. The set light polarization is rotated using the subsequent half-wave plate and the laser power for the major (A) and minor (B) axis is measured using a silicon photo detector (Thorlabs, DET100A2). **b** Ellipticity ratio ϵ as a function of the tilt angle of the Berek Compensator. Depending on the tilt angle, the pathway of the light through the birefringent MgF₂ plate is changed. This changes the resulting retardance and thus the outcoming light polarization from linear to elliptical to circular.

Raman Scattering Experiments

To explain the unexpected CBPV response in our films, we propose the existence of opposite circular dichroism for the different polarization variants. Consequently, CD spectra for each polarization variant are needed. To the best of our knowledge, commercially available CD spectrometers (mostly equipped with a Xe lamp) are not capable of resolving structure in the submicrometer range. However, circular dichroism has been observed using laser-based threshold photoemission electron microscopy (PEEM) in a BiFeO₃ single crystal with multi-domain state.¹¹

Having this observation in mind, we conceived a Raman scattering experiment following partially the basic principle of Raman Optical Activity (ROA) in collaboration with our colleagues. The Raman spectra were acquired using a confocal Raman microscope setup (Renishaw, InVia). The sample was placed on an xy -stage providing a 100 nm positioning resolution. The polarization state of the excitation laser light (532 nm) is tuned from linear to circular by inserting a quarter-wave plate. In order to gain information from a very localized region of the sample, we focused the laser beam to a spot size of $\sim 1 \mu\text{m}$. A spatial resolution below the laser spot size was achieved by using the StreamLineTM high-resolution mode of the Raman instrument. In this mode, an increased spatial resolution is achieved by reducing the read-out area of the CCD detector during signal recording. A comparison between two spectra observed under illumination with linear (polarization along x -direction) and circular light polarization can be found in Figure 5.S9a. In both spectra three dominant modes at 138 cm^{-1} , 174 cm^{-1} and 222 cm^{-1} were observed. This is in good agreement with previous studies on BiFeO₃/DyScO₃ thin films.¹² Contrarily, Talkenberger *et al.* used a 442 nm linearly polarized excitation laser. Because of the smaller penetration depth of the light ($\sim 75 \text{ nm}$), they did not separate modes at higher wave numbers due to the DyScO₃ substrate (compare spectra of DyScO₃ substrate at the bottom of Figure 5.S9a). Because of this contribution from the substrate, we were not able to observe BiFeO₃ modes at higher wave numbers. In another study, Himcinshi *et al.* used Raman spectroscopy to identify domains with different polarization variants in BiFeO₃

a single crystal.¹³ The change in the Raman signal (peak area of 172 cm⁻¹ mode) due to a different orientation of the linear polarization of the excitation laser towards the corresponding polarization direction was used to map a domain configuration with micrometer-resolution. When performing the Raman scattering experiments, we observed a change of the ratio between the peak intensity of the 138 cm⁻¹ and 174 cm⁻¹ mode, however, under excitation with circularly polarized light. The intensity changes were not as high as shown by Himcinshi *et al.*¹³, which might also be related to the smaller domain size and different excitation wavelength.

To systematically investigate this position-dependent change in the Raman spectra, we characterized a 10×10 μm² region on our sample using piezo-response force microscopy (PFM). The AFM image (Figure 5.S9b) reveals a topography with a similar roughness to the one shown in Figure 1(a) in our manuscript. The in-plane PFM (IP-PFM) phase image (Figure 5.S9c) shows great similarities to Figure 1(b), however, we want to mention the larger domain width in this region (~250 nm compared to ~150 nm in Figure 1(b) main text).

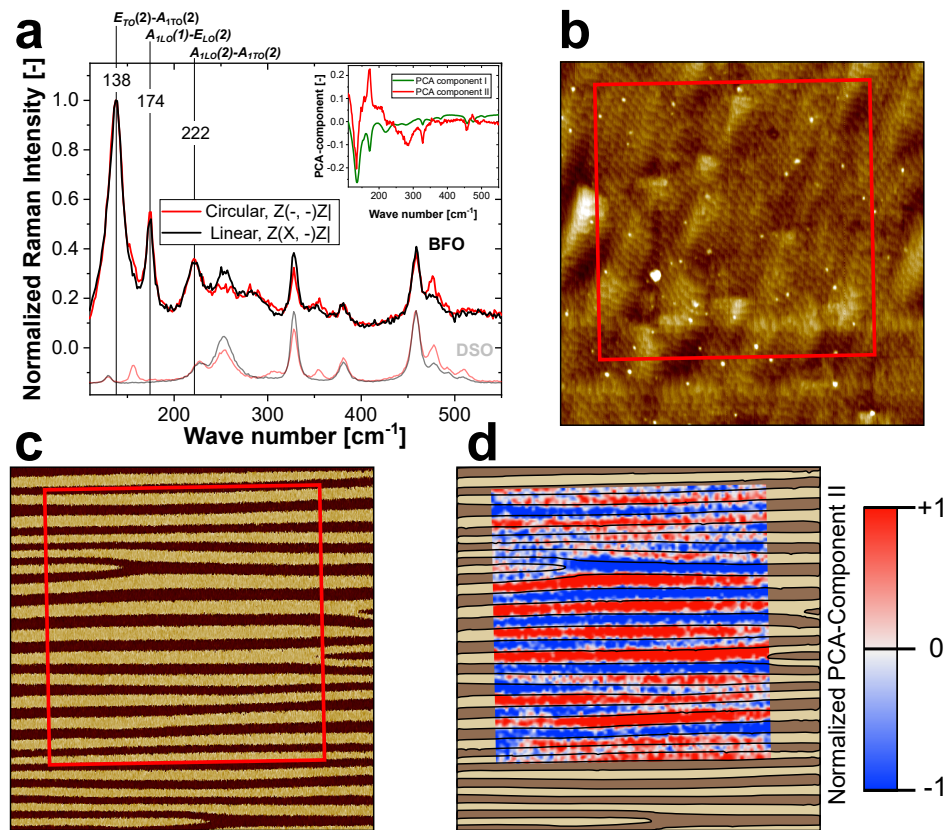


Figure 5.S8: Raman scattering experiments demonstrating the domain-specific light-matter interaction. **a** Normalized Raman spectra of BiFeO₃/DyScO₃ thin film under circular (red) and linear (black) laser light excitation. Bottom: Qualitative Raman spectra of a DyScO₃ substrate. Inset: Both PCA-component used to analyze the spatial-resolved Raman spectra. **b** Topography and **c** in-plane PFM phase image of pre-characterized region (10×10 μm²). The red squares indicate the position of the overlapped map acquired from the spatial-resolved Raman scattering experiments. **d** Normalized PCA-component II map (7.6×7.6 μm²) acquired from the spatial-resolved Raman scattering experiments overlapping the schematic domain configuration extracted from PFM image in **c**. The outline of the map is inserted in **b** and **c** (red square).

Then, we performed spatial-resolved Raman scattering experiments to acquire a two-dimensional grid of Raman spectra in a $8 \times 8 \mu\text{m}^2$ region in the vicinity of the PFM pre-characterized region. The Raman data (~ 6400 spectra) were processed using principal component analysis (PCA) (WiRE 3.4 software, Renishaw), a commonly used tool show data variance. The PCA-analysis divides the Raman spectra into two main components (see inset Figure 5.S9a). The change of the 174cm^{-1} and 138cm^{-1} peak intensity ratio can be represented by the PCA- component II. As a result, the position-dependent PCA-component can be mapped. To compare two characterization techniques, the resultant PCA-component map is overlapped with the IP-PFM phase image (Figure 5.S9d). To match the shape of both patterns, the PCA-component map is resized ($8 \times 8 \mu\text{m}^2 \rightarrow 7.6 \times 7.6 \mu\text{m}^2$). The lowest spatial resolution step of **xy**-positioning stage of the Raman microscope was used and a systemic positioning error while working at the lowest resolution limit could explain the necessity to resize the map to achieve a perfect overlap. However, the spatial resolution of this experiment is limited to $\sim \lambda/2$. For thinner structures, a mixed Raman spectra is obtained and it is not possible to clearly distinguish the different domains (compare Figure 5.S9d upper and lower areas).

The possibility to resolve the ferroelectric domain arrangement using Raman scattering experiments under excitation with CP light suggests differential interaction between CP light and the domains exhibiting different polarization variants.

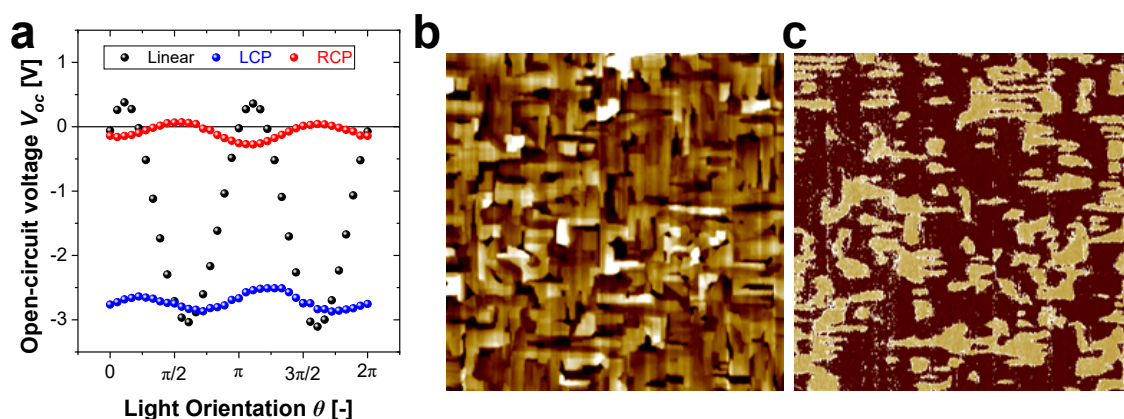


Figure 5.S9: Linear and circular bulk photovoltaic effect in BiFeO₃/SrTiO₃ thin film.

a Open-circuit voltage as a function of the light orientation θ for BiFeO₃/SrTiO₃ under illumination with linearly polarized (LP) light (black), left-handed circularly (LCP) light (blue) and right-handed-circularly polarized (RCP) light (red). **b** Atomic Force Microscopy image and **c** lateral piezo-response Force Microscopy phase image of BiFeO₃/SrTiO₃ sample. All images: $7.5 \times 7.5 \mu\text{m}^2$.

References - CHAPTER 5.S

1. Wilson, D. W., Glytsis, E. N., Hartman, N. F. & Gaylord, T. K. "Beam diameter threshold for polarization conversion photoinduced by spatially oscillating bulk photovoltaic currents in LiNbO₃:Fe". *Journal of the Optical Society of America B* **9**, 1714 (1992).
2. Belinicher, V. I. & Sturman, B. I. "The photogalvanic effect in media lacking a center of symmetry". *Soviet Physics Uspekhi* **23**, 199–223 (1980).
3. Newnham, R. E. *Properties of materials: Anisotropy, symmetry, structure* (Oxford Univ. Press, Oxford, 2004).
4. Nye, J. F. *Physical properties of crystals: Their representation by tensors and matrices* Reprinted. (Clarendon Press, Oxford, 2012).
5. Sturman, B. I. & Fridkin, V. M. *The photovoltaic and photorefractive effects in noncentrosymmetric materials* (Gordon and Breach, Philadelphia, 1992).
6. Gallego, S. V., Etxebarria, J., Elcoro, L., Tasci, E. S. & Perez-Mato, J. M. "Automatic calculation of symmetry-adapted tensors in magnetic and non-magnetic materials: a new tool of the Bilbao Crystallographic Server". *Acta Crystallographica Section A* **75**, 438–447 (2019).
7. Landau, L. D. & Lifshits, E. M. *Electrodynamics of continuous media* 2nd ed., rev (Pergamon, Oxford, 1984).
8. Kubel, F. & Schmid, H. "Structure of a ferroelectric and ferroelastic monodomain crystal of the perovskite BiFeO₃". *Acta Crystallographica Section B, Structural Science*, 698–702 (1990).
9. Buerger, M. J. *X-ray crystallography: An introduction to the investigation of crystals by their diffraction of monochromatic x-radiation* 3. print (Wiley, New York, 1953).
10. Megaw, H. D. & Darlington, C. N. W. "Geometrical and structural relations in the rhombohedral perovskites". *Acta Crystallographica Section A* **31**, 161–173 (1975).
11. Sander, A., Christl, M., Chiang, C.-T., Alexe, M. & Widdra, W. "Domain imaging on multiferroic BiFeO₃ (001) by linear and circular dichroism in threshold photoemission". *Journal of Applied Physics* **118**, 224102 (2015).
12. Talkenberger, A., Vrejoiu, I., Johann, F., Röder, C., Irmer, G., Rafaja, D., Schreiber, G., Kortus, J. & Himcinschi, C. "Raman spectroscopic investigations of epitaxial BiFeO₃ thin films on rare earth scandate substrates". *Journal of Raman Spectroscopy* **46**, 1245–1254 (2015).
13. Himcinschi, C., Rix, J., Röder, C., Rudolph, M., Yang, M.-M., Rafaja, D., Kortus, J. & Alexe, M. "Ferroelastic domain identification in BiFeO₃ crystals using Raman spectroscopy". *Scientific Reports* **9**, 379 (2019).

Summary - CHAPTER 5

In order to investigate the circular BPV effect, the light polarization range of the experimental setup was extended to elliptical and circular polarization. The findings demonstrated the evolution of the bulk photovoltaic effect in BiFeO₃ thin films as the polarization of light was modulated systematically from linear to elliptical to circular. The investigated films were grown on DyScO₃ substrates and revealed a striped arrangement of the ferroelectric domains (Figure 5.1b). The high thin film quality was confirmed by XRD measurements (Figure 5.1d). Initially, the existence of the linear BPV effect was demonstrated by measuring the photovoltaic response while rotating linear light polarization using a half-wave plate (Figure 5.2b). In the second step, a quarter wave plate was introduced to continuously adjust both ellipticity and helicity of the light polarization. Top electrodes running parallel to the net in-plane polarization (perpendicular to the striped domains) were used. The overall BPV response was divided into the contributions from the linear and circular BPV effect (Figure 5.2c). The experimental findings followed the expected behavior derived from a tensorial analysis of both effects. An extended experimental setup, including a Berek compensator to set arbitrary light polarization state and a subsequent half-waveplate to rotate the light polarization main axis (compare Section 3.6, Figure 5.3a), enabled the systematic investigation under linearly, elliptically and circularly polarized light. On one hand, the measurements with electrodes parallel to net in-plane polarization matched the analytical results from the tensorial assessment (Figure 5.3b). On the other hand, measurements with electrodes perpendicular to the net in-plane direction contradicted the analytical results (Figure 5.3c). After considering the circular BPV response for both domain variants separately (Table 5.1), a domain-specific differential light interaction was proposed to explain the observed circular BPV responses. This scenario was further tested with electrodes parallel to the in-plane polarization projection of each domain variant ($\pm 45^\circ$ with respect to the overall net in-plane polarization). Whereas measurements with one electrode geometry revealed an increased V_{oc} value for right-handed and an almost vanishing open-circuit voltage value for left-handed circularly polarized light (Figure 5.4b), measurements with the other electrode geometry showed exactly the opposite behavior (Figure 5.4c). These findings further validated the assumption of a domain-specific differential interaction with circularly polarized light. Additionally, spatially-resolved Raman scattering experiments with circularly polarized light enabled the visualization of the domain structure (Figure 5.S8). This result was confirmed by PFM measurements of the same area. The possibility to image the ferroelectric domain arrangement using Raman scattering experiments under circularly-polarized light is another indicator of the domain-specific differential light-matter interaction. The chiral character of the antiferromagnetic order of BiFeO₃ is one possible reason to explain the anomalous character of both the circular BPV response and the Raman scattering experiments.

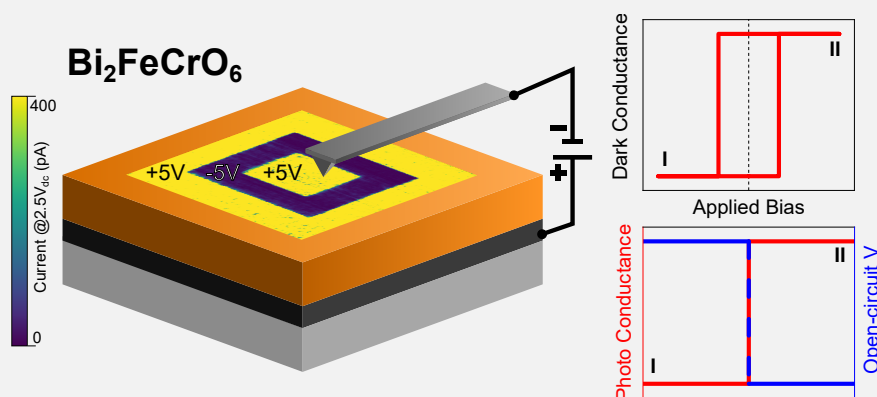
CHAPTER 6

Resistive Switching in Ferroelectric $\text{Bi}_2\text{FeCrO}_6$ Thin Films and Impact on the Photovoltaic Effect

The first two parts of this thesis addressed the fundamental properties of the BPV effect in BiFeO_3 thin films. The last part concentrated on photoelectrical measurements of $\text{Bi}_2\text{FeCrO}_6$ thin films. Although being closely related to its parent material BiFeO_3 , $\text{Bi}_2\text{FeCrO}_6$ reveals improved performance regarding its magnetic (compare Section 2.2.2) and photovoltaic properties (record solar conversion efficiency of perovskite oxides observed in $\text{Bi}_2\text{FeCrO}_6$; compare Section 2.3.3). Different SPM and (photo)electrical measurements with macroscopic top electrodes were performed to investigate epitaxial $\text{Bi}_2\text{FeCrO}_6$ thin films. The experimental findings demonstrated a superior PV performance compared to BiFeO_3 and an unexpected resistive switching behavior.

PUBLISHED AS:

Walch, David S., Yun, Y., Ramakrishnegowda, N., Mühlenbein, L., Lotnyk, A., Himcinschi, C. & Bhatnagar, A. "Resistive Switching in Ferroelectric $\text{Bi}_2\text{FeCrO}_6$ Thin Films and Impact on the Photovoltaic Effect". *Advanced Electronic Materials* **8**, 2200276 (2022)



ToC Figure 6.0: Schematic of the conductive atomic force microscopy measurement revealing the local resistive switching behavior (left). The hysteretic behavior of the dark conductance (right, top) directly influences the photo conductance and the resulting open-circuit voltage (right, bottom).

Resistive Switching in Ferroelectric $\text{Bi}_2\text{FeCrO}_6$ Thin Films and Impact on the Photovoltaic Effect

David S. Walch, Yeseul Yun, Niranjana Ramakrishnegowda, Lutz Mühlenbein, Andriy Lotnyk, Cameliu Himcinschi, and Akash Bhatnagar*

The multiferroic character of $\text{Bi}_2\text{FeCrO}_6$ (BFCO), that is, the coexistence of ferroelectricity and ferromagnetism, has been predicted and demonstrated in different studies. Intriguingly, the material system also exhibits a reduced band gap, in addition to bulk-driven photovoltaic effect. The co-existence of all these attributes in a single system is a rare occurrence and paves way to a multitude of practical applications, with ferroelectric solar cell as one of them. In this work, epitaxially grown BFCO thin films, deposited with pulsed laser deposition on single crystalline SrTiO_3 (STO) substrates, reveal a self-ordered ionic arrangement which is proven with X-ray and transmission electron microscope (TEM) measurements. A lowered band gap and a higher conductivity lead to a superior photovoltaic performance compared to a BiFeO_3 (BFO) reference film. Scanning probe microscopy (SPM) is used to test locally the ferroelectric switching properties. Poling with electric field not only caused a reliable change in the state of polarization, but also resulted in substantial changes in the resistance of the regions. Macroscopic measurements using transparent $\text{In}_2\text{O}_3:\text{Sn}$ (ITO) electrodes demonstrate a bi-directional multi-stage resistive switching, which in turn influences the photovoltaic performance of the heterostructure.

1. Introduction

Magnetolectric multiferroics, that is, materials exhibiting a rare combination of ferroelectricity and ferromagnetism, are of great interest for the development of new-age functional materials.^[1–3] Especially, if the coexistence of the two ferroic orders manifests via a strong coupling, the materials can be used for ferroelectric data storage devices with magnetic readout. $\text{Bi}_2\text{FeCrO}_6$ (BFCO) has been theoretically predicted as one of the most promising candidate in this context, with a large spontaneous polarization and magnetization.^[4,5] The multiferroic character has been confirmed experimentally in epitaxial BFCO thin films.^[6–8]

Beyond, an anomalous photovoltaic effect, also known as bulk photovoltaic (BPV) effect, is relevant for crystals lacking inversion symmetry, and thus also for all ferroelectrics.^[9–12] The BPV effect depends on the light polarization state

and the orientation of the ferroelectric polarization.^[13–15] Subsequent experiments on the optical properties of BFCO thin films indeed unraveled a photovoltaic effect which was found to be sensitive to the orientation of the ferroelectric polarization.^[16–18] Interestingly, the effective band gap may be adjusted by tuning the ionic ordering within the film^[19,20] and thus the development of a multilayer BFCO device achieved a solar conversion efficiency of 8.1% under AM1.5 illumination, the highest reported from a ferroelectric until now.^[21] A necessary precondition was the application of a high electric field in order to align the ferroelectric polarization uniformly in one direction. However, the application of electric fields may influence the electrical resistance as reported in $\text{Au/BFCO/LaNiO}_3/\text{SiO}_2/\text{Si}$ heterostructure^[22] and in BFCO/SRO/STO thin films.^[23]

The coexistence of multiferroic, photovoltaic, and resistive switching properties makes BFCO an ideal material to conceptualize novel (self-powered) photo-neuromorphic devices, for example, combining photovoltaic and neuromorphic applications.^[24] In conjunction, the response to light essentially also allows non-destructive readout of both, resistive and ferroelectric, state of the material.^[25]


In this work, BFCO thin films on STO (001) single-crystalline substrates with either SrRuO_3 (SRO) or $\text{La}_{0.7}\text{Sr}_{0.3}\text{MnO}_3$ (LSMO) as intermediate conductive layer were fabricated using pulsed laser deposition (PLD). The quality of the films was

D. S. Walch, Y. Yun, N. Ramakrishnegowda, L. Mühlenbein, A. Bhatnagar^[†]
Zentrum für Innovationskompetenz SiLi-nano
Martin-Luther-Universität Halle-Wittenberg
06120 Halle (Saale), Germany
E-mail: akash.bhatnagar@physik.uni-halle.de

D. S. Walch, Y. Yun, N. Ramakrishnegowda, L. Mühlenbein, A. Bhatnagar
Institut für Physik
Martin-Luther-Universität Halle-Wittenberg
06120 Halle (Saale), Germany

A. Lotnyk
IOM Leibniz-Institut für Oberflächenmodifizierung
04318 Leipzig, Germany

C. Himcinschi
TU Bergakademie Freiberg
Institut für Theoretische Physik
09596 Freiberg, Germany

 The ORCID identification number(s) for the author(s) of this article can be found under <https://doi.org/10.1002/aelm.202200276>.

© 2022 The Authors. Advanced Electronic Materials published by Wiley-VCH GmbH. This is an open access article under the terms of the Creative Commons Attribution-NonCommercial License, which permits use, distribution and reproduction in any medium, provided the original work is properly cited and is not used for commercial purposes.

^[†]Present address: SCHOTT AG Hattenbergstraße 10, 55122 Mainz, Germany

DOI: 10.1002/aelm.202200276

characterized using X-ray diffraction, SPM and TEM measurements. The superior photovoltaic performance of BFCO was first established upon comparison with BFO, as the short-circuit current density (i_{sc}) from BFCO exceeded that of BFO by around 700 times. The ferroelectric behavior was demonstrated and visualized with piezoresponse force microscopy (PFM) while the resistive states were observed with conductive atomic force microscopy (C-AFM). Sequential poling of regions assisted in ruling-out the polarization-flip as the underlying origin for the observed resistive switching effect. Macroscopic measurements were conducted that unraveled a case of bidirectional multi-stage resistive switching. The use of ITO as top electrodes facilitated the photovoltaic measurements on the same device, and enabled analyzing the corresponding impact. The variations in the conductance were sufficient to induce a change in the resultant open-circuit voltage (V_{oc}), an evident footprint of bulk-driven photovoltaic effect. The results further highlight the utility of light as a tool for read-out purposes.

2. Results and Discussion

BFCO thin films with a thickness of around 100 nm were deposited on single-crystalline STO (001) substrates using a PLD system. Details on the thin film growth can be found in the Experimental Section. Conductive SRO or LSMO buffer layers were deposited to enable (photo) electrical measurement across the BFCO thin film (see inset **Figure 1a**). Crystallinity and phase purity of the heterostructures were confirmed with X-ray measurement. The resultant $2\theta - \omega$ scans around the (002) substrate peak are presented in **Figure 1a**. Additionally,

high-resolution TEM images of the BFCO/SRO//STO structure can be found in **Figure S1**, Supporting Information. In case of BFCO/SRO//STO (red), the peaks arising from BFCO and SRO appear to be merged together as both layers grow under compressive epitaxial strain and exhibit similar lattice parameter. On the other hand, in case of BFCO/LSMO//STO (blue), the larger lattice constant of STO compared to LSMO results in tensile epitaxial strain, and consequently the peaks from LSMO and BFCO are split from one another separated by the STO substrate peak. Reciprocal space maps (RSM) around the (204) STO plane for both samples are shown in **Figure 1b**. In particular, the RSM of the BFCO/LSMO//STO shows two distinct peaks arising from the BFCO layer. The BFCO split-peak is also visible in BFCO/SRO//STO, although, not distinguishable into two. The closeness with the lattice parameter of SRO results in a rather convoluted four-way split.

One possible reason for this observation is the existence of a layered structure within the BFCO film, evidently visible in the cross-sectional images acquired with TEM in **Figure 1c**. Further analysis conducted with energy dispersive X-rays (EDX) mapping provided a qualitative proof of the existence of Fe- and Cr-rich regions across the entire thickness of the sample (see EDX profiles in **Figure S2**, Supporting Information). While in some regions the dominant presence of one and the depletion of the other ion is clearly visible. As expected, the A-site cation, Bi^{3+} , is found to be uniformly distributed. However, local analysis of d -spacing using TEM in BFCO layer at different regions did not show any significant changes. The existence of different domain variants (with different in-plane polarization direction) can cause a layer peak splitting in the RSM measurements which has been known in BFO^[26] and also recently

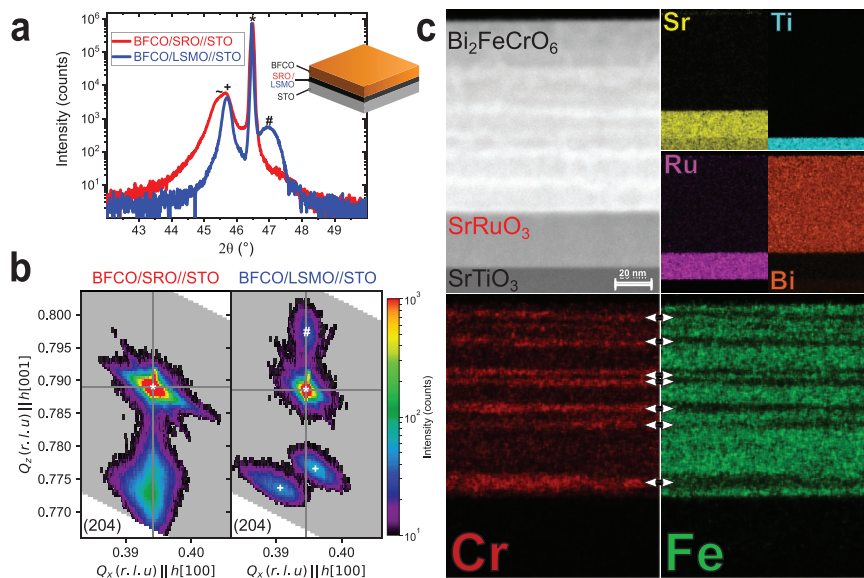


Figure 1. Structural characterization. a) $2\theta - \omega$ scans around (002) substrate peak of BFCO/SRO//STO (red) and BFCO/LSMO//STO (blue) films (* STO substrate, + BFCO, # LSMO, - SRO). b) RSM maps around (204) substrate plane of BFCO/SRO//STO (left) and BFCO/LSMO//STO (right) film. c) STEM-HAADF image (top left). EDX maps of Sr (yellow), Ti (turquoise), Ru (pink), Bi (orange) (all top right), Cr (red, bottom left), and Fe (green, bottom right).

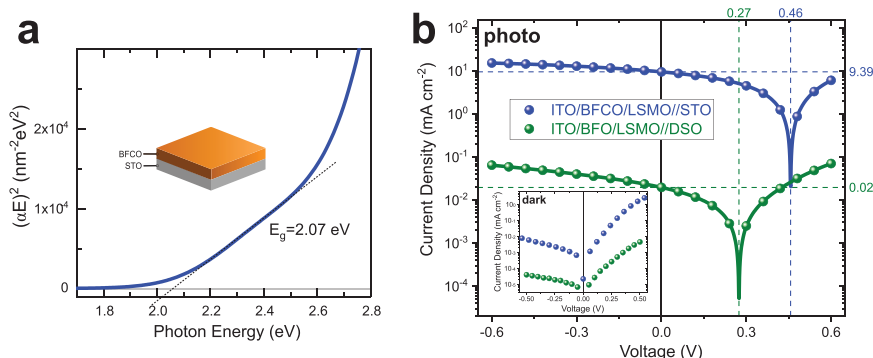


Figure 2. Initial photovoltaic measurements. a) The square of the product between absorption coefficient α and the energy E , as function of energy of a BFCO//STO structure. The bandgap was determined by the linear extrapolation to zero absorption. b) Current–voltage characteristics under 405 nm illumination of ITO/BFCO/LSMO//STO (blue) and ITO/BFO/LSMO//DSO structure (green). Fit (solid lines) used to extract V_{oc} values.

demonstrated in BFCO thin films.^[27] In other recent publications, such peak-split was attributed to existence of cationic ordered and disordered domains within the BFCO layers.^[17,21,28]

2.1. Photovoltaic Effect

The ordering of the iron and chromium ions at the B-sites, studied with ab initio calculations by Baettig et al., results in rather intricate hybridizations between the 3d orbitals of iron and chromium with the oxygen 2p orbital.^[4,5] Interestingly, the chromium 3d states do not only contribute to the conduction band but their hybridization with oxygen 2p orbital is also not negligible and plays host to spin-polarized holes. An evident impact is on the photovoltaic properties which have been found to be much improved in comparison to any other ferroelectric.^[20,21]

We validated this scenario by measuring the ellipsometry spectra of the BFCO//STO structure. From the BFCO extinction coefficient determined by ellipsometry, the absorption coefficient α was calculated. The onset of absorption region was analyzed and a bandgap of ≈ 2.07 eV was obtained by linear extrapolation of $(\alpha E)^2$ versus energy as it is shown in **Figure 2a**. This value is significantly lower than the reported direct bandgaps of BFO (2.7 eV)^[29,30] or BCO (2.95 eV)^[31] thin films. The determined value of band gap is in good agreement with literature values determined for BFCO films, and it can be tuned by the growth conditions.^[21,32–34] Lowering of bandgap values has also been observed in other Fe/Cr mixed systems in comparison with the parent compounds (as in the case of LaFe_{0.5}Cr_{0.5}O₃^[35] or HoFe_{0.5}Cr_{0.5}O₃^[36]) due to charge transfer excitation between Fe and Cr.

To measure the photovoltaic properties, electrodes were structured using a photolithography process and subsequently ITO was deposited on the BFCO/LSMO//STO structure using a radio frequency sputtering machine (see Experimental Section). BFCO/LSMO//STO structure was used for macroscopic measurements primarily for three reasons: i) extent or nature of ordering in the BFCO samples if one considers the RSM in **Figure 1b**; ii) reduced surface roughness (see **Figure 3a,e**), thus the interface between top electrode and the surface can

be expected to be more homogeneous and; iii) homogeneous response from ferroelectric domains in PFM measurements (see **Figure 3b,f**). **Figure 2b** shows the resultant current–voltage (I – V) characteristics under laser light illumination (3.06 eV, 405 nm) that reveal a V_{oc} of 0.46 V and an i_{sc} of 9.39 mA cm^{–2}, which culminates into a higher photovoltaic performance if compared with a ITO/BFO/LSMO//DSO reference sample ($V_{oc} = 0.27$ V, $i_{sc} = 0.02$ mA cm^{–2}). The dark I – V (inset) also demonstrates a higher conductivity of the BFCO/LSMO//STO structure compared to the BFO reference film. Under solar simulator illumination (1.5 AM), the photovoltaic performance of the ITO/BFCO/LSMO//STO structure reduces to $V_{oc} = 0.21$ V and $i_{sc} = 73.1$ μ A cm^{–2} (see **Figure S3**, Supporting Information). This is still much lower compared to the highly efficient single layer BFCO thin films reported by Nechache et al.,^[21] however, the application of high electric fields prior to the photovoltaic measurement is needed to align the ferroelectric polarization uniformly in one direction.

2.2. Scanning Probe Microscopy

PFM measurements were performed to verify the switchability and retention of polarization. DC voltages of opposite polarity were applied subsequently in squared-regions of diminishing sizes that is, +5 V: 10 \times 10 μ m² \rightarrow –5 V: 6 \times 6 μ m² \rightarrow +5 V: 3 \times 3 μ m², (see schematic **Figure 3 top**). The consequent vertical PFM measurements are shown in **Figure 3a–c,e–g** for the BFCO/SRO//STO and BFCO/LSMO//STO films, respectively. The topography of the BFCO/LSMO//STO film (**Figure 3e**) reveals a reduced roughness and grain size compared to the BFCO/SRO//STO film (**Figure 3a**). Importantly, the topographies remain unchanged after the application of the DC voltages. For both the samples, the contrast in the vertical PFM phase images (**Figure 3b,f**), corresponding to the oppositely-poled regions, clearly confirms ferroelectric switching. The vertical PFM amplitude images reveal the domain walls separating the written domains (**Figure 3c,g**).

To gain further information on the resistive/conductive state, C-AFM measurements were performed subsequently on the same area. The resulting current maps (**Figure 3d,h**)

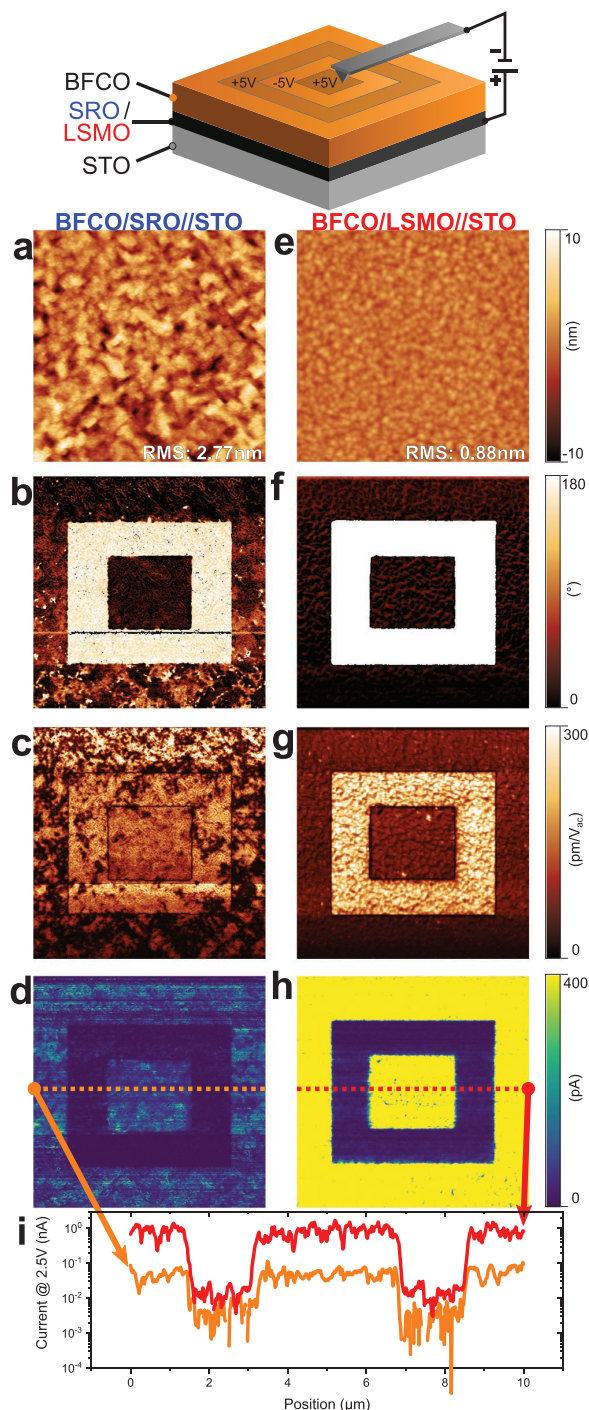


Figure 3. Scanning probe microscopy. Topography, vertical PFM phase, vertical PFM amplitude, C-AFM (read-out voltage 2.5 V) images ($10 \times 10 \mu\text{m}^2$) for BFCO/SRO//STO (a–d) and BFCO/LSMO//STO (e–h), respectively, with corresponding current line profiles (i).

show also a contrast, which is more pronounced with higher currents for the BFCO/LSMO//STO film as emphasized in the line scans in Figure 3i. The contrasts clearly suggest the formation and persistence of states exhibiting different values of resistance. Although such resistive switching behavior has been demonstrated with C-AFM on BFCO/Nb:STO films,^[34] the fields needed to pole the samples were much larger (+9 V) despite nearly half the thickness (49 nm). Furthermore, measurements on ultrathin (6 nm) BFCO films on SRO-buffered STO have demonstrated the coexistence of ferroelectric and bipolar resistive switching, also under the C-AFM tip.^[23]

Additionally, systematic scans were conducted with SPM to evaluate the correlation between the observed ferroelectric and resistive switching. The AFM topography image in Figure 4a shows the outline of a subdivided area into four equally large rectangular parts (each $2.5 \times 10 \mu\text{m}^2$). Different voltages (+5 V, 0 V, -5 V, +5 V) were applied to each area. The subsequent C-AFM (only upper half shown) and PFM (only lower half shown) measurements with corresponding line scan are shown in Figures 4b,c and 4d,e, respectively. The C-AFM image (readout voltage 1.5 V) shows only a high current response in +5 V-poled areas with maximum currents exceeding 500 pA. The measured current at the pristine (0 V) and -5 V-poled area is much lower with maximum current values in the range of tens of picoamperes. The current of the right half of the C-AFM current map (-5 V, 5 V) mimics the findings presented in Figures 3 and 5, in which the material is in the high-resistive (HR) and low-resistive (LR) state after the applications of positive and negative voltages, respectively. Importantly, despite the fact that the ferroelectric polarization within the +5 V-poled and pristine area are alike, as apparent from the vertical PFM phase images, the CFM images clearly suggests a much different state of resistance in the two regions. This essentially demonstrates the coexistence of ferroelectric and resistive switching, while being independent from one another.

2.3. Macroscopic Electrical Measurements

Upon observation of switchable ferroelectric and resistive states using SPM techniques, I - V characteristics of the BFCO/LSMO//STO sample were measured with a larger voltage range and ITO as the top electrode. The current measured during a triangular voltage sweep ($0 \text{ V} \rightarrow +5 \text{ V} \rightarrow -5 \text{ V} \rightarrow 0 \text{ V}$) at a rate of 0.1 V s^{-1} is shown in Figure 5a. In the positive voltage regime, a splitting of forward and backward scan is observed. With opposite polarity, the splitting becomes even more evident with distinct turning point at about -2 V. Focusing on the slope of the curve around the origin, a relatively higher slope can be observed after the application of positive voltages than after negative.

To get a deeper insight, the measurement was repeated, albeit, with acquisition of intermediate I - V characteristics. After every 0.5 V, I - V characteristics with a smaller voltage range of $\pm 0.2 \text{ V}$ (see Figure 5b inset) was acquired to gain information on the resistive/conductive state of the sample. The resultant intermediate I - V curves always exhibit linear

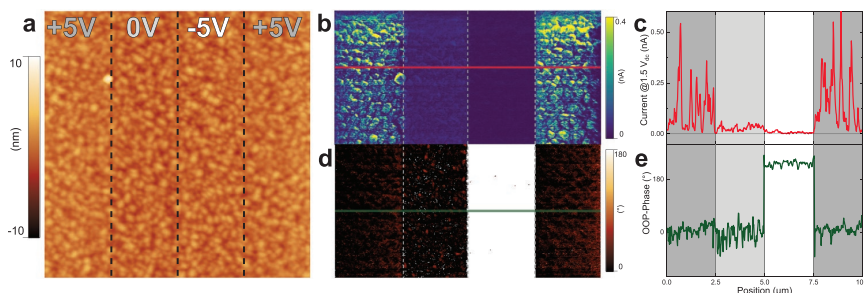


Figure 4. Comparing initial, HR, and LR states using SPM measurements. a) AFM image ($10 \times 10 \mu\text{m}^2$) with dotted lines indicating areas of different applied voltages. b,c) C-A FM current map of the upper half and corresponding line scan (read-out voltage 1.5 V). d,e) Vertical PFM phase images of lower half and corresponding line scan.

characteristic, and the extracted slope is sufficient to estimate the conductance and is plotted as a function of the applied voltage. The conductance as a function of applied voltage is shown in Figure 5b reveals a hysteretic behavior, in which the LR and HR state is obtained after application of positive and negative voltages, respectively. Such hysteretic behavior of the gap conductance has been observed in ferroelectric tunnel junctions, however, with only a several nanometer thick ferroelectric BaTiO₃ layer.^[37–40] The linear current response within

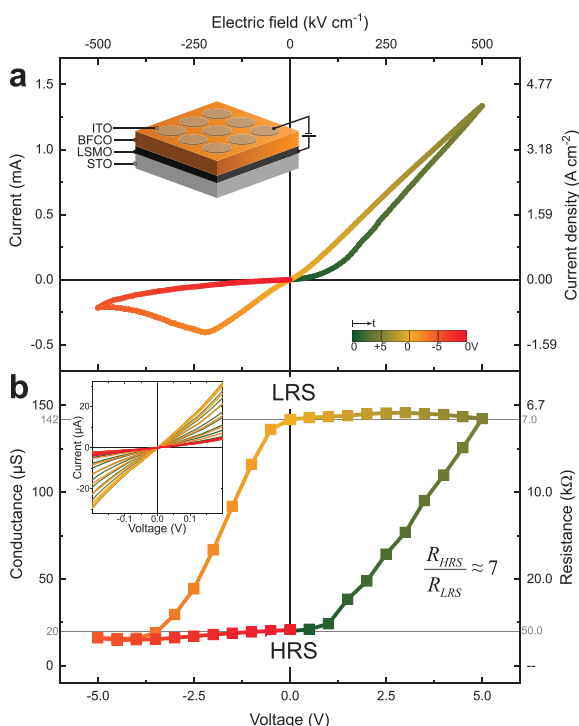


Figure 5. Resistive switching in macroscopic measurement. a) Current–voltage characteristic with schematic of ITO/BFCO/LSMO//STO structure. b) Hysteretic conductance–voltage behavior extracted from small range current–voltage characteristics (inset).

the narrow voltage range of the sample essentially also rules out the role of ferroelectric polarization-related mechanisms which have been widely reported to result in diode-like I – V characteristics.^[41–43] These aspects were further verified with dielectric measurements wherein the typical features associated with polarization-switching were not observed in capacitance–voltage measurements (see Figure S4, Supporting Information).

The hysteretic character of the switching behavior can be utilized to deterministically set different resistive states. This aspect has been presented in Figure 6a,b that shows with current–voltage and corresponding conductance–voltage characteristics, respectively with asymmetric voltage range and opposed sweeping direction. The measurements were conducted in two separate cycles. In the first cycle, the reset voltage was fixed at +5 V and individual I – V curves were measured as the set voltage was step-wise varied from –5 to –1 V with a step size of 1 V. The results clearly demonstrated the impact of the applied electric field on the conductance of the material, as the differences in the conductance (between HRS and LRS) and the effective resistance may be tuned from about 50 to 7 k Ω , respectively. The lower is the magnitude of the set voltage, the higher the resulting conductance ranging from the HR toward LR state at the end of the half-cycle. Note, the repeated application of a high reset voltage while lowering of set voltage magnitude results in a slight overall increase of the conductance at the end of the final cycles. As shown in Figure 5b the conductance hysteresis is not completely symmetric. In the positive voltage regime, the conductance does not seem to be saturated contrary to the negative direction. In the second cycle, the measurements were repeated, albeit with reset voltage as –5 V and set voltage varied from +5 to +1 V. The conductance after applying the set voltages reduces from the LRS toward the HRS with decreasing values of set voltage. The conductance saturates at about –4 V. Therefore and in contrast to Figure 5b, a continuing decrement of the conductance after repeated application of the negative reset voltage is not observed and the conductance after resetting is constant in Figure 5d. Figure 6 demonstrates the possibility of bi-directional multistage resistive switching in the ITO/BFCO/LSMO//STO heterostructure.

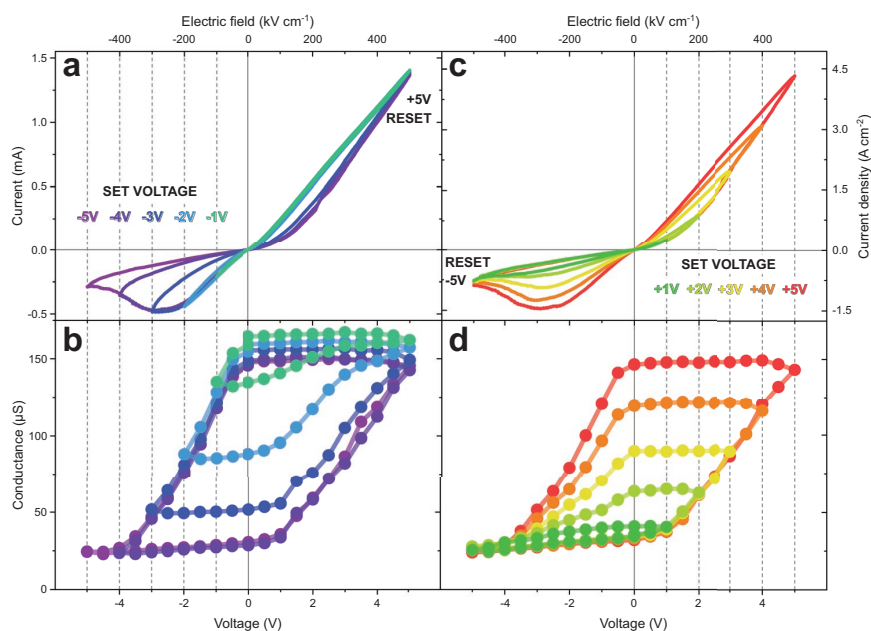


Figure 6. Multistage bi-directional resistive switching. Current–voltage and conductance–voltage characteristics with reducing set voltage magnitude in a,b) negative direction and c,d) positive direction, respectively.

Recent publications also demonstrated resistive switching in Au/BFCO/LaNiO₃/SiO₂//Si^[22] and Au/BFCO/SnO₂:F^[44] structures attributing the effect to changed boundary condition due to oxygen vacancy migration toward the interfaces.

2.4. Influence of Resistive Switching on Photovoltaic Effect

Figure 7a shows the dark *I*–*V* characteristics for the pristine, LR and HR states. The HR state has slightly higher conductivity than the pristine state, while the LR state exhibits much larger

conductivity resulting in high currents under bias fields. An increased dark conductivity influences the photovoltaic effect under the assumption that the charge-separation mechanism proceeds via bulk photovoltaic effect, which can be described by the following equation

$$V_{oc} = -\frac{I_{sc}l}{A(\sigma_{ph} + \sigma_{dark})} \quad (1)$$

Where *l*, *A*, σ_{ph} , and σ_{dark} are the distance between the electrodes, the area, the photo and dark conductivity, respectively.

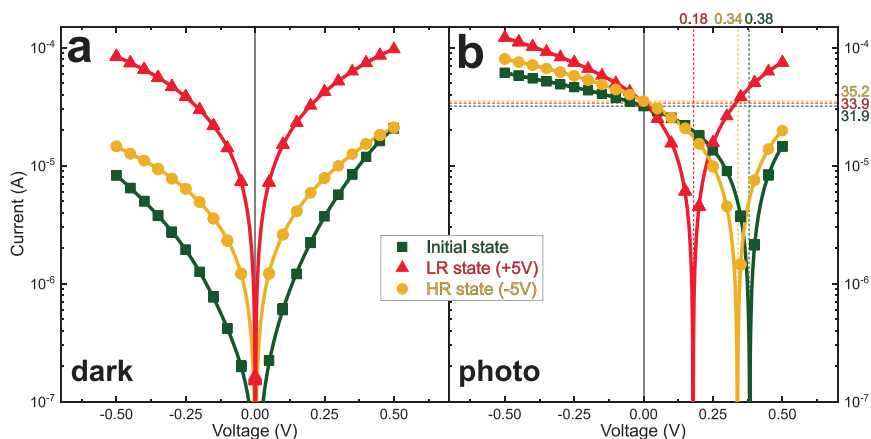


Figure 7. Influence of resistive switching on photovoltaic properties/optical sensing of resistive state. a) Dark and b) photo (405 nm laser illumination) current–voltage characteristics of initial, LR, and HR state. Fit (solid lines) used to extract V_{oc} values.

In case of constant I_{sc} , the resultant V_{oc} depends on the overall conductivity of the material. Hence, the LR and HR states may be used to tune the obtainable V_{oc} from the devices.

Figure 7b presents $I-V$ characteristics acquired under laser light with photon energy of 3.06 eV. Interestingly, the short-circuit current (I_{sc}) from each state, that is, HR state ($-35.2 \mu\text{A}$), LR state ($-33.9 \mu\text{A}$), and initial state ($-35.2 \mu\text{A}$) remain largely similar. However, there is a apparent change in the corresponding V_{oc} . It changes from 0.38 V in the initial state, to 0.18 V in the LR state, and back to 0.34 V in the HR state. Similar to the situation in Figure 7a, the V_{oc} does not completely recover back to the pristine state. Comparing HR and LR state, the V_{oc} and resistance (under light) reduce by half (V_{oc} : factor $V_{oc,HR}/V_{oc,LR} \approx 0.53$; $R_{HR}/R_{LR} = 10.61 \text{ k}\Omega/5.75 \text{ k}\Omega \approx 0.54$) according to Equation (1).

Alternatively, Figure 7b also demonstrates the possibility to use the photovoltaic effect to read out the conductive/resistive state of the material. Similar findings have been shown in ITO/BaTiO₃/LSMO//STO ferroelectric tunnel junctions at low temperature, in which the resulting V_{oc} depends on the resistive state of the memristor.^[39,40]

3. Conclusions

Epitaxial BFCO-based heterostructures were fabricated and were tested for their photoelectric, ferroelectric, and resistive switching properties. X-ray analysis was conclusive in proving the single crystalline nature of the samples and RSM suggested partial ordering of Fe and Cr ions at the B-site. TEM measurements confirmed the existence of Fe- and Cr-rich layers throughout the film thickness and atomic EDX provided a visual proof. In line with theoretical calculations, the ordering at the B-site not only serves lowering the band gap, but may also have an impact on the resultant conductivity.^[4] Consequently, the photoresponse from the BFCO was measured to be around 700 times larger than from BFO. SPM techniques, that is PFM and C-AFM, were used to test investigate the surface and ferroelectric properties. The polarization was switchable with ± 5 V and written domains remained stable. In the C-AFM mode, the domains of opposite polarities exhibited massively different states of electrical resistance with differences of more than one order of magnitude. Systematic scans conducted with different bias voltages, suggested little or no interlink between the ferroelectric and resistive states of the samples. Hence it can be implied, that oxygen ion migration and related mechanisms might be at the origin of the observed effects. Another aspect worthy to be mentioned is the higher conductivity in BFCO in comparison to BFO (inset Figure 2b) which in turn also results in much larger currents during the resistive switching. A possible reason could be the lower binding of oxygen 1s orbital in the BFCO in comparison to BFO, allowing the oxygen ions to easily dissociate.^[45]

Macro-scale measurements were conducted to further analyze the resistive switching characteristics. The SET and RESET voltages were successfully implemented to fine-tune the conductive states of the sample, and switch between HR, LR, and intermediate states. The absence of any abrupt change in the conductivity further supports this argument

and suggests a rather homogeneous migration of oxygen ions during the SET and RESET processes.^[46] The observed gradual changes in the resistance, also referred to analogue switching, are prerequisite for the realization of neuromorphic devices.^[47] The possibility to tune the conductance was eventually utilized to tune the V_{oc} under light which also evidently suggests the dominance of bulk-driven photoeffects in the samples. It is imperative to note here that the direction of I_{sc} , and corresponding polarity of V_{oc} , remain unchanged after the application of SET/RESET voltages, thereby ruling out any role of ferroelectric switching. The synergistic overlap of the different functionalities elaborated in this work namely, ferroelectricity, resistive switching and photovoltaics, presents BFCO as a rather lucrative system for highly coveted self-powered photo-neuromorphic applications.

4. Experimental Section

Thin Film Growth Using Pulsed Laser Deposition and Electrode Fabrication: The heterostructures were grown on single-crystalline STO (001)_c substrates using a pulsed laser deposition system (SURFACE PLD-Workstation, KrF excimer laser). The distance between the stoichiometric ceramic targets and the substrate is set to 60 mm. The films were cooled down at a rate of 20 °C min⁻¹ under a oxygen partial pressure of ≈ 200 mbar (Table 1).

Top electrodes were structured using a direct-write photolithography machine (DMO MicroWriter ML3) and ITO as transparent, conductive electrode materials (thickness 100–125 nm) were subsequently evaporated using a RF sputtering machine.

Spectroscopic Ellipsometry: The ellipsometric measurements were performed by using a M2000 J.A. Woollam ellipsometer. The ellipsometric data were evaluated and from the determined optical constants of BFCO the absorption coefficient α was calculated.

Transmission Electron Microscopy: Cross-sectional specimen for TEM investigations was prepared by focused gallium ion beam milling (Zeiss Auriga Dual-beam FIB). A probe Cs-corrected Titan3 G2 60-300 microscope was used for TEM studies. The microscope was operated at 300 kV accelerating voltage. The Titan was equipped with high-brightness gun (X-FEG), several annular detectors (Fischione, FEI), and Super-X energy-dispersive X-ray spectroscopy (EDS) system (FEI ChemiSTEM technology). Probe-forming aperture of 20 mrad was used during scanning TEM (STEM) measurements. STEM images were recorded with an annular dark-field detector (Fischione) using annular ranges of 80–200 mrad, which correspond to high-angle annular dark-field (HAADF) imaging condition. EDX maps were recorded in STEM mode using the Super-X EDS system. The maps were acquired and processed with Bruker software. The beam currents were set to 150 pA during the EDX mapping.

Scanning Probe Microscopy: SPM measurements were acquired with a Asylum Research Cypher equipped with a platinum-coated tip (MikroMasch NSC 15). PFM measurements were performed in Dual AC Resonance-Tracking (DART) mode with AC voltage of 1.5–2.5 V and a center drive frequency of ≈ 1.3 MHz. For C-AFM measurements, the read-out voltage was set to values of 1.5–2.5 V.

Table 1. PLD deposition parameters.

	BFCO	SRO	LSMO	BFO
Substrate temperature [°C]	700	750	650	725
O ₂ partial pressure [mbar]	0.01–0.02	0.067	0.2	0.145
Laser repetition rate [Hz]	1–2	1	2	2
Laser fluence [J cm^{-2}]	1.50	1.16	1.33	1.50

(Photo) Electrical Measurements: A high impedance electrometer / source meter (Keithley 6517B / Keithley 2450) acted as a voltage source (*I*-*V* characteristics, switching voltage) and simultaneously measured the current. The samples were illuminated by a diode laser (Cobolt 06 MLD / Thorlabs LDM9T) with a wavelength of 405 nm and 20 mW power. Additionally, a diode-based solar simulator (Wavelabs SINUS-70) was used as a light source to measure under 1.5 AM condition.

Supporting Information

Supporting Information is available from the Wiley Online Library or from the author.

Acknowledgements

The authors thank Professor Kathrin Dörr and Dr. Diana Rata for the X-ray measurements, Marian Lisca for the technical support, Dr. Bodo Fuhrmann and Dipl.-Phys. Sven Schlenker for their support with the facilities at the Interdisziplinäre Zentrum für Materialwissenschaften (IZM), Karl Heinze and Thomas Richter for the electrode deposition. Financial support from Bundesministerium für Bildung und Forschung (BMBF) Project No. 03Z22HN12, Deutsche Forschungsgemeinschaft (DFG) within Sonderforschungsbereiche (SFB) 762 (project A12), and Europäischen Fonds für regionale Entwicklung (EFRE) Sachsen-Anhalt is gratefully acknowledged.

Open access funding enabled and organized by Projekt DEAL.

Conflict of Interest

The authors declare no conflict of interest.

Author Contributions

A.B. and D.S.W. designed and conceived the experiments. D.S.W. was responsible for thin film growth, PFM analysis, and (photo) electric measurements. Y.Y., N.R., and L.M. participated in structural characterization. TEM specimen preparation and measurements were conducted by A.L. C.H. performed ellipsometric measurements and analysis. A.B. and D.S.W. co-wrote the manuscript with inputs from all the co-authors.

Data Availability Statement

The data that support the findings of this study are available from the corresponding author upon reasonable request.

Keywords

Bi₂FeCrO₆, ferroelectric photovoltaic effect, resistive switching

Received: March 11, 2022

Revised: May 23, 2022

Published online:

- [1] N. A. Hill, *J. Phys. Chem. B* **2000**, *104*, 6694.
[2] N. A. Hill, A. Filippetti, *J. Magn. Magn. Mater.* **2002**, *242-245*, 976.
[3] W. Eerenstein, N. D. Mathur, J. F. Scott, *Nature* **2006**, *442*, 759.

- [4] P. Baettig, C. Ederer, N. A. Spaldin, *Phys. Rev. B* **2005**, *72*, 2111.
[5] P. Baettig, N. A. Spaldin, *Appl. Phys. Lett.* **2005**, *86*, 012505.
[6] R. Nechache, C. Harnagea, A. Pignolet, F. Normandin, T. Veres, L. P. Carignan, D. Ménard, *Appl. Phys. Lett.* **2006**, *89*, 102902.
[7] R. Nechache, P. Gupta, C. Harnagea, A. Pignolet, *Appl. Phys. Lett.* **2007**, *91*, 222908.
[8] R. Nechache, L. P. Carignan, L. Gunawan, C. Harnagea, G. A. Botton, D. Ménard, A. Pignolet, *J. Mater. Res.* **2007**, *22*, 2102.
[9] V. M. Fridkin, B. N. Popov, *Sov. Phys.-Usp.* **1978**, *21*, 981.
[10] V. I. Belinicher, I. F. Kanaev, V. K. Malinovsky, B. I. Sturman, *Ferroelectrics* **1978**, *22*, 647.
[11] B. I. Sturman, V. M. Fridkin, *The Photovoltaic and Photorefractive Effects in Noncentrosymmetric Materials*, Gordon and Breach, Philadelphia **1992**.
[12] V. M. Fridkin, *Crystallogr. Rep.* **2001**, *46*, 654.
[13] A. Bhatnagar, A. Roy Chaudhuri, Y. Heon Kim, D. Hesse, M. Alexe, *Nat. Commun.* **2013**, *4*, 2835.
[14] D. S. Knoche, Y. Yun, N. Ramakrishnegowda, L. Mühlenbein, X. Li, A. Bhatnagar, *Sci. Rep.* **2019**, *9*, 13979.
[15] D. S. Knoche, M. Steimecke, Y. Yun, L. Mühlenbein, A. Bhatnagar, *Nat. Commun.* **2021**, *12*, 282.
[16] R. Nechache, C. Harnagea, S. Licoccia, E. Traversa, A. Ruediger, A. Pignolet, F. Rosei, *Appl. Phys. Lett.* **2011**, *98*, 202902.
[17] W. Huang, C. Harnagea, D. Benetti, M. Chaker, F. Rosei, R. Nechache, *J. Mater. Chem. A* **2017**, *5*, 10355.
[18] W. Huang, J. Chakrabarty, C. Harnagea, D. Gedamu, I. Ka, M. Chaker, F. Rosei, R. Nechache, *ACS Appl. Mater. Interfaces* **2018**, *10*, 12790.
[19] S. Zhang, H. Y. Xiao, S. M. Peng, G. X. Yang, Z. J. Liu, X. T. Zu, S. Li, D. J. Singh, L. W. Martin, L. Qiao, *Phys. Rev. Appl.* **2018**, *10*, 044004.
[20] L. Wei, C. Li, X. Li, J. Guo, D. Ge, L. Guan, B. Liu, *Appl. Phys. Express* **2019**, *6*, 096112.
[21] R. Nechache, C. Harnagea, S. Li, L. Cardenas, W. Huang, J. Chakrabarty, F. Rosei, *Nat. Photonics* **2015**, *9*, 61.
[22] H. L. Zhou, Y. P. Jiang, X. G. Tang, Q. X. Liu, W. H. Li, Z. H. Tang, *ACS Appl. Mater. Interfaces* **2020**, *12*, 54168.
[23] W. Xu, J. Sun, X. Xu, G. Yuan, Y. Zhang, J. Liu, Z. Liu, *Appl. Phys. Lett.* **2016**, *109*, 152903.
[24] A. Pérez-Tomás, *Adv. Mater. Interfaces* **2019**, *6*, 1900471.
[25] R. Guo, L. You, Y. Zhou, Z. S. Lim, X. Zou, L. Chen, R. Ramesh, J. Wang, *Nat. Commun.* **2013**, *4*, 1990.
[26] Y. H. Chu, M. P. Cruz, C. H. Yang, L. W. Martin, P. L. Yang, J. X. Zhang, K. Lee, P. Yu, L. Q. Chen, R. Ramesh, *Adv. Mater.* **2007**, *19*, 2662.
[27] Y. Liu, J. Lin, N. Zhong, P. H. Xiang, Y. Chen, P. Yang, J. Chu, C. G. Duan, L. Sun, *J. Appl. Phys.* **2020**, *128*, 234103.
[28] W. Huang, C. Harnagea, X. Tong, D. Benetti, S. Sun, M. Chaker, F. Rosei, R. Nechache, *ACS Appl. Mater. Interfaces* **2019**, *11*, 13185.
[29] S. R. Basu, L. W. Martin, Y. H. Chu, M. Gajek, R. Ramesh, R. C. Rai, X. Xu, J. L. Musfeldt, *Appl. Phys. Lett.* **2008**, *92*, 091905.
[30] D. Sando, C. Carrétéro, M. N. Grisolia, A. Barthélémy, V. Nagarajan, M. Bibes, *Adv. Optical Mater.* **2018**, *6*, 1700836.
[31] C. Himcinschi, I. Vrejoiu, T. Weißbach, K. Vijayanandhini, A. Talkenberger, C. Röder, S. Bahmann, D. R. T. Zahn, A. A. Belik, D. Rafaja, J. Kortus, *J. Appl. Phys.* **2011**, *110*, 073501.
[32] S. Li, B. Alotaibi, W. Huang, Z. Mi, N. Serpone, R. Nechache, F. Rosei, *Small* **2015**, *11*, 4018.
[33] A. Quattropani, D. Stoeffler, T. Fix, G. Schmerber, M. Lenertz, G. Versini, J. L. Rehspringer, A. Slaoui, A. Dinia, S. Colis, *J. Phys. Chem. C* **2018**, *122*, 1070.
[34] M. V. Rastei, F. Gellé, G. Schmerber, A. Quattropani, T. Fix, A. Dinia, A. Slaoui, S. Colis, *ACS Appl. Energy Mater.* **2019**, *2*, 8550.
[35] J. Andreasson, J. Holmlund, S. G. Singer, C. S. Knee, R. Rauer, B. Schulz, M. Käll, M. Rübhausen, S. G. Eriksson, L. Börjesson, A. Lichtenstein, *Phys. Rev. B* **2009**, *80*, 075103.

- [36] G. Kotnana, S. N. Jammalamadaka, *J. Appl. Phys.* **2015**, *118*, 124101.
- [37] H. J. Mao, C. Song, L. R. Xiao, S. Gao, B. Cui, J. J. Peng, F. Li, F. Pan, *Phys. Chem. Chem. Phys.* **2015**, *17*, 10146.
- [38] J. Li, C. Ge, J. Du, C. Wang, G. Yang, K. Jin, *Adv. Mater.* **2020**, *32*, 1905764.
- [39] A. Rivera-Calzada, F. Gallego, Y. Kalcheim, P. Salev, J. Del Valle, I. Tenreiro, C. León, J. Santamaría, I. K. Schuller, *Adv. Electron. Mater.* **2021**, *7*, 2100069.
- [40] I. Tenreiro, V. Rouco, G. Sánchez-Santolino, F. Gallego, C. Leon, A. Rivera-Calzada, I. K. Schuller, J. Santamaria, *Appl. Phys. Lett.* **2022**, *120*, 034101.
- [41] T. Choi, S. Lee, Y. J. Choi, V. Kiryukhin, S. W. Cheong, *Science* **2009**, *324*, 63.
- [42] C. Wang, K. j. Jin, Z. t. Xu, Le Wang, C. Ge, H. b. Lu, H. z. Guo, M. He, G. z. Yang, *Appl. Phys. Lett.* **2011**, *98*, 192901.
- [43] S. Hong, T. Choi, J. H. Jeon, Y. Kim, H. Lee, H. Y. Joo, I. Hwang, J. S. Kim, S. O. Kang, S. V. Kalinin, B. H. Park, *Adv. Mater.* **2013**, *25*, 2339.
- [44] S. Hu, Z. Tang, L. Zhang, D. Yao, Z. Liu, S. Zeng, X. Guo, Y. Jiang, X. G. Tang, L. Ma, Z. Nie, J. Gao, *J. Mater. Chem. C* **2021**, *9*, 13755.
- [45] R. Nechache, C. Harnagea, L. P. Carignan, D. Ménard, A. Pignolet, *Philos. Mag. Lett.* **2007**, *87*, 231.
- [46] S. Slesazeck, T. Mikolajick, *Nanotechnology* **2019**, *30*, 352003.
- [47] W. Zhang, B. Gao, J. Tang, X. Li, W. Wu, H. Qian, H. Wu, *Phys. Status Solidi RRL* **2019**, *13*, 1900204.

6.S Supplementary Information

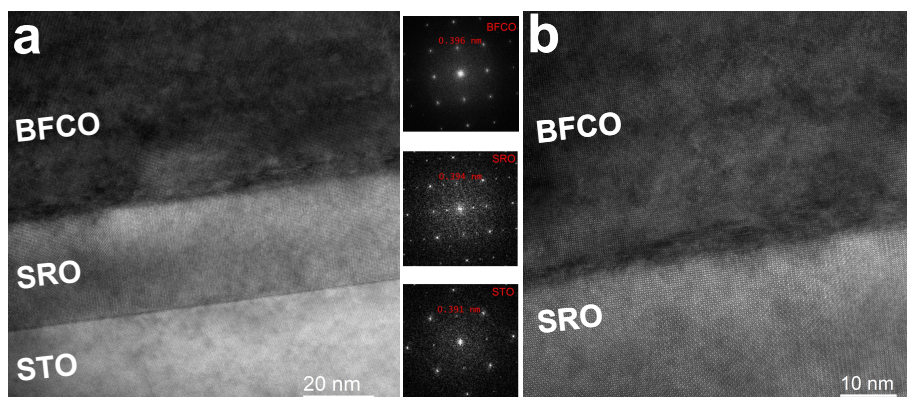


Figure 6.S1: HR-TEM images of (a) BFCO/SRO//STO structure and (b) BFCO/SRO interface.

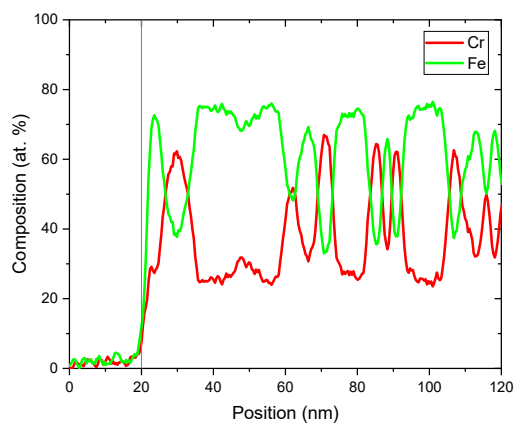


Figure 6.S2: Fe and Cr composition profile along growth axis extracted from EDX maps of BFCO/SRO//STO structure shown in Fig.1c in the manuscript. Vertical line indicates the BFCO/SRO interface.

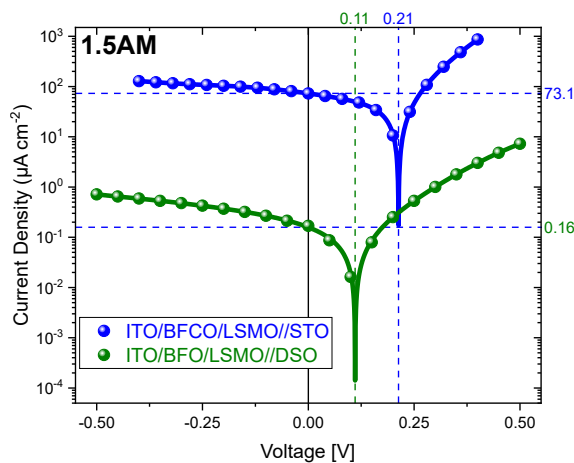


Figure 6.S3: Current-voltage characteristics under 1.5 AM solar simulator illumination of ITO/BFCO/LSMO//STO (blue) and ITO/BFO/LSMO//DSO structure (green).

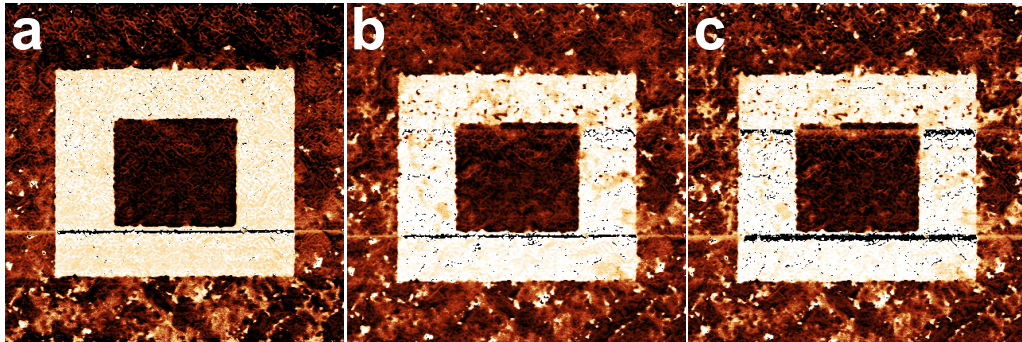


Figure 6.S4: Vertical PFM phase image of BFCO/SRO//STO structure (a) after poling, (b) after 2.5 V C-AFM read-out, and (c) after one day. All images: $10 \times 10 \mu\text{m}^2$.

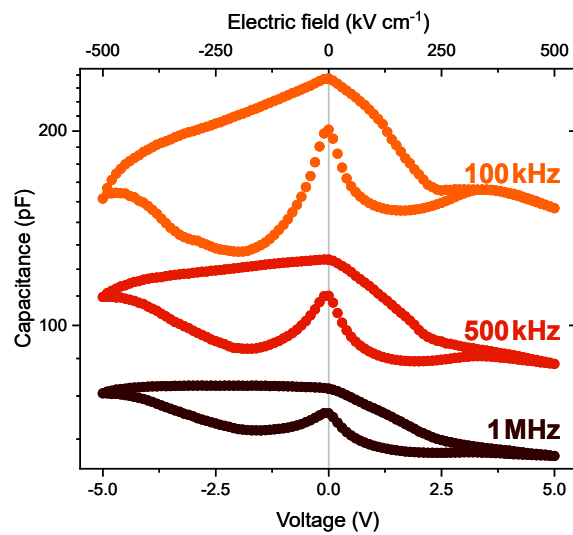


Figure 6.S5: Capacitance as a function of applied voltage of ITO/BFCO/LSMO//STO structure. AC voltage is kept 0.1 V, whereas the frequency is changed from 100 kHz (top), to 500 kHz (middle), to 1 MHz (bottom).

Summary - CHAPTER 6

Epitaxial $\text{Bi}_2\text{FeCrO}_6$ thin films with intermediate conductive perovskite oxide layer ($\text{La}_{0.7}\text{Sr}_{0.3}\text{MnO}_3$ or SrRuO_3) were grown on SrTiO_3 substrates using PLD. The high thin film quality was confirmed using AFM, XRD and TEM measurements. XRD RSM measurements implied the existence of a layered ordering inside the $\text{Bi}_2\text{FeCrO}_6$ layer. High-resolution TEM EDX mapping revealed a self-ordered ionic arrangement of the B-site cations (Fe^{3+} and Cr^{3+}) throughout the film thickness (Figure 6.1). A reduced band gap and a higher conductivity were identified as possible reasons for a superior photovoltaic performance compared to BiFeO_3 reference samples (Figure 6.2). PFM measurements were used to test the local ferroelectric switching properties (Figure 6.3). The reliable ferroelectric switching was accompanied by a persistent change of the electrical resistance as demonstrated by further C-AFM investigations. More detailed PFM/C-AFM measurements were used to explore the connection between ferroelectric and resistive switching. Through this, the mechanism behind the resistive switching was demonstrated to be decoupled from the ferroelectric switching (Figure 6.4). Furthermore, the resistive switching behavior was also demonstrated on a macroscopic scale using transparent $\text{In}_2\text{O}_3:\text{Sn}$ top electrodes (Figure 6.5). The macroscopic measurements demonstrated a robust bi-directional multi-stage resistive character (Figure 6.6). The characterization of the photovoltaic effect of different resistive states revealed different magnitudes of the open-circuit voltage. Because of the direct influence of the resistive switching on the photovoltaic properties, the readout of the open-circuit voltage can reveal information about the resistive state (Figure 6.7).

CHAPTER 7

Summary & Conclusion

The main objective of this cumulative thesis was to present the results of fundamental investigations of the BPV effect in bismuth-based ferroelectric perovskite oxides, BiFeO_3 and $\text{Bi}_2\text{FeCrO}_6$. The major results of this thesis were published in three peer-reviewed articles as presented in Chapter 4, Chapter 5 and Chapter 6.

Both materials exhibit promising functional properties and especially their magnetoelectric multiferroic character make both materials interesting for novel applications. Furthermore, BiFeO_3 and $\text{Bi}_2\text{FeCrO}_6$ are known to show prominent photovoltaic effects. BiFeO_3 is one of the prototype photovoltaic ferroelectric material due to its comparable low band gap and its ferroelectric character with high polarization values. The occurrence of a lateral polarization component in epitaxially grown thin films on various substrates is another property, which makes BiFeO_3 interesting for various applications and fundamental experiments of the BPV effect.

As part of this work, systematic in-plane BPV measurements under linearly polarized light of epitaxial BiFeO_3 thin films with unordered ($\text{BiFeO}_3//\text{SrTiO}_3$) and ordered ($\text{BiFeO}_3//\text{DyScO}_3$) domain arrangement were conducted. The experimental findings were followed by analytical calculations, which demonstrated the tensorial nature of the PV effect in BiFeO_3 . Moreover, the observed open-circuit voltages ($> 10\text{ V}$) exceeded the corresponding band gap (2.7 eV). By accompanying the BPV measurements with a detailed PFM analysis, it was possible to monitor the change of the ferroelectric domain structure under the application of electric fields. In doing so, a sensitive co-dependency between the ferroelectric domain configuration and the BPV response was observed. Consequently, the BPV response could be used to estimate the switching progress in the entire electrode gap. Furthermore, the results unraveled the possibility to utilize BPV measurements to analyze and trace the net in-plane polarization of large areas.

After the demonstration of the possible utilization of BPV measurements under linearly polarized light to gain information of the present ferroelectric polarization state, the BPV effect under circularly polarized light, the circular BPV effect, was investigated in BiFeO_3 for the first time. Systematic photoelectrical investigation of BiFeO_3 thin films with ordered domain configuration ($\text{BiFeO}_3//\text{DyScO}_3$) illustrated the evolution of the BPV effect while the light polarization was modulated from linear to elliptical to circular. The observed open-circuit voltage values under circularly polarized light ($> 20\text{ V}$) were found to be well-above the corresponding band gap. However, the experimental findings partially contradicted the predicted behavior based on the tensorial analysis of the effect and an anomalous character of the circular BPV effect in BiFeO_3 was observed. A deeper analysis of the domain-resolved BPV response

suggested the existence of a domain-specific and chirality-dependent light-matter interaction. The adjustment of the electrode alignment with respect to the net in-plane polarization of one ferroelectric domain variant led to a maximum open-circuit voltage exceeding 25 V under left-handed circularly polarized light. Whereas the measured open-circuit voltage under right-handed circularly polarized light almost vanished. It was possible to reverse this scenario by aligning the electrodes with respect to the other domain variant. These findings demonstrated a light-chirality-dependent ON and OFF state of the circular BPV effect. In conjunction with spatially-resolved Raman scattering experiments, the observed behavior supported the assumption of a domain-specific and chirality-dependent light-matter interaction. The chiral magnetic texture in BiFeO_3 , the antiferromagnetic spin cycloid, could be the origin of this differential light-domain behavior.

The demonstrated existence of both ferroelectric and ferromagnetic properties at room temperature and the established record solar conversion efficiency of perovskite oxide materials made $\text{Bi}_2\text{FeCrO}_6$ an interesting material for investigations of functional properties and their interplay. The last part of this work focused on the investigation of (photo)electrical properties of $\text{Bi}_2\text{FeCrO}_6$ thin film heterostructures ($\text{Bi}_2\text{FeCrO}_6/\text{SrRuO}_3//\text{SrTiO}_3$ & $\text{Bi}_2\text{FeCrO}_6/\text{La}_{0.7}\text{Sr}_{0.3}\text{MnO}_3//\text{SrTiO}_3$). The initial structural characterization of the $\text{Bi}_2\text{FeCrO}_6$ thin films based on XRD and transmission electron microscopy (TEM) methods confirmed the high thin film quality and revealed a self-ordered ionic arrangement of the B-site cation. Furthermore, a reduced band gap and higher conductivity led to a superior PV performance compared to a BiFeO_3 reference sample. However, the observed PV performance was inferior compared to the reported solar conversion efficiency record. Following the literature, one underlying pre-condition to obtain high PV performance was the application of high electric fields to achieve a uniform alignment of the ferroelectric polarization. The ferroelectric switching behavior of the investigated $\text{Bi}_2\text{FeCrO}_6$ thin films was tested using SPM techniques, revealing the co-existence of ferroelectric and resistive switching. However, the two switching characteristics were found to be independent from each other. The experimental findings at microscopic scale were confirmed with macroscopic measurements using transparent $\text{In}_2\text{O}_3:\text{Sn}$ top electrodes. A bi-directional multi-stage resistive switching behavior was observed. Finally, a direct impact of the resistive switching behavior on the PV properties was demonstrated.

The photoelectrical investigations summarized in this chapter demonstrate the variety of functional properties observable in BiFeO_3 and $\text{Bi}_2\text{FeCrO}_6$. Even though the use of the BPV effect in energy-harvesting devices might not be feasible in the foreseeable future, fundamental investigations of this effect can result in a better understanding of ferroelectric perovskite oxides and open the door for novel applications. The BPV effect can be utilized for non-destructive readout of the ferroelectric polarization in future non-volatile memory devices. The principle of new detectors could be based on the dependence of the BPV effect on the light polarization state. The implementation of photovoltaic ferroelectric functional oxides could lead to self-powered neuromorphic devices. Furthermore, one of the innumerable different compositions of perovskite oxides, not yet explored, could open the door for energy-harvesting applications in the future.

Curriculum Vitae

ANGABEN ZUR PERSON

Name	David Sebastian Walch (geb. Knoche), M.Sc.
Geburtsdatum	
Geschlecht	Angaben aus datenschutz-
Staatsangehörigkeit	rechtlichen Gründen entfernt
Adresse	

AUSBILDUNG

	Martin-Luther-Universität Halle-Wittenberg Naturwissenschaftliche Fakultät II - Chemie, Physik, Mathematik Doktorand am Institut für Physik (Dr. rer. nat.)
2018-2022	Zentrum für Innovationskompetenz (ZIK) SiLi-nano - Fachgruppe: Light for High-Voltage Photovoltaics - FG-Leiter: Dr. Akash Bhatnagar - Betreuer: Prof. Dr. Jörg Schilling
2015-2018	Martin-Luther-Universität Halle-Wittenberg Master of Science (M.Sc.) Erneuerbare Energien
2012-2015	Universität Siegen Bachelor of Science (B.Sc.) Maschinenbau (dual)
2003-2012	Städtisches Gymnasium Schmalleberg Allgemeine Hochschulreife (Abitur)

ANGABEN ZU VORSTRAFEN

Es liegen keine Vorstrafen vor und es wurde kein Ermittlungsverfahren eingeleitet.

Publikationsliste

ARTIKEL IN WISSENSCHAFTLICHEN ZEITSCHRIFTEN

Knoche, David S., Yun, Y., Ramakrishnegowda, N., Mühlenbein, L., Li, X. & Bhatnagar, A. "Domain and Switching Control of the Bulk Photovoltaic Effect in Epitaxial BiFeO₃ Thin Films". *Scientific Reports* **9**, 13979 (2019)

Ramakrishnegowda, N., Yun, Y., **Knoche, David S.**, Mühlenbein, L., Li, X. & Bhatnagar, A. "Activity of Sub-Band Gap States in Ferroelectric Pb(Zr_{0.2}Ti_{0.8})O₃ Thin Films". *Advanced Electronic Materials* **6**, 1900966 (2020)

Ramakrishnegowda, N., **Knoche, David S.**, Mühlenbein, L., Lotnyk, A. & Bhatnagar, A. "Bulk-Controlled Photovoltaic Effect in Nanometer-Thick Ferroelectric Pb(Zr_{0.2}Ti_{0.8})O₃ Thin Films and the Role of Domain Walls". *ACS Applied Nano Materials* **3**, 11881–11888 (2020)

Mühlenbein, L., Singh, C. B., Lotnyk, A., Himcinschi, C., Yun, Y., Ramakrishnegowda, N., **Knoche, David S.**, Li, X. & Bhatnagar, A. "Nanocomposites with Three-Dimensional Architecture and Impact on Photovoltaic Effect". *Nano Letters* **20**, 8789–8795 (2020)

Knoche, David S., Steimecke, M., Yun, Y., Mühlenbein, L. & Bhatnagar, A. "Anomalous circular bulk photovoltaic effect in BiFeO₃ thin films with stripe-domain pattern". *Nature Communications* **12**, 282 (2021)

Yun, Y., Mühlenbein, L., **Knoche, David S.**, Lotnyk, A. & Bhatnagar, A. "Strongly enhanced and tunable photovoltaic effect in ferroelectric-paraelectric superlattices". *Science Advances* **7** (2021)

Himcinschi, C., Drechsler, F., **Walch, David S.**, Bhatnagar, A., Belik, A. A. & Kortus, J. "Unexpected Phonon Behaviour in BiFe_xCr_{1-x}O₃, a Material System Different from Its BiFeO₃ and BiCrO₃ Parents". *Nanomaterials* **12** (2022)

Walch, David S., Yun, Y., Ramakrishnegowda, N., Mühlenbein, L., Lotnyk, A., Himcinschi, C. & Bhatnagar, A. "Resistive Switching in Ferroelectric Bi₂FeCrO₆ Thin Films and Impact on the Photovoltaic Effect". *Advanced Electronic Materials* **8**, 2200276 (2022)

KONFERENZEN

Knoche, David S., Yun, Y., Ramakrishnegowda, N., Mühlenbein, L., Li, X. & Bhatnagar, A. *Characterization of Switchable Polarization States in Epitaxial Bismuth Ferrite Thin Films Using the Bulk Photovoltaic Effect: (Conference Talk)*. in *E-MRS Spring Meeting, Nizza: Nano-functional materials: Polar oxides: synthesis, science and applications* (ed European Materials Research Society) (2019)

Knoche, David S., Yun, Y., Ramakrishnegowda, N., Mühlenbein, L., Li, X. & Bhatnagar, A. *Characterization of Switchable Polarization States in Epitaxial Bismuth Ferrite Thin Films Using the Bulk Photovoltaic Effect: (Poster)*. in *International School of Oxides Electronics, Cargèse* (ed Centre National de la Recherche Scientifique) (2019)

Knoche, David S., Yun, Y., Mühlenbein, L., Ramakrishnegowda, N., Li, X. & Bhatnagar, A. *Circular Bulk Photovoltaic Effect in Bismuth Ferrite: (Conference Talk)*. in *CMD2020GEFES, online: Oxide heterostructures and interfaces: from fundamentals to applications* (ed European Physical Society / Spanish Royal Physics Society) (2020)

Danksagung

Auch wenn ich immer der Meinung war, eine Danksagung wäre etwas Unnötiges, muss ich mir am Ende eingestehen, dass ich ohne Danksagung vielen Leuten Unrecht tun würde. Eben jene Leute, ohne die diese Dissertation nicht entstanden wäre.

An erster Stelle gilt dabei mein Dank **Akash**, der mich von der ersten Minute an mit seiner Begeisterung und Hingabe für sein Forschungsgebiet inspiriert hat und mich während meiner Zeit als Doktorand bedingungslos unterstützt und gefördert hat. Seine Tür stand stets offen und unsere Zusammenarbeit war geprägt von offener und konstruktiver Diskussion. Es fühlte sich mehr an, wie mit einem Freund etwas Gemeinsames zu schaffen, als seinem Vorgesetzten Zuarbeit zu leisten. Die Übersicht und objektive Einschätzung meiner Ergebnisse haben immer einen roten Faden vorgegeben und waren maßgebend für den Inhalt meiner Dissertation.

Als Nächstem möchte ich **Jörg** für die Betreuung und kompetente Unterstützung meiner Forschung und dieser Arbeit danken. Von Tag eins im ZIK SiLi-nano habe ich mich wohl gefühlt und immer Hilfe gefunden, wenn ich sie gebraucht habe. Außerdem möchte ich mich bei allen Kollegen aus dem ZIK bedanken. Die unterschiedlichen Einblicke aus den anderen Fachgruppe und die regelmäßige Auseinandersetzung mit den verschiedenen Disziplinen und Forschungsfeldern haben stets konstruktiv zu meiner Forschung beigetragen und neue Perspektiven und alternative Lösungsansätze aufgezeigt. Insbesondere bedanke ich mich aber bei meinen Kollegen aus der Arbeitsgruppe **Yeseul, Niranjan, Lutz** und **Xinye** für das erfolgreiche und freundschaftliche Zusammenarbeiten. Während der unzähligen Stunden im Labor, Büro und Reinraum wart ihr alle nicht nur aus wissenschaftlicher Sicht eine große Bereicherung. Jeder von euch hat seinen Teil zu den Veröffentlichungen und somit zu dieser Arbeit beigetragen. Ein großer Extradank geht natürlich noch an **Marian**. Die kompetente und unkomplizierte Hilfe bei technischen Problemen, Beschaffung und auch bei wissenschaftlichen Fragen waren täglicher Begleiter und ohne diese wäre so manch ein Arbeitstag vermutlich immer noch nicht vorbei. Ein ebenso großer Extradank geht an **Romy** und **Sandra** für die schnelle Hilfe bei allen organisatorischen, koordinatorschen und sonstigen Fragen. Als letztes aus dem ZIK-Team möchte ich mich bei **Koundinya** für die unzähligen Tischtennispartien bedanken. Gerade in der letzten Phase haben die sportlichen Pausen wieder Schwung gebracht und ich bin froh, dass wir uns die Siege stets brüderlich aufgeteilt haben.

Dann möchte ich mich bei den weiteren Koautoren meiner Publikationen bedanken. Insbesondere bei **Matthias** für die unglaublich schnelle und unkomplizierte Hilfe durch die Raman-Messungen, über deren Ergebnisse ich mich bis heute freue. Außerdem bei **Andriy** für die TEM-Messungen und bei **Cameliu** für die optischen Messungen.

Als Nächstes möchte ich mich herzlich bei **Prof. Kathrin Dörr**, **Prof. Marin Alexe** und **Dr. Ignasi Fina Martínez** für die Bereitschaft zur Begutachtung meiner Arbeit bedanken. Während meiner Promotion hat mich ihre Forschung im Bereich der ferroelektrischen Oxide stets begleitet und inspiriert. Außerdem bedanke ich mich herzlich bei **Prof. Dietrich Hesse** für die Anregungen und Rat zu den Veröffentlichungen.

Dann möchte ich mich natürlich noch bei meinen treuen Spikeball-Siedler-Begleitern **Emil, Karl, Nils** und **Falko** bedanken. Dabei nicht nur wegen der sportlichen und denksportlichen Zeit zusammen, sondern auch und vor allem für alles andere. Es war mir stets eine Freude. Als Nächstem möchte ich noch **Christian** für das beste Abendprogramm danken. Auch wenn die Entspannung immer erst ein paar Tage später einsetzen konnte. Zudem gilt der Dank aber auch den stets offenen Türen und die gute Freundschaft. Außerdem danke ich **Christopher** für ein stets offenes Ohr und für das Korrekturlesen meiner Dissertation.

Zu vorletzt möchte ich noch meiner **Familie**, leiblich sowie angeheiratet, danken. Insbesondere aber meinen **Eltern** für die Unterstützung bei meinem doch von Quereinsteigen geprägten Werdegang danken. Der Rückhalt und die Sicherheit durch die Familie hat mir immer die nötige Kraft auch in schwierigen Situationen gegeben.

Und zu guter Letzt danke ich am allermeisten meiner wundervollen Frau **Mareike**. Du hast mich stets unterstützt und ermutigt, warst immer für mich da. Die Zeit der Promotion und die damit verbundene Fernbeziehung hat unsere Beziehung nur stärker gemacht. Ich freue mich auf unsere gemeinsame Zukunft zusammen mit unserem kleinen Prinz **Tamino**.

Selbständigkeitserklärung

Hiermit erkläre ich, David Sebastian Walch, ausdrücklich, dass ich die vorliegende Arbeit mit dem Thema

"The Photovoltaic Effect in Bismuth-Based Ferroelectric Perovskite Oxides"

selbständig und ohne unerlaubte fremde Hilfe angefertigt, keine anderen als die angegebenen Quellen und Hilfsmittel verwendet und die den verwendeten Quellen und Hilfsmitteln wörtlich oder inhaltlich entnommenen Stellen als solche kenntlich gemacht habe.

Ebenso erkläre ich, dass ich bisher keine vergeblichen Promotionsversuche unternommen habe und dass ich die Dissertation in der gegenwärtigen bzw. in einer anderen Fassung keiner anderen Fakultät vorgelegt habe.

Ort, Datum

Unterschrift